VICTORIA UNIVERSITY OF WELLINGTON

DOCTORAL THESIS

Confinement Properties of the 3D Topological Insulators Bi_2Se_3, Bi_2Te_3, and Sb_2Te_3

Author:	*Supervisor:*
Markus KOTULLA	Prof. Uli ZÜLICKE

A thesis
submitted to the Victoria University of Wellington
in fulfillment of the requirements for the degree of
Doctor of Philosophy

Condensed Matter Theory
School of Chemical and Physical Sciences

February, 2020

Dedicated to dad.
You planted trees whose shade
you weren't meant to enjoy.
But they will shelter us forever.

In loving memory,
Markus

VICTORIA UNIVERSITY OF WELLINGTON

Abstract

Faculty of Science
School of Chemical and Physical Sciences

Doctor of Philosophy

Confinement Properties of the 3D Topological Insulators Bi_2Se_3, Bi_2Te_3, and Sb_2Te_3

by Markus KOTULLA

Recent discoveries have spurred the theoretical prediction and experimental realization of novel materials that have topological properties arising from band inversion. Such topological insulators have conductive surface or edge states but are insulating in the bulk. How the signatures of topological behavior evolve when the system size is reduced is noteworthy from both a fundamental and an application-oriented point of view, as such understanding may form the basis for tailoring systems to be in specific topological phases. This thesis investigates the softly confined topological insulator family of Bi_2Se_3 and its properties when subjected to an in-plane magnetic field. The model system provides a useful platform for systematic study of the transition between the normal and the topological phases, including the development of band inversion and the formation of massless-Dirac-fermion surface states. The effects of bare size quantization, two-dimensional-subband mixing, and electron-hole asymmetry are disentangled and their corresponding physical consequences elucidated.

When a magnetic field is present, it is found that the Dirac cone which is formed in surface states, splits into two cones separated in momentum space and that these cones exhibit properties of Weyl fermions. The effective Zeeman splitting is much larger for the surface states than for the bulk states. Furthermore, the g-factor of the surface states depends on the size of the material. The mathematical model presented here may be realizable experimentally in the frame of optical lattices in ultra cold atom gases.

Acknowledgements

Writing a PhD thesis is not an easy task and it takes persistence. Without the help and support of friends and family, it would have been a difficult undertaking and I would like to express my sincerest gratitude to all my supporters.

First, I would like to thank the MacDiarmid institute, the Victoria University of Wellington, its researchers and administration staff for making it possible for me to write this thesis. Furthermore, I would like to thank my friends and family for their positive attitude and for their encouraging words. For help with the English language and her persistent reminders to keep writing, I would like to thank Carolin Janitschke. My parents and my partner I would like to thank wholeheartedly for empowering me to go through this project and for a life full of trust and love. I couldn't be where I am without you.

Most of all, I would like to express my sincerest gratitude to Uli Zülicke for his support, his advice, and especially for his patience. Thank you for not giving up on me.

Contents

Abstract **iii**

Acknowledgements **v**

1 A History of Physics **1**

1.1 Classical Condensed Matter Physics 2

1.2 Quantum Mechanics 3

1.3 Condensed Matter Physics 5

1.4 Topological Condensed Matter Physics 7

2 Topological Insulator Fundamentals **11**

2.1 Characterization of Crystal Structures in Physics 12

2.2 Characterization of Topology in Mathematics 15

2.3 The Berry Phase 17

2.4 Quantum Hall Effect 18

2.5 Quantum Spin Hall Effect 20

2.5.1 The Haldane Model 21

2.5.2 The Kane-Mele Model 22

3 Recent Developments **25**

3.1 A 3D Topological Insulator in Bi_2Se_3, Bi_2Te_3, and Sb_2Te_3 28

4 Confined 3D Topological Insulator with no external fields **33**

4.1 Model Hamiltonian for a Confined 3D Topological Insulator . 34

4.2 Properties of the System H_0 42

4.3 Properties of the Coupled System $H_0 + H_{||}$ 48

4.3.1 General Features of the $\mathscr{H}$ Band Structure 49

4.3.2 Gap Behavior 56

4.3.3 Four-fold Degeneracies 58

4.4 Properties of the Full system $H_0 + H_{||} + H_\epsilon$ 61

4.5 Classification of observed results 64

4.6 Summary 65

5 Confined 3D Topological Insulator in a Magnetic Field 67

5.1 Approximation of Magnetic Effects on H_0 71
5.2 Properties of the System $H_0(B)$ 76
5.3 Properties of the Coupled System $H_0(B) + H_{||} + H_B(B) + H_Z(B)$ 77
5.4 Effective Low Energy Model: g-factors and Cone Splittings . . 83
5.5 Properties of the System $H_0(B) + H_{||} + H_\epsilon(B) + H_B(B) + H_Z(B)$ 86
5.6 Summary 88

6 Summary and Outlook 89

Bibliography 93

List of Figures

2.1 (a) An amorphous material with no clear structure (i.e. glass). (b) The structure of a 2D crystal with a square lattice. The definition of the lattice vector $\mathbf{R}_n$ allows access to every lattice site. The region indicated by a square around a lattice point is called the Wigner-Seitz cell or Brillouin zone in the reciprocal lattice. 12
2.2 (a) All three displayed objects are topologically equivalent. The dashed (dotted) shapes are deduced by applying the homeomorphisms $f(x,y) = (x^3,y^3)$ ($f(x,y) = (\text{Sin}(x),\text{Sin}(y))$) to each coordinate of the circle (thick line). (b) A torus generating a 2D lattice of atoms (in red) by rotating along the lines and the atom indicated on the torus' surface. 15
2.3 (Left) Sketch of a flat material with conducting channels on its edges where the magnetic field is perpendicular to the material plane [39] and (right) example data showing quantized steps in resistance with varying magnetic field strength [40]. R_H is the Hall resistance associated with the conductivity σ_{xy} or σ_H and R_{xx} is the resistivity associated with σ_{xx}. The edge channels are not spin sensitive. 19
2.4 (left) Localization of the wave function at the interface of a trivial and a non-trivial Haldane system where $m(y)$ is approximated as a continuous function through $m = 0$ [42]. (right) Predicted edge state dispersion of Quantum Spin Hall state in Graphene as proposed by Kane and Mele [43]. 22
2.5 (Left) Sketch of a flat material with conducting channels on its edges due to the Quantum Anomalous Hall effect and (right) sketch of a flat material with conducting channels on its edges due to the Quantum Spin Hall effect where the edge channels are spin sensitive [39]. 23

3.1 (Left) Crystal structure of Bi_2Se_3. Bismuth selenide consists of one selenium layer (green), which is followed by a bismuth layer, another selenium layer, and a bismuth and selenium layer where the stacking occurs along the z axis. The x and y axis lie in the plane perpendicular to the stacking direction. The crystal obeys a mirror symmetry with the mirror plane normal lying in the x-y plane and pointing in y direction. (Right, obtained from [64]) The formation of the band structure of Bi_2Se_3. Note the inversion of valence and conduction band after the application of spin-orbit coupling - these bands have opposite parity. (I) Hybridization (II) Anti-bonding/Bonding (III) Crystal-Field-Splitting (IV) Spin-Orbit-Coupling 29

4.1 Band structure of H_0 for Bi_2Te_3: a) for an arbitrary $\gamma = 1.694$ which attributes to a width of 1 nm and b) for a smaller $\gamma = 0.7$ (wider TI) with a width of 1.71 nm. The red (black) bands denote (un-) inverted bands. The larger the width of the material, the more bands are inverted. 43
4.2 a) Energy dispersion of H_0 for Bi_2Se_3 at $\gamma = 0.258$. b) Band structure of H_0 for Sb_2Te_3 at $\gamma = 1.22$ (wider TI). Red (black) bands denote (un-)inverted bands and the respective values for γ correspond to a width of roughly 1 nm for both materials. Even though the width are similar, the shape of the band structures varies significantly. 44
4.3 Periodicity of the gap closure in H_0. Pictured are Bi_2Te_3 (dotted), Bi_2Se_3 (dashed), and Sb_2Te_3 (thick). The gap opens and closes as the strength of the harmonic potential changes. . . . 45
4.4 a) $\hat{S}_z$ expectation values of Bi_2Te_3 at $\gamma = 0.7$. All bands are doubly degenerate with opposite spin projection expectation values. b) The pseudospin projection expectation values are inverted with respect to the spin projection expectation values. All bands are doubly degenerate with negated pseudospin projection expectation values for the bands not pictured. 47

4.5 a) Convergence of band structure energy with increase in dimension of the total Hamiltonian $\mathscr{H}_n$. The dashed lines show the location of n_c. Convergence only occurs after all inverted H_0 bands with $n < n_c$ are included in the simulation. b) Convergence of $\mathscr{H}_n$ eigenvectors. Generally, the eigenvectors converge more slowly and their imaginary argument is subject to the *Mathematica* matrix solving algorithm and not a fixed value for different n. 49

4.6 a) H_0 band structure of Bi_2Se_3 at $\gamma = 0.258$ and b) the band structure for the full Hamiltonian $\mathscr{H}$ at the same γ. The band coupling pushes the lowest band towards zero energy so that the Dirac cone is established even though the gap in the H_0 picture is quite significant. 50

4.7 For Bi_2Te_3 (a) and Sb_2Te_3 (b) the lowest band also forms the Dirac cone due to the coupling of bands. Contrary to Bi_2Se_3, the structures of the bulk bands allow for band crossings and they resemble their respective structure in the H_0 picture. . . . 51

4.8 Establishment of Dirac Cone and band twisting from H_0 (a) to $\mathscr{H}$ (b) in Bi_2Te_3. The crossings indicated by the blue circles in a) turn into anti-crossings and lead to the formation of the Dirac cone. They also lead to a twisting effect between the two bands closest to the Dirac bands. 51

4.9 Dirac wave functions for Bi_2Se_3 and Sb_2Te_3 for $\gamma = 0.1$ and $\gamma = 0.15$, respectively. While the location of the Dirac wave functions tends to the surface with little probability in the center for Bi_2Se_3, the same cannot be said for Sb_2Te_3. 52

4.10 The Dirac wave function densities at $z = 0$ tend to zero with increase in size for both materials. However, for Sb_2Te_3, the density shows periodic behavior in $1/\gamma$. The dashed red lines denote the position ob the gap closures in the H_0 picture. . . . 53

4.11 The three energy bands above the Fermi energy that are energetically closest to the Dirac band show clear bulk-like behavior for Sb_2Te_3 and semi-Dirac behavior for the two bands closest to the Bi_2Se_3 Dirac cone. As the distance to the Dirac cone in terms of energy increases, the Bi_2Se_3 bands become more bulk-like, too. The dotted blue lines depict the wave function densities of the energy band that are, energy wise, closest to the Dirac band. The thick yellow lines represent the second closest bands to the Dirac band and the dashed red lines show the bands third closest to the Dirac band. 53
4.12 Pseudospin projection expectation value distribution for a) Sb_2-Te_3 and b) Bi_2Se_3 at $\gamma = 0.15$ and $\gamma = 0.1$, respectively. While the inverted character of bands is very clear in Sb_2Te_3, it is less clear for Bi_2Se_3. For both materials, the Dirac cone is neutral in $\hat{T}_z$ expectation values. 54
4.13 Spin projection expectation value distribution a) in $\hat{S}_z$ projection and b) in $\hat{S}_x$ projection for Sb_2Te_3. While values for $\hat{S}_z$ in the Dirac cone equal ± 1 at $\mathbf{q} = 0$, the rest of it is spin neutral. Bulk bands are spin up in their z projection expectation values with their respective degeneracy partner being spin down. The $\hat{S}_x$ expectation values are zero for all bands in all materials. . . 55
4.14 Band gap Δ_γ for Bi_2Te_3 and Sb_2Te_3. The dashed red lines depict the gap closures in the H_0 picture. For both materials the oscillation remains but with a slightly increased period of oscillation. 56
4.15 Band gap Δ_γ for Bi_2Se_3 assuming different sets of parameters [99] (left) and [98] (right). While one set leads to gap oscillations like in the other materials, the other set leads to a smooth exponential decay of the gap. 56
4.16 Change of gap behavior with material parameters M_1 and A_0, starting at the set of parameters for Bi_2Se_3 with no gap oscillations. While for M_1 there seems to be a smooth transition between periodic and non-periodic gap, for A_0, any small deviations increasing or decreasing its value lead to a periodic gap. Dashed (dotted) lines indicate the value of A_0 or M_1 for the parameter set with smooth (periodic) gap. 58

4.17 (a) Band structure of Bi_2Te_3 for a width of $\gamma = 0.65$. At this point, the bands of interest in red and blue are still separated and non-degenerate. The "twisting" of the bands occurs due to weak coupling of H_0 obeying two rules: (i) crossings between odd and even bands yield anti crossings, (ii) crossings between the same symmetry remain crossings. (b) The contributions of the oscillator prefactors as function of q_y where the red (blue) band in (a) is represented by the thick (dashed) lines. 59
4.18 (a) Band structure of Bi_2Te_3 for a width of $\gamma = 0.15$. As the TI gets wider from $\gamma = 0.65$ in figure 4.17 to $\gamma = 0.15$ the bands colored in blue and red approach each other energetically and become degenerate. The wave function densities of the four degenerate bands in (b) are equal and lie on top of each other. 60
4.19 The decomposition of the wave function into its oscillator function prefactors for Bi_2Te_3 at (a) $\gamma = 0.15$ and (b) $\gamma = 0.65$. The wave function densities of the four degenerate bands are equal but the decomposition into their oscillator function prefactors shows variations. 60
4.20 (a) The particle-hole asymmetry deforms the H_0 bands which translates directly to the full model in (b). Pictured is Bi_2Te_3 at $\gamma = 0.4$. Notable is the absence of the four-fold degeneracy discussed in section 4.3.3 and the non-linear behavior of the Dirac cones. 61
4.21 The particle-hole asymmetry also leads to the deformation of Bi_2Se_3 at $\gamma = 0.1$ (a) and Sb_2Te_3 at $\gamma = 0.15$ (b). While the cone crossing in Bi_2Se_3 is shifted, the impact on the rest of the band structure is small. The opposite is true for Sb_2Te_3 in which some bulk bands coincide with the Dirac cone. 62
4.22 Shown are the gap oscillations with particle-hole asymmetry present. The dashed blue lines indicate the approximate positions of the gap minima in the particle-hole symmetric system $H_0 + H_{||}$. For both pictured materials the period of oscillations decreases with the introduction of the asymmetry. For Bi_2Se_3 the gap remains non oscillatory. 63

4.23 In contrast to the particle-hole symmetric system (red), the Dirac bands for Sb_2Te_3 with particle-hole asymmetry (blue, dashed) have a non vanishing probability density at the center of the material for $\left|q_y\right| > 0$. 64
4.24 Comparison of the gap oscillations derived in [110] (blue) with the gap behavior obtained with $\mathscr{H}$ (red) for the material parameter set [98] (left) and [99] (right) for Bi_2Se_3. Notable is the lack of gap oscillations for the parameter set [99] in $\mathscr{H}$. 64
4.25 Comparison of the gap behavior derived in [110] (blue) with the gap behavior determined with the full Hamiltonian $\mathscr{H}$ (red) for Bi_2Te_3. Magnitude and oscillations are not in good agreement at all. 65

5.1 Shown are the ratios of the parameters l_μ and l_γ as function of the magnetic field for Bi_2Se_3 (blue), Bi_2Te_3 (red), and Sb_2Te_3 (green, dashed). The impact of magnetic fields on Bi_2Se_3 is much lower than on the other two materials. 77
5.2 Band structure for Bi_2Te_3 (a,b) at $\gamma = 0.4$ and Bi_2Se_3 (c,d) at $\gamma = 0.1$. Notable are the cones being formed in both materials in (b,d) with a magnetic field of magnitude 2 T applied. The impact of the field on Bi_2Se_3 is significantly lower than for Bi_2Te_3 and, in general, the energy splitting in the Dirac bands is larger than in the bulk of the materials. 78
5.3 (a) Pseudospin expectation values for $\hat{T}_z$ in Bi_2Te_3 at $\gamma = 0.4$. (b) Real spin expectation values for $\hat{S}_x$. The expectation values of $\hat{S}_y$ vanish for all bands due to the magnetic field being aligned along the x-axis. For each split cone, right (left) moving particles show spin up (down), respectively. 80
5.4 (a) Pseudospin expectation value plot of Bi_2Te_3 that shows pseudospin expectation value rotation for $\hat{T}_z$ around the split cones along the axis $\mathbf{r}(\theta, \kappa)$ for $\kappa = 0.1\, q_0$ and $\mathbf{q}_0 = (0, 0.1563)\, q_0$. As $\mathbf{r}(\theta, \kappa)$ rotates around the center of the cone, the expectation values of $\hat{T}_z$ oscillate from positive to negative and back. (b) Sketch of the pseudospin rotation within the $\hat{T}_z$-$\hat{T}_x$ plane with the rotation around the cones. 80

5.5 The respective probability densities for the red and blue cone depicted in (a) are pictured in (b). Notable is that the two cones are located on opposite sides of the material which opposes the picture of Weyl cones like in Weyl semimetals. 81
5.6 Probability density for the three band pairs closest to the Dirac band at $q_y = 0.1q_0$ for Bi_2Te_3 and Bi_2Se_3. The dotted blue lines depict the wave function densities of the energy band that are, energy wise, closest to the Dirac band. The thick yellow lines represent the second closest bands to the Dirac band and the dashed red lines show the bands third closest to the Dirac band. With further distance to the Dirac bands the bulk character of the bands increases. 82
5.7 Gap behavior for the cones located at $q_y = 0$. The fact that the periodic gap closure does not occur in the split cones at the Fermi energy while the periodicity is still given for the cones above/below the Fermi energy, suggests that the splitting of the Dirac cone in momentum space can be seen as the result of a Zeeman shift. 83
5.8 The g-factors related to the full numerical Hamiltonian $\mathscr{H}$ are determined by measuring the energy splitting of neighbouring Dirac bands at the origin. 85
5.9 Shown are the effective g-factors of the surface states for Bi_2Se_3 (blue) and Bi_2Te_3 (red) over (a) the width of the material l_γ and (b) over $1/\gamma^{1/2}$ with normalized material parameters. The g-factors of both materials in this model depend on the width of the material and are approximated by (5.58) (dashed lines). . . 85
5.10 Shown is the distance between the cone crossings in momentum space over the width of the material l_γ in Å. The splitting in momentum space follows the same dependencies as the Zeeman splitting in energies. 86
5.11 Band structure of (a) Bi_2Te_3 and (b) Bi_2Se_3 with particle-hole asymmetry present and magnetic field directed in x-direction and of magnitude 2 T. 87

5.12 Wave function densities for bulk bands that are energy wise closest to the Dirac bands for holes (dashed) and electrons (thick) for Bi_2Te_3. While electrons behave like the Dirac states and are located on one side of the material, holes are located on both sides with a preference to one side. As bands further away from the Dirac bands are chosen, this behavior deteriorates towards bulk like band behavior. 88

List of Tables

3.1 Material parameters according to [98] and [99] for all involved materials. In this thesis, the set on the right hand side [99] will be used for the most part. In some cases the left hand side parameter set [98] will be used to underline differences that occur. While the derivation of the parameters in [98] relies on the atomic orbital wave functions and on symmetry considerations and $\mathbf{k} \cdot \mathbf{p}$-theory, the parameters from [99] are derived solely on the basis of $\mathbf{k} \cdot \mathbf{p}$-theory with spinor wave functions derived with the extended linearized augmented plane wave method (ELAPW). 30

4.1 Relevant model parameters of $\gamma_{||}$ for the gap behavior in Bi_2Se_3 for two different sets of material parameters. 57

5.1 Magnetic material parameters according to [98] and [99] for all involved materials. The g factors each have two contributions: the orbital g factor resulting from each atomic orbital and a higher order contribution that can be related to the effective mass [98]. 68

List of Abbreviations

TI	**T**opological **I**nsulator
HO	**H**armonic **O**scillator
QHE	**Q**uantum **H**all **E**ffect
QSHE	**Q**uantum **S**pin **H**all **E**ffect
TR	**T**ime-**R**eversal
TRS	**T**ime-**R**eversal **S**ymmetry

Chapter 1

A History of Physics

The subject of topology is still relatively new in the field of physics. Initial steps have been made in the 1980s after the discovery of the Quantum Hall effect where topological order in a two-dimensional crystalline material leads to quantized conduction along its edges. In general, a topological insulator is described as a crystal structure that exhibits certain symmetries leading to topological properties that cannot be altered easily. The topological properties of a crystal are related to its repetitive microscopic structure. The repetitiveness, however, can never be an infinitely extended feature because boundaries have to be introduced in the real world. But since materials usually are sized at micro-, milli-, or centimeter scales and the repetitiveness is on the scale of a nanometer, repetitions stay in the millions or billions and edge states have not been given much attention before the discovery of topology in physics.

But now, with the focus on edge and surface states, what happens if materials are made wider or thinner? Suppose that a material is shrunk from one centimeter to some hundred nanometer. Repetitions are now at the scale of only a few hundred. Do we expect our initial conditions to still hold? And as the material is made even smaller, repetitions are now down to a few dozen, we can almost be certain for it to break down or at least to be affected significantly. But not only size can be a restriction to topology but also force fields that affect the strict structure of a crystal.

That is the point where this dissertation takes over. What happens to a three-dimensional topological insulator when it is brought to nanometer scales? How does it react to magnetic fields and what does it imply for the physical properties of these fields? In order to understand this, first of all there is the need to understand what topological insulators are and what establishes their properties. After realizing that they have only been discovered a decade ago, one might also wonder why this has not happened earlier since crystals had been studied quantum mechanically for some decades already. Already in the 1960s George Gamow stated that only "number theory and topology still remain purely mathematical disciplines without any applications to physics. Could it be that they will be called to help in our further understanding of the riddles of Nature?" [1]. As it turns out, he was quite right. The physics community was surprised and unprepared for the Quantum Hall effect and, among other concepts, topology was introduced into the field of condensed matter physics.

Outline. This introductory chapter is intended to be a broad overview accessible to the layperson. It serves as a means to classify topological insulators historically by giving a brief history of physics, quantum mechanics, condensed matter physics, and the start of topological condensed matter physics with the discovery of the Quantum Hall effect.

Chapter 2 delves into the fundamental concepts that are necessary to understand topological insulators. It is aimed at general physicists with the wish to get a basic understanding of the topic but may also be approachable for laypersons.

Chapter 3 treats the most recent developments in topological condensed matter physics that lead to the discovery of 3D topological insulators. It also describes properties of topological insulators, gives examples for other physical systems where topology may appear in, and introduces the mathematical model Hamiltonian that is investigated in this thesis.

Chapter 4 shows the mathematical structure of the applied confinement potential and its consequences for band structures and other physical properties of the system. These results have been summarized partially in a separate publication [2].

Chapter 5 then extends the previous results to a confined model with a planar magnetic field applied to it. The results are finally summarized and concluded in chapter 6.

1.1 Classical Condensed Matter Physics

Humphry Davy and Michael Faraday can be seen as the great grand fathers of condensed matter physics. Davy was studying the electrical and thermal conductivity of the elements known at the time and opposed John Dalton's atomic model - since it was related to the periodic table of elements, at the time this was rather considered Chemistry. He also proposed that elements that are not solids at room temperature could be categorized into metals and insulators if methods were found to make them solid. Consequently, he attracted a young Michael Faraday to the "Royal Institution" who turned out to be a gifted experimentalist [3]. Faraday continued Davy's work and got on a journey to find the liquid phases of gases and succeeded for most of them. This then became the field of low temperature physics. Later in the eighteen hundreds (1869), Thomas Andrews studied the reverse transitions (compared to Faraday) of liquids turning into gases and described a critical point [4] during phase transitions at which liquids and gases are indistinguishable which was then explained by Johannes van der Waals by extending the ideal gas law.

Then, after the discovery of the Hall effect by Edwin Herbert Hall in 1879, it was only at the turn of the 19th century when attention was brought back to solids. First by Joseph John Thomson with the prediction and discovery of the electron and then by Paul Drude developing a classical model for electrons in solids, called Drude model today (he also introduced the letter c for the speed of light in the vacuum). At the same time, the earlier developments of quantum mechanics began to take on pace with Planck's solution to the black body problem and Einstein's explanation of the photo electric effect. The classical chapter of condensed matter physics, and also Michael Faraday's great pursuit, was finally closed with Heike Kamerlingh Onnes' liquefaction of Hydrogen and Helium. Another hindsight at a new type of physics was his discovery of superconductivity in mercury in 1911 [5] which was to become one of the most intriguing discoveries in physics history. Drude and Onnes would have to wait quite a few years for the open questions to be addressed.

1.2 Quantum Mechanics

The physics of condensed matter systems did bear notable discoveries during the following years but, after Planck's and Einstein's first contributions to theoretical quantum physics, the Zeitgeist rather pointed towards further developments of the latter. Experimentally, Ernest Rutherford, Arthur Compton, Chandrasekhara Venkata Raman, and Pieter Zeeman discovered the nuclear model of the atom (Rutherford model [6]), the particle property of electromagnetic waves (Compton effect [7]), the wave length shift of light during scattering (Raman scattering [8]), and the splitting of spectral lines of atoms in the presence of magnetic fields (Zeeman effect, 1896), respectively. Rutherford's atomic model served as basis for Niels Bohr's theory of the atomic structure of electrons and nuclei, which is now called the "old quantum theory" and was of more phenomenological nature.

After being brought to a halt due to World War I, the development of the "new" quantum theory started with Louis de Broglie's postulate that "to each bit of energy of the proper mass m_0 there is connected a periodic phenomenon of the frequency ν_0", now being called the particle-wave dualism [9] and basically the opposite of what Einstein did to light with the introduction of the Photon. Meanwhile, Wolfgang Pauli proposed that two electrons that reside within the same physical system cannot occupy the same quantum numbers or quantum states, the Pauli exclusion principle [10]. De Broglie's statement and Pauli's principle inspired Werner Heisenberg and Erwin Schrödinger where the former first introduced the idea of non-commutative operators [11] and consequently the uncertainty principle [12]. The latter delivered one of the most important equations of the 20th and most likely the 21st century, the Schrödinger equation [13]

$$\hat{H}\,\Psi(\vec{r},t) = \left[-\frac{\hbar^2}{2m}\vec{\nabla}^2 + V(\vec{r})\right]\Psi(\vec{r},t) = -\mathrm{i}\hbar\,\partial_t\Psi(\vec{r},t)$$

which describes a probability distribution or wave function $|\Psi(\vec{r},t)|^2$ so that now there was only a certain probability to find a particle anywhere in space instead of the classic view in which particles were assumed to have definite positions. Up until today, it is still used as the framework of non-relativistic microscopic models.

At the same time, sparked by Heisenberg's publication about non-commutative operators and Schrödinger's equation, Paul Dirac developed a theory basing on classical dynamics but with non-commuting fields. He introduced symmetric and anti-symmetric wave functions for indistinguishable particles, already applying the so-called Slater-determinant which was attributed to Slater, even though Heisenberg and Dirac had used their own versions of it three years earlier, and derived and reproduced Fermi-Dirac and Bose-Einstein statistics, respectively [14]. Two years later, in a remarkable publication, he formulated the Dirac equation [15], his equation

$$\left[\alpha_1 p_x + \alpha_2 p_y + \alpha_3 p_z + \beta\right] \Psi(\vec{r}, t) = -\mathrm{i}\hbar\, \partial_t \Psi(\vec{r}, t)$$

which is, at the least, of same importance as Schrödinger's equation and lead to the postulation of the positron, the anti-particle of the electron. For both, the Schrödinger and the Dirac equation, the fact that only the absolute value of the wave function is of interest lead to the belief that a complex phase factor $\mathrm{e}^{i\varphi}$ would leave the physical state invariant. Later on, after the discovery of the Quantum Hall effect, it was realized that the phase factor can indeed be impactful on the physical system.

1.3 Condensed Matter Physics

Roughly three decades after Drude had developed his model of classical kinetic electron transport in metals and after quantum mechanics had been established, it was Arnold Sommerfeld who applied one of the recent discoveries, Fermi-Dirac statistics, to the Drude model in 1927. Maybe Sommerfeld can be seen as the grand father of modern condensed matter physics - he was famous for his teaching and an astonishing number of his students' names are still persistent within the field. Pauli developed the theory of paramagnetism, already in 1926. Léon Brillouin introduced the Brillouin zone in his quantum theory of solids and later works around 1930. Max von Laue, already in 1912, had shown diffraction patterns for X-rays in crystal lattices. Felix Bloch, not a student of Sommerfeld but of Werner Heisenberg (who used to be one of Sommerfeld's students), embedded quantum mechanics into the periodicity of crystal lattices in 1928. Instead of applying the Schrödinger equation to the whole lattice with huge numbers of electrons, he realized that the problem could be simplified by dividing the wave functions and potentials into a part $u(\vec{r})$ periodic in $\vec{r}$ and a part that describes the crystal momentum $\mathrm{e}^{\mathrm{i}\vec{k}\vec{r}}$ to get an effective Schrödinger equation with Bloch functions instead of wave functions

$$\left[\left(\frac{\hbar^2 k^2}{2m} - E\right) - \frac{\hbar^2}{2m}\vec{\nabla}^2 + V(\vec{r})\right] u_{\vec{k}}(\vec{r}) = 0.$$

As a result, with this theory of energy bands in solids, first band structure calculations were conducted. Bloch's theorem would also become important later on for the characterization of topology in crystals. Ernst Ising, a student of Wilhelm Lenz, provided the model of the Ising spin chain

$$H = -\sum_{ij} J_{ij} S_i S_j$$

that, through contributions by Felix Bloch, Rudolf Peierls, Louis Néel, and Lars Onsager, enabled the microscopic understanding of magnetism and also the explanation of phase transitions between ferromagnetic and paramagnetic states of solids.

However, many other contributions came from different schools of physics all over the world. Lawrence Bragg derived a simple formula that enabled the mapping of crystal structures, the Bragg equation. Together with Carl Hermann and Max von Laue he also was the first author of "International Tables for Crystallography" in 1935, which made systematic crystal structures available to the whole physics community. In the same year, an early attempt at a theory for superconductivity was made by Fritz and Heinz London [16] - it successfully explained the Meissner effect but failed to deliver a microscopic picture of superconductivity. Also in the same year, Lev Landau investigated the quantum effects of magnetic fields and developed the framework of Landau quantization. Landau was incredibly productive. Two years later, in 1937, Landau introduced a theory of phase transitions [17] which he would modify with the help of Vitaly Ginzburg after World War II in 1950. Another valuable contribution was made by him in 1956, the (Landau-)Fermi liquid theory of interacting fermions in metals. Much later, his theory of phase transitions would be extended by topological phases which can't be explained in the frame of his theories.

Parts of the riddle of superconductivity was finally solved by John Bardeen, Leon Cooper, and John Schrieffer in 1965. They pictured the essential feature of a superconductor to be Cooper pairs - pairs of electrons that are formed due to phonon-phonon interactions within superconducting materials. These pairs of fermions effectively behave like bosons and condense into a superconducting state with no resistivity. One year earlier, a new problem was formulated by Jun Kondo [18] which would take ten years to be explained by Kenneth Wilson in 1975 [19]. The Kondo effect describes a material state where magnetic impurities lead to increased resistivity at low temperatures.

In 1971, Dyakonov and Perel proposed a spin version of the Hall effect, the last Hall effect to be explained with only quantum mechanics [20, 21]. This effect involves accumulation of opposite spin on opposite boundaries in a charge carrying sample and a resulting spin current instead of a charge current - thus being called the Spin Hall effect. Later on, this effect was further categorized into an extrinsic Spin Hall Effect relying on spin dependent scattering off impurities [22] and an intrinsic Spin Hall Effect due to spin-orbit coupling in the band structure of electrons [23].

1.4 Topological Condensed Matter Physics

Roughly 100 years after the first discovery of the Hall Effect, in 1980, Klaus von Klitzing, Gerhard Dorda, and Michael Pepper found that the Hall conductance in very strong magnetic fields can be measured in multiples of the inverse Klitzing constant $\frac{e^2}{h}$ [24]. Due to the magnetic field the band structure of the probe splits into Landau levels. Variation of the field also changes the number of electrons the energy levels can carry and, therefore, if the magnetic field is strong enough, all conduction electrons will be concentrated in one level. Consequently, all these electrons will have the same energy and a cyclotron frequency $\omega_c = \frac{eB}{m}$. Semi-classically, the electrons close to the boundaries of the sample will bounce off the edges forming conduction channels while the electrons in the bulk will travel on circular orbits. For each filled Landau level there is one conduction channel contributing e^2/h to the conductance. Introducing the filling factor ν as the number of filled Landau bands, the total Hall conductance then is $\sigma_H = \nu e^2/h$. It was realized that ν is a topological invariant. First, Robert Laughlin showed that the quantization of the Hall conductance is a consequence of gauge invariance in combination with the existence of a mobility gap [25]. This was given further justification by David Thouless et al. by explicitly considering a two-dimensional electron gas in a uniform magnetic field in a periodic lattice structure with the Fermi energy lying in a gap [26]. In 1982, Bertrand Halperin showed that, in a strong magnetic field, charge carriers that are located within roughly one cyclotron radius of the edges of the sample serve as current generators while charge carriers in the bulk do not contribute [27]. Meanwhile, Michael Berry was studying adiabatic changes to quantum systems. He pointed out that the phase of quantum states $e^{i\varphi}$ cannot be assumed to be irrelevant when the system goes through a series of adiabatic changes. Instead, the wave function picks up an additional geometrical phase factor that depends on the path of these adiabatic changes [28], the Berry phase factor $e^{i\gamma_c}$. This sparked the first connection of physics and topology that had been anticipated by George Gamow in the 1960s. Just a few months after Berry's findings, Barry Simon showed that Berry's geometrical phase factor is a "holonomy in a Hermitian line bundle since the adiabatic theorem naturally defines a connection in such a bundle" [29]. He also showed the natural connection to the findings of Thouless et al. a year earlier and that, in fact, the Hall quantization is not a consequence of the Hamiltonian of the system but a result of the phase space the system's parameters live in. Finally, Franck Wilczek and Anthony Zee showed that Berry's and Simon's constructions would lead to non-abelian gauge fields during the adiabatic evolution of quantum mechanical systems [30].

The Quantum Hall effect is the first example of a bulk-boundary correspondence which means that the material's bulk structure is responsible for a non trivial behavior at the boundary. In the same year Tsui, Stormer, and Gossard found plateaus similar to the resistivity plateaus in the QHE, but for fractional filling factors $\nu = \frac{1}{3}, \frac{2}{3}, \frac{1}{5}, ..$, soon to be known as the fractional Quantum Hall effect. However, this is not a manifestation of a new aspect of the Quantum Hall effect but rather a result of electron-electron interaction forming quasi particles that replace the electrons in Klitzing's Quantum Hall effect [31].

A few years later, in 1988, Duncan Haldane proposed a model of "2D graphite" - a honeycomb lattice with two sub lattice sites that exchange places under rotations around the Brillouin zone center (today's Graphene). In contrast to Gordon Semenoff, who had studied this lattice structure before [32], Haldane not only considered nearest neighbour hopping of electrons between the two types of sites due to the two sub lattices, but also next neighbour hopping enabling electrons to stay within their sub lattice. Furthermore, he considered a time-reversal breaking periodic local magnetic flux density that introduces chirality to the Hamiltonian with different effective electron masses on each sub lattice. If these electron masses were to have opposite signs, the Landau filling factor of the time-reversal invariant version of the model (where the local magnetic flux is zero) differs from the time-reversal breaking version by one, meaning that the time-reversal breaking model exhibits quantized conductance just like in the Quantum Hall effect [33]. Haldane's model was a milestone during the establishment of topological condensed matter physics and it is further examined in section 2.5.1. The Haldane model is the equivalent to the classical anomalous Hall effect and further developments found that this quantum anomalous Hall effect can also be realized in ferromagnetic insulators with strong spin-orbit coupling which was finally done in the year 2013 [34].

Also in 1988, Barry Simon published the continuation of his earlier work that was connecting Michael Berry's geometrical phase with the TKNN integer. He succeeded to put this integer into a framework of topological invariants in fermion systems with time-reversal invariance by realizing that it could be associated with the first Chern number [35].

The developments in the 1980s laid the foundations for today's topological condensed matter physics. The ideas established at the time are necessary for the understanding of topological insulators and will be presented in the next chapter.

Chapter 2

Topological Insulator Fundamentals

The topic of topological insulators is a complicated one. It involves mechanisms from different areas of physics and mathematics and it gets tangled very fast, especially when diving into the topic while coming from fields that are only marginally related. This chapter is written with the intent to prevent drowning after the dive.

In order to understand the significance of topology in topological insulators, there are a few concepts and basics that have to be addressed first. To put it very general, solids with crystalline structure are invariant under a set of symmetry transformations. This leads to a repetitive behavior within the crystal that is summarized in the concept of the Brillouin zone. External or internal fields can then induce a current in the material that, in part, depends on an integral over and, therefore, on the form of the Brillouin zone. This is described by the Berry phase (or geometric phase). The Berry phase, however, not only captures properties of specific crystal symmetries (like translation invariance) but allows for any parameter of the underlying mathematical model that can be altered adiabatically to have a direct influence on the properties of the whole material. While perfect crystal symmetries are disturbed quite easily by defects in the crystal, there are other symmetries that can be disturbed or broken less easily. This means that the resultant topological structure and properties of the crystal are stable and it can lead to unique properties. It is the intend of the following sections to lay out this quick explanation in more detail.

2.1 Characterization of Crystal Structures in Physics

A crystal consists of a number of atoms that obey repetitive arrangements. In contrast to this are amorphous materials that are not arranged in any specific way, apart from, for example, the average distance between atoms. An example of a crystal in two dimensions could be a square lattice of identical atoms where each atom has the same distance to its nearest neighbours. In general, each lattice site in a crystal can be described as a linear combination of base vectors

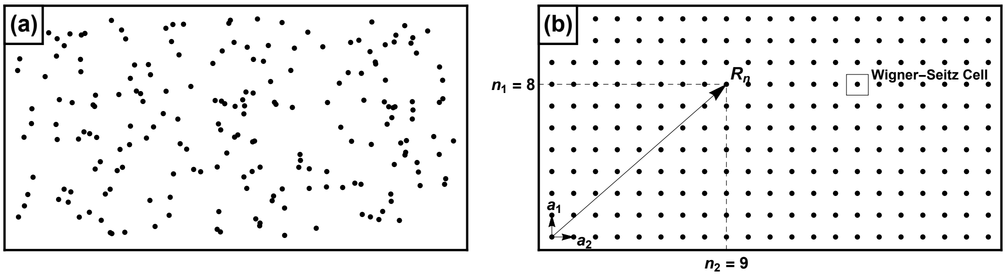

Amorphous Material **Crystalline Material**

FIGURE 2.1: (a) An amorphous material with no clear structure (i.e. glass). (b) The structure of a 2D crystal with a square lattice. The definition of the lattice vector $\mathbf{R}_n$ allows access to every lattice site. The region indicated by a square around a lattice point is called the Wigner-Seitz cell or Brillouin zone in the reciprocal lattice.

$$\mathbf{R}_n = \sum_{i=1}^{d} n_i \mathbf{a}_i \tag{2.1}$$

where n_i are integers and d represents the dimension of the lattice. The base vectors $\mathbf{a}_i$ do not necessarily have to be orthogonal but can take on any form as long as they still span the according space in terms of dimensions and as long as their according unit cell can fill the material without intermediate spaces. The unit cell is spanned by the base vectors and, due to the previous restrictions, crystals in three dimensions are limited to the fourteen Bravais lattices [36]. The fourteen Bravais lattices describe all the lattice structures that are possible in three dimensions. Another important concept is the Wigner-Seitz cell which is depicted in figure 2.1b and can be defined as the set of all points that is closer to one lattice point than to any other lattice point.

One of the fundamental properties of crystals are their symmetries regarding translations with respect to their base vectors as well as rotations or reflections. For example, considering figure 2.1b, for an infinite lattice, a translation from any lattice site to another lattice site would leave the lattice invariant. The same is true for a rotation of 90°, 180°, or 270° of the whole lattice around any lattice site. These symmetry transformations are gathered to form the symmetry group of crystal lattices which contains 48 symmetry transformations. Each possible Bravais lattice obeys only a subset of the symmetry group.

The base vectors have the dimension of length. However, for most applications, the Fourier transform of the lattice vectors is more convenient. For this reason, the reciprocal base vectors are defined in three dimensions as

$$\mathbf{b}_1 = \frac{2\pi}{V}(\mathbf{a}_2 \times \mathbf{a}_3),\ \mathbf{b}_2 = \frac{2\pi}{V}(\mathbf{a}_3 \times \mathbf{a}_1),\ \text{and}\ \mathbf{b}_3 = \frac{2\pi}{V}(\mathbf{a}_1 \times \mathbf{a}_2) \tag{2.2}$$

where V is the volume of the unit cell and, as equivalent to $\mathbf{R}_n$, the reciprocal lattice vector is defined as

$$\mathbf{G} = k_1\mathbf{b}_1 + k_2\mathbf{b}_2 + k_3\mathbf{b}_3. \tag{2.3}$$

Opposed to the regular lattice base vectors, the reciprocal base vectors bear the unit of inverse length and, as such, are compatible with wave numbers or wave momenta. This is because the maximum wave number allowed by the lattice in real space is given by the minimum wave length fitting within one lattice spacing. Thus, all possible crystal momenta fit within one Wigner-Seitz cell which is called the first Brillouin zone for the reciprocal lattice.

Periodic Boundaries and Bloch Theorem

The importance of the Brillouin zone for the fundamentals of topological insulators lies within the fact that, when moving from one zone to the adjacent zone, it is mathematically equivalent to entering the first zone from the opposite side. This originates from the periodicity of the lattice and the assumption that macroscopic materials are large enough and that lattices can be assumed to extend to infinity or satisfy periodic boundary conditions. For example, if there is a lattice with periodic boundary conditions with N sites in the direction of one basis vector, moving one site further from $n = N$ will end up at the other side of the lattice, $n = 1$. Usually, this is also the case for any function f of interest on the lattice. If any f satisfies the periodic boundary conditions, the relation

$$f(\mathbf{R}_n) = f(\mathbf{R}_n + N_i\mathbf{a}_i) \tag{2.4}$$

holds. f can be applied to reciprocal space by making use of its Fourier transform

$$f(\mathbf{k}) = \sum_n f(\mathbf{R}_n)\mathrm{e}^{-i\mathbf{k}\mathbf{R}_n} \text{ and } f(\mathbf{R}_n) = \frac{1}{N}\sum_{\mathbf{k}} \mathrm{e}^{i\mathbf{k}\mathbf{R}_n} f(\mathbf{k}). \tag{2.5}$$

Because any point in the lattice can be accessed by addition of a reciprocal lattice vector $\mathbf{k} + \mathbf{G}$, it suffices to determine these relations only for the $\mathbf{k}$ within the first Brillouin zone since $\mathbf{G}\mathbf{R}_n = 2\pi$ and $e^{i\mathbf{G}\mathbf{R}_n} = 1$.

When considering the Hamiltonian of an actual physical system, this property also comes into play if the involved functions fulfill the same periodicity as the lattice. For example, with a translation invariant potential $V(\mathbf{r}) = V(\mathbf{r} + \mathbf{R}_n)$ and the Schrödinger equation

$$\left(-\frac{\hbar^2}{2m}\nabla^2 + V(\mathbf{r})\right)\Psi(\mathbf{r}) = E\Psi(\mathbf{r}), \tag{2.6}$$

it follows that any eigenfunction $\Psi(\mathbf{r})$ does not have to satisfy translation invariance but can pick up a phase factor $\mathrm{e}^{i\mathbf{k}\mathbf{R}_n}$ and thus

$$\Psi(\mathbf{r} + \mathbf{R}_n) = \mathrm{e}^{i\mathbf{k}\mathbf{R}_n}\,\Psi(\mathbf{r}) \tag{2.7}$$

which is called the Bloch condition. With the definition of the Bloch functions

$$u_{\mathbf{k}}(\mathbf{r}) = \mathrm{e}^{-i\mathbf{k}\mathbf{r}}\,\Psi_{\mathbf{k}}(\mathbf{r}), \tag{2.8}$$

it follows that eigenfunctions of the Schrödinger equation can be expressed in terms of translation invariance fulfilling Bloch functions

$$\Psi_{\mathbf{k}}(\mathbf{r}) = \mathrm{e}^{i\mathbf{k}\mathbf{r}}\,u_{\mathbf{k}}(\mathbf{r}). \tag{2.9}$$

This is called the Bloch theorem.

2.2 Characterization of Topology in Mathematics

Historically, topology initially was a part of geometry and it started being accepted as an independent field of mathematics between the late 1800s and early 1900s. Topology is now a major area within mathematics and it deals with the study of abstract spaces and their properties. Important with respect to condensed matter physics is the study of geometrical objects in two, three, and four dimensions, such as tori or spheres. Fundamentally, from the geometric point of view, "topology may be regarded as the study of those properties of geometric figures that remain invariant under single-valued continuous mappings possessing single-valued continuous inverses" [37]. This refers to homeomorphisms which are defined as a mapping f so that:

- f is a bijection (each function parameter x is associated with exactly one function value $f(x)$)
- f is continuous
- the inverse function f^{-1} is continuous.

An example for this would be $f(x) = x^3$ which is a bijection, continuous, and its inverse $f^{-1}(x) = x^{1/3}$ is continuous. Homeomorphisms are essential for distinguishing between topological objects and they are not the topological objects of interest themselves. From the example in figure 2.2a, it is apparent

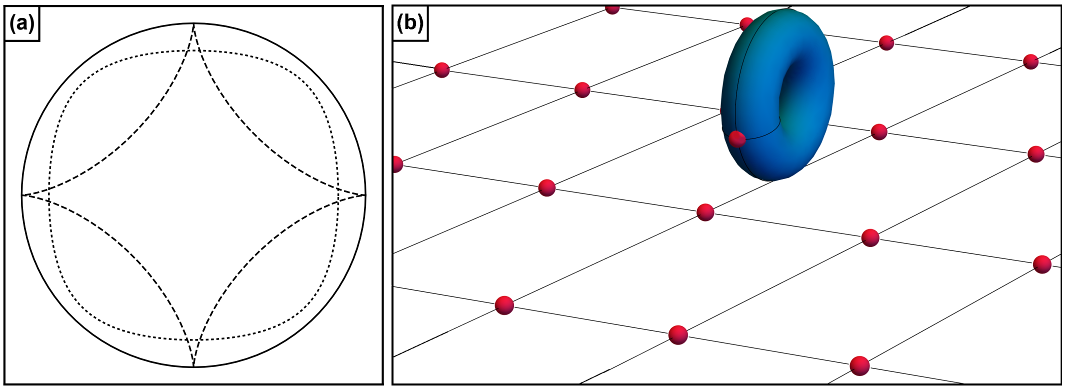

FIGURE 2.2: (a) All three displayed objects are topologically equivalent. The dashed (dotted) shapes are deduced by applying the homeomorphisms $f(x,y) = (x^3, y^3)$ ($f(x,y) = (\mathrm{Sin}(x), \mathrm{Sin}(y))$) to each coordinate of the circle (thick line). (b) A torus generating a 2D lattice of atoms (in red) by rotating along the lines and the atom indicated on the torus' surface.

that homeomorphisms not necessarily conserve the proportions of the objects they are applied to. This is because the actual distance between points in a topological object is not of concern - a classic metric, like the absolute value of a vector $\mathbf{v}$, $|\mathbf{v}|$, is not defined or not of interest in Topology. Thus, the deformation of a coffee cup into a torus is just an example of a homeomorphic deformation. And because the homeomorphic deformation is possible, the two objects are topologically equivalent.

Another way to distinguish between topological objects is the Euler characteristic χ. It captures the shape of the respective topological space and is invariant under any homeomorphic deformations. Oversimplified, it can be viewed as a measure for how many holes an object has. Consider the 3D plastic versions of the three characters "8", "O", and "c". The "c" does not have any hole and can be deformed to a sphere, its Euler characteristic is $\chi_c = 2$. The "O" basically represents a torus with one hole and thus $\chi_O = 0$. And the "8" is a double torus with two holes and $\chi_8 = -2$ (a n-holed torus has $\chi_n = 2 - 2n$). Even though, at first glance, this correspondence seems arbitrary, there is a system called Conway symbols of orbifolds, which is closely related to symmetry groups in crystal structures, enabling the derivation of an object's Euler characteristic.

The Euler characteristic relates topological spaces to their Gaussian curvature K. This is summarized in the Gauss-Bonnet theorem

$$\int_M \mathrm{d}\mathbf{S}\,\mathbf{K} + \int_{\partial M} \mathrm{d}s\, k_g = 2\pi\chi(M) \tag{2.10}$$

where M is a manifold representing the topological object of interest. The first part is a surface integral over the Gaussian curvature. The second part only is significant if the manifold has an open boundary. It is a line integral around an open boundary ∂M.

The initial question, how topology and crystal structures are related, can now be answered. Taking a 2D lattice as example, because the crystal lattice is repetitive and going from one crystal cell to the next is equivalent to entering the first cell from the opposite side, the path through a lattice is periodic and can be represented by a circle. In 2D, this is possible in two directions, hence the lattice can be described by two circles in its parameter space. Combining the two circles into one object will give an object that resembles a torus. The torus can be viewed as the generator of the lattice and is pictured in figure 2.2b. It can be used as a "stamp", printing the lattice onto a 2D surface while rolling through space along its two circles in parameter space. The torus is here the most simple example and only covers two parameters but can be generalized to any number of parameters. The topological aspect of crystal lattices is that many lattices may result in the same topological "stamp" representing them.

2.3 The Berry Phase

The Berry phase is a concept derived by Michael Berry [28] when studying the quantum adiabatic theorem and it is also referred to as geometric phase because it is crucially dependent on the geometry of the underlying structure. The relation between the Berry phase and the Quantum Hall effect was subsequently pointed out by Barry Simon [29], describing it as a result of holonomy of the underlying manifold.

The quantum adiabatic theorem was first proved by Max Born and Vladimir Fock [38]. It states that if a Hamiltonian is changing in time sufficiently slowly and the system initially begins close to an eigenstate, then the system remains close to an eigenstate with evolution of time. This can be expressed in terms of a Hamiltonian with a set of parameters $\mathbf{R}(t)$ that is time dependent $H(\mathbf{R}(t))$. The system is assumed to go through a cycle c from $t = 0$ to $t = T$ where $\mathbf{R}(T) = \mathbf{R}(0)$ and c describes the motion described by the vector $\mathbf{R}(t)$ with passing time. At any given time the system is characterized, up to a phase uncertainty, by its Schrödinger equation

$$H(\mathbf{R}(t))|u_n(\mathbf{R}(t))\rangle = E_n(\mathbf{R}(t))|u_n(\mathbf{R}(t))\rangle \tag{2.11}$$

where the quantum number n is related to the Energy eigenvalues of the Bloch functions $|u_n\,(\mathbf{R}(t))\rangle$. However, this equation does not capture the time evolution of the system. For this, the full time dependent Schrödinger equation

$$i\hbar\partial_t|\Psi(t)\rangle = H(\mathbf{R}(t))|\Psi(t)\rangle, \tag{2.12}$$

where the wave functions are time dependent explicitly, has to be considered. Comparison with (2.11) delivers an expression for the full wave function in terms of the Bloch functions $|u_n(\mathbf{R}(t))\rangle$

$$|\Psi(t)\rangle = \mathrm{e}^{i\gamma_C(t)}\mathrm{e}^{i\phi(t)}|u_n(\mathbf{R}(t))\rangle \tag{2.13}$$

where $i\phi(t) = -i/\hbar \int_0^t \mathrm{d}t' E_n(\mathbf{R}(t'))$ contains the regular energy terms and γ_c, the quantity of interest, depends on a line integral along c

$$\gamma_c = \oint_c \mathrm{d}\mathbf{R}\ \mathbf{A}_n(\mathbf{R}) \quad \text{with} \quad \mathbf{A}_n(\mathbf{R}) = i\langle u_n(\mathbf{R}(t))|\boldsymbol{\nabla}_{\mathbf{R}}|u_n(\mathbf{R}(t))\rangle. \tag{2.14}$$

γ_c is called Berry phase and $\mathbf{A}_n(\mathbf{R})$ is called the Berry vector potential. The Berry phase can be rewritten as surface integral

$$\gamma_c = \int_M \mathrm{d}\mathbf{S}\ \boldsymbol{\nabla}_{\mathbf{R}} \times \mathbf{A}_n(\mathbf{R}) = \int_M \mathrm{d}\mathbf{S}\ \boldsymbol{\Omega}^n(\mathbf{R}) \tag{2.15}$$

where M represents the manifold describing the surface spanned by the path c. This resembles the Gauss-Bonnet theorem from (2.10) and $\boldsymbol{\Omega}^n(\mathbf{R})$ is interpreted as an equivalent to the Gaussian curvature K in topology and is called Berry curvature. Considering the definition of $\mathbf{A}_n(\mathbf{R})$, the Berry curvature can be expressed in terms of the Bloch functions of the Hamiltonian as

$$\boldsymbol{\Omega}^n(\mathbf{R}) = \mathrm{Im} \sum_{m \neq n} \frac{\langle u_{n\mathbf{k}}|\boldsymbol{\nabla}_{\mathbf{R}} H(\mathbf{R})|u_{m\mathbf{k}'}\rangle \times \langle u_{m\mathbf{k}'}|\boldsymbol{\nabla}_{\mathbf{R}} H(\mathbf{R})|u_{n\mathbf{k}}\rangle}{(E_m - E_n)^2} \tag{2.16}$$

where $|u_{nk}\rangle$ are Bloch functions with momentum indices as in (2.8). In terms of the components R^μ of the set of parameters $\mathbf{R}(t)$ the Berry curvature tensor can be written as

$$\boldsymbol{\Omega}^n_{\mu\nu}(\mathbf{R}) = -2\,\mathrm{Im} \sum_{m \neq n} \frac{\langle u_{n\mathbf{k}}|\partial_{R_\mu} H|u_m\rangle\langle u_{m\mathbf{k}'}|\partial_{R_\nu} H|u_{n\mathbf{k}}\rangle}{\big(E_m(\mathbf{k}') - E_n(\mathbf{k})\big)^2}. \tag{2.17}$$

Now that the connection between topology, crystal symmetries, and Hamiltonian systems has been established, what is left is to find the last link to an application of the previous derivations.

2.4 Quantum Hall Effect

The Quantum (charge) Hall effect was the experimental discovery setting off the first developments in topological condensed matter physics. It takes place in the setting of a flat, effectively two-dimensional, material that is penetrated by a strong magnetic field and that is carrying a small current. For magnetic fields strong enough, the Hall conductivity is then quantized with the number of occupied Landau levels ν. A sketch of the flat material and

FIGURE 2.3: (Left) Sketch of a flat material with conducting channels on its edges where the magnetic field is perpendicular to the material plane [39] and (right) example data showing quantized steps in resistance with varying magnetic field strength [40]. R_H is the Hall resistance associated with the conductivity σ_{xy} or σ_H and R_{xx} is the resistivity associated with σ_{xx}. The edge channels are not spin sensitive.

experimental results for the Quantum Hall Resistance are shown in figure 2.3.

The Hall conductivity σ_{xy} for an initial current in x direction that leads to a current in y direction can be determined by making use of the Kubo formula [41] which describes the linear response of a Hamiltonian to a small time dependent oscillating electric field

$$\sigma_{xy}(\omega+i\delta) = \frac{i}{\omega+i\delta}\frac{1}{V}\frac{1}{Z_0}\sum_{n,m}\frac{\langle n|j_x|m\rangle\langle m|j_y|n\rangle}{\hbar\omega+i\delta+E_n-E_m}\left(\mathrm{e}^{-\beta E_n}-\mathrm{e}^{-\beta E_m}\right). \tag{2.18}$$

A second term, called the diamagnetic term, is omitted due to it being applicable only to diagonal elements of σ_{ij}. ω is the frequency of the oscillating electric field, Z_0 is the partition function associated with the unperturbed Hamiltonian, and $|n\rangle$ are eigenstates of the unperturbed Hamiltonian with their respective energy eigenvalues E_n. For Bloch waves, $\omega \to 0$, $T \to 0$, and by making use of

$$\frac{1}{\hbar\omega+E_n+E_m} = \frac{1}{E_n-E_m}\left(1-\frac{\hbar\omega}{E_n-E_m}\right)+\mathcal{O}(\omega^2), \tag{2.19}$$

the Hall conductivity can be expressed as

$$\begin{aligned}\sigma_{xy} =& \mathrm{Im}\frac{2e^2}{\hbar}\sum_{n,m,\mathbf{k},\mathbf{k}'}\frac{\langle u_{n\mathbf{k}}|v_y|u_{m\mathbf{k}'}\rangle\langle u_{m\mathbf{k}'}|v_x|u_{n\mathbf{k}}\rangle}{(E_n(\mathbf{k})-E_m(\mathbf{k}'))^2}\\ =& -2\,\mathrm{Im}\frac{e^2}{\hbar}\sum_{n,\mathbf{k}}^{E_n<E_F}\sum_{m,\mathbf{k}'}^{m\neq n}\frac{\langle u_{n\mathbf{k}}|\partial_{k_x}H|u_{m\mathbf{k}'}\rangle\langle u_{m\mathbf{k}'}|\partial_{k_y}H|u_{n\mathbf{k}}\rangle}{(E_n(\mathbf{k})-E_m(\mathbf{k}'))^2}\\ =& \frac{e^2}{h}\frac{1}{2\pi}\sum_{n}^{E_n<E_F}\int_{BZ}\mathrm{d}\mathbf{k}\,\boldsymbol{\Omega}^n_{xy}\end{aligned} \tag{2.20}$$

where the summation excludes $n = m$ and n only runs over occupied states with $E_n < E_F$. E_F is the Fermi energy. The summations over wave vectors has been converted to an integral over the Brillouin zone in the final step. Here lies the connection between the Quantum Hall conductivity and the Berry phase/curvature. The QH conductivity can be expressed in terms of the Berry curvature given in (2.17). It crucially depends on the integral and, thus, on the shape of the Brillouin zone. In the case of the Quantum Hall conductance, the integral equals 2π and the summation over n, where only the ν occupied (Landau) bands are considered, then contributes a factor of ν. Hence, the conductivity for the integer Quantum Hall effect is

$$\sigma_{xy} = \nu \frac{e^2}{h}. \tag{2.21}$$

It is quantized because each occupied Landau band opens up exactly one 1D channel for electron transport. ν is called the first Chern number and it is a topological invariant.

2.5 Quantum Spin Hall Effect

A crucial concept for the Quantum Spin Hall effect is that of time-reversal symmetry (TRS). The action of time-reversal is represented by the replacement of the parameters for time, $t \rightarrow -t$. If a system's state is invariant under this transformation, it is called time-reversal invariant. time-reversal symmetry is related to entropy in that, if a system is time-reversal invariant, the entropy of the system does not change. Hence, on the macroscopic scale, time-reversal symmetry is in conflict with the second law of thermodynamics. On the microscopic scale, TRS is a symmetry present in quantum mechanical systems where the seeming paradox of TRS in the quantum world but TR asymmetry on the macroscopic scale is resolved by the fluctuation theorem of statistical mechanics.

Time-reversal symmetry in quantum mechanics has an important effect on fermions described by the Kramers theorem. If a Hamiltonian H is invariant under time-reversal T, $[H, T] = 0$, then for each state of the Hamiltonian $|\Psi\rangle$ there exists a second state $T|\Psi\rangle$ that bears the same energy because $HT|\Psi\rangle = TH|\Psi\rangle = ET|\Psi\rangle$, where E is the energy of the original state $H|\Psi\rangle = E|\Psi\rangle$. The two states $|\Psi\rangle$ and $T|\Psi\rangle$ are called a Kramer or TRS pair. For condensed matter systems these two states usually are distinguishable by their respective values in momentum space which take opposite sign. An exception to this is when the wave vector equals zero for which both states have the same momentum. In the absence of spin-orbit coupling, Kramers degeneracy simply describes the usual spin up/spin down degeneracy that can be lifted by a magnetic field and results in Zeeman splitting.

2.5.1 The Haldane Model

An important step towards the theoretical development of the Quantum Spin Hall effect was a model introduced by Duncan Haldane [33]. He constructed a model on a honey-comb lattice with sub-lattices A and B that features nearest- and next-nearest-neighbour hopping represented by the respective hopping amplitudes t_1 and t_2 with a position dependent magnetic flux density that averages to zero over the whole unit cell but with opposite signed fluxes for different regions within the cell. Hopping due to the next nearest neighbour hopping t_2 acquires a phase ϕ while hopping around the whole cell with nearest neighbour hopping t_1 acquires no phase. Essentially being a Graphene model with additional next nearest neighbour hopping, the resulting tight binding Hamiltonian shows two distinct points in the k_x-k_y plane at which the gap is closed, $\mathbf{K}_\tau$ where $\tau \in \{-1, 1\}$, if none of the symmetry breaking terms are present. An expansion of the Hamiltonian to linear order around these two points results in a Dirac-like Hamiltonian for each point

$$H_\tau = \begin{pmatrix} m_\tau & \hbar v_F(\tau k_x - i k_y) \\ \hbar v_F(\tau k_x + i k_y) & -m_\tau \end{pmatrix} \tag{2.22}$$

where v_F is the Fermi velocity and $m_\tau = M - 3\sqrt{3}\tau t_2 \sin(\phi)$ with M being an on-site energy, positive for A sites and negative for B sites. m_τ is present due to the next nearest neighbour hopping and represents an effective mass within the picture of the Dirac Hamiltonian. The eigenenergies of (2.22) are given by $E^\tau_\pm(\mathbf{k}) = \pm\sqrt{(\hbar v_F \mathbf{k})^2 + m_\tau^2}$. The terms m_τ break time-reversal symmetry and inversion symmetry of the original Graphene model and, without it, the dispersion would form a Dirac cone. Suppose now that a film of material governed by the Haldane model in the region $M - 3\sqrt{3}\tau t_2 \sin(\phi) < 0$ is side by side with the same model but where the complex next nearest neighbour hopping term t_2 is zero. If the x axis serves as edge between the two layers and $t_2 \neq 0$ for $y < 0$, and if the function for the mass

$$m(y) = \begin{cases} M - 3\sqrt{3}\tau t_2 \sin(\phi) & y \leq 0 \\ M & y > 0 \end{cases} \tag{2.23}$$

at the edge of the two materials is continuous, then it needs to cross zero around $y = 0$. The Fourier transformed Hamiltonian of the system can then be represented by ($\hbar v_F = 1$)

$$H(x,y) = \begin{pmatrix} m(y) & -(i\partial_x + \partial_y) \\ -(i\partial_x - \partial_y) & -m(y) \end{pmatrix} \tag{2.24}$$

which results in a wave function located at the boundary of the two regions

$$\psi_{k_x}(x,y) \propto \mathrm{e}^{ik_x x} \mathrm{e}^{-\int_0^y \mathrm{d}y\, m(y')} \tag{2.25}$$

with the linear dispersion $E(q_x) = E_F + \hbar v_F q_x$. $|\psi_{k_x}(y)|^2$ and $m(y)$ are plotted in figure 2.4. The model thus has two topologically distinct regions that can be associated with a topological integer $\nu \in \{0, \pm 1\}$. When inversion symmetry is broken, a gap opens and the system becomes a regular semiconductor with $\nu = 0$. But if TRS is also broken the system ends up in a state with $\nu = \pm 1$ and becomes an integer Quantum Hall state. This model derived by Duncan Haldane is now referred to as a Chern insulator or the Quantum Anomalous Hall effect.

FIGURE 2.4: (left) Localization of the wave function at the interface of a trivial and a non-trivial Haldane system where $m(y)$ is approximated as a continuous function through $m = 0$ [42]. (right) Predicted edge state dispersion of Quantum Spin Hall state in Graphene as proposed by Kane and Mele [43].

2.5.2 The Kane-Mele Model

The Kane-Mele model refers to work of Charles Kane and Eugene Mele who were first to construct a model that predicted the Quantum Spin Hall effect [43, 44]. They combined two time-reversal conjugate copies of the Haldane model, one for spin up electrons exhibiting $\nu = +1$ and one for spin down electrons with $\nu = -1$. In this setup, the two copies cancel each others'

FIGURE 2.5: (Left) Sketch of a flat material with conducting channels on its edges due to the Quantum Anomalous Hall effect and (right) sketch of a flat material with conducting channels on its edges due to the Quantum Spin Hall effect where the edge channels are spin sensitive [39].

Quantum Anomalous Hall effect that was determined in the previous section. A sketch of the Quantum Anomalous Hall effect and the Quantum Spin Hall effect can be seen in figure 2.5. But a calculation for the spin current instead of the charge current results in a quantized spin current conductivity $\sigma_{xy}^{s} = e/(2\pi)$. Kane and Mele introduced a coupling term between the spin up and spin down electrons to allow for spin flips that was expected to open up a gap in the whole band structure. But it was found that the edge states remained gapless and that they are protected by the Kramers degeneracy and an associated $\mathbb{Z}_2$ topological invariant that reflects the parity of the Chern number.

The $\mathbb{Z}_2$ invariant can be characterized by a Chern number associated with time-reversal polarization which is defined as $P_T = P^+ - P^-$ and can be expressed as an integral similar to the Berry curvature. Here, P^+ and P^- are the partial charge polarizations for each spin flavor. It then results in a $\mathbb{Z}_2$ integer ν that defines two distinct polarization states, one with conducting edge states and one with gapped edge states. The $\mathbb{Z}_2$ classification is similar to the first Chern number classification of the quantum charge Hall effect and can be identified as second Chern number [35, 45]. The edge states transmit electrons perfectly even when there are regions of disorder. The reflection amplitude of an electron in an edge channel is odd under time-reversal which results in dissipation less transmission at zero temperature unless time-reversal symmetry is broken.

Subsequently to the discovery of the Quantum Spin Hall effect by Kane and Mele, the term "topological insulator" (TI) was coined as a distinction from insulators with trivial topological properties. Trivial usually attributes to the fact that the wave functions of a material can be defined continuously over the whole Brillouin zone while in the Quantum Spin Hall phase wave functions have to be defined in patches within the Brillouin zone. The Quantum Spin Hall effect is the basis of topological insulators. Due to this effect, topological insulators have conducting helical edge states that are filtered by spin and resistant towards perturbations.

Chapter 3

Recent Developments

The theoretical prediction of the Quantum Spin Hall effect in Graphene set off a series of developments. After Charles Kane's and Eugene Mele's topological categorization of the Quantum Spin Hall effect by a $\mathbb{Z}_2$ invariant [43, 44], several other attempts at mathematical derivations of the invariant and characterizations of properties were made. Liang Fu and Charles Kane showed that, for non interacting electrons, the Quantum Spin Hall $\mathbb{Z}_2$ invariant can be expressed analogous to the Berry phase formulation of the charge polarization [46]. The Kramers doublet plays an important role as the relative phase between it reduces the second Chern number represented by $\mathbb{Z}$ to a $\mathbb{Z}_2$ topological invariant [47]. Moore et al. show that the time-reversal invariant Brillouin zone can be classified within homotopy theory and determine distinct classes of maps from the Brillouin zone to the space of Bloch Hamiltonians. They show that there exists one $\mathbb{Z}_2$ index per Bloch band in two dimensions and four $\mathbb{Z}_2$ indice per Bloch band in three dimensions [48]. Moreover, time-reversal invariant insulators exist in four dimensions and the 2D and 3D topological insulators can be obtained through dimensional reduction of these 4D system [49]. The edge states of 2D systems also have the important property helicity, meaning that the up spins propagate in one direction, while the down spins propagate in the other [50]. The stability of the Quantum Spin Hall state is further investigated by Xu and Moore who find that it is stable to weak interactions and disorder for models with single Kramer pairs [51].

Further investigation into topological insulators has brought to light more of their properties. Together with superconductors, different types of topological insulators and superconductors can be systemized in a periodic table [52]. This is due to the relation between the two types of structures in terms of time-reversal symmetry, particle-hole symmetry, and chiral symmetry for different spacial dimensions. Imura et al. found that weak topological insulators may also be associated with a periodic gap size [53]. Moreover, other symmetries may be used as source for the protection of edge states, for example mirror symmetry and rotational symmetries [54, 55].

Experimental Discovery of 2D and 3D Topological Insulators

The initial candidate for a 2D topological or spin hall insulator, Graphene, had to be dismissed as it was realized that the actual spin-orbit coupling in Graphene was too weak to open up a gap large enough. At the Dirac point, the gap only reaches a size of order 10^{-6} eV [56, 57]. For another proposal, independent of the work of Kane and Mele, by Bernevig and Zhang in GaAs there were no immediate experimental systems available [58]. A second proposal by Bernevig, Hughes, and Zhang claimed for the Quantum Spin Hall effect to be present in layered CdTe-HgTe-CdTe quantum wells when certain conditions for the thickness of HgTe are met [59]. Subsequently, the proposed quantum well structure was realized by Molenkamp et al. showing strong evidence for the existence of gapless edge states without the presence of a magnetic field [60]. In this model, the necessary spin-orbit coupling in the effective Hamiltonians results from the spin-orbit coupled p orbitals and the mass parameter can be tuned to reach negative values because s orbitals lie, energetically, below the p orbitals. With increasing HgTe size the mass parameter becomes smaller until it is negative and the system enters the topological regime.

After the discovery of the QSHE in HgTe/CdTe quantum wells, further proposals for $\mathrm{Bi}_{1-x}\mathrm{Sb}_x$ and strained HgTe as strong 3D topological insulators were made [61] which lead to the experimental discovery of the first 3D topological insulator in $\mathrm{Bi}_{1-x}\mathrm{Sb}_x$ by Hsieh et al. [62]. Fu and Kane also pointed out that with 3D topological insulators there is associated a set of four $\mathbb{Z}_2$ topological invariants $(\nu_0;\nu_1\nu_2\nu_3)$ that can lead to weak and strong topological insulators, where the 3D TI in $\mathrm{Bi}_{1-x}\mathrm{Sb}_x$ is classified as strong. The term weak 3D topological insulator is associated with structures that consist of layered two-dimensional topological insulators similar to how the 3D integer quantum Hall state can be constructed by layering regular 2D Quantum Hall structures [63]. Weak topological insulators have $\nu_0 = 0$ and the helical edge states of the 2D structures turn into anisotropic surface states that are not protected by time-reversal symmetry anymore.

Three-dimensional topological insulators with topological invariant $\nu_0 = 1$ are considered strong topological insulators. In a strong topological insulator the number of Kramers points enclosed by the surface Fermi circle is odd ($\nu_0 = 1$) while it is even for weak topological insulators ($\nu_0 = 0$). Because the band gap in $Bi_{1-x}Sb_x$ is small, it was desirable to find topological materials with larger band gap. Zhang et al. then showed that Bi_2Se_3, Bi_2Te_3, and Sb_2Te_3 are possible candidates of strong topological insulators [64] which was confirmed around the same time by Xia et al. [65] for Bi_2Se_3. The works of Zhang et al. in [64] serves as a foundation for this thesis. Its details will be explained more thoroughly in section 3.1.

Topological Insulators in other Physical Systems

Topological states have also been identified in other areas of physics. 3D topological insulators have been simulated in the frame of ultra cold atoms being subject to artificial gauge fields in optical lattices [66–69]. In acoustical topological insulators, edge states have been observed in acoustic resonators that are arranged in a honey comb lattice [70, 71]. Also, topologically nontrivial states of light have been created in periodic photonic structures [72, 73]. For two types of water waves on the oceans of earth around the equator, it was theorized that they are the result of topological order [74].

The discovery of topological insulators also sparked excitement in the area of quantum computation. Qubits, the binary system associated with the construction of quantum computers, tend to be unstable when created in conventional ways. With the help of the stability of topological states the existence of stable zero energy Majorana modes is expected in systems consisting of a superconductor in close proximity to a topological insulator [75–78]. These Majorana modes behave like anyons and are a candidate for fault tolerant quantum computing. There is strong evidence for the existence of Majorana modes but the observed systems yet have to be proven to be suitable for quantum computing [79, 80].

Apart from Majorana fermions, another fundamental particle predicted by the Dirac equation are Weyl fermions. Weyl semimetals are named after these types of fermions and they feature charge carriers that behave like Weyl fermions in the bulk band structure and show Fermi arcs in the surface state band structure. Weyl fermions occur at accidental touching points in the bulk band structure [81] which are related to Berry curvature monopoles in the

Brillouin zone [82, 83].

Topological Kondo insulators relate to classic Kondo insulators that adapt topological order. Robust surface states have been observed in SmB_6 which may be attributed to topological properties of the Kondo insulator [84, 85].

Magnetic Properties of Topological Insulators

Considering the prerequisite of classical topological insulators being time-reversal invariance and the fact that TRS is broken by a magnetic field, it may seem pointless at first sight to consider magnetic properties of topological insulators. However, as stated before, topologically protected states not only result from TRS but may also be the result of other symmetries. For example, due to crystalline symmetries in Bi_2Te_3, the band structure of it in a magnetic field does not show the opening of a gap [55]. There are a number of topological effects that are related to magnetic properties. Topological states can also be present in ferromagnetic materials where magnons represent the particles being transported in protected edge channels. These topological magnon insulators have been proposed [86] and experimentally observed in superconducting qubit chains and in the honeycomb ferromagnet CrI_3 [87, 88]. Topological insulators also may feature the topological magneto-electric effect which leads to magnetic fields induced by electric fields and electric fields induced by magnetic fields [89, 90]. The properties of the Berry curvature may also lead to the realization of effective magnetic monopoles [91, 92]. Negative magnetoresistance is observed in topological insulators and topological semimetals that is also related to the Berry curvature and the chiral anomaly, respectively [93, 94]. The planar Hall effect has been observed on the surface of topological insulators and is related to effects induced by the orbital magnetic moment [95, 96]. Finally, Weyl fermions may be created in materials with time-reversal symmetry and inversion symmetry by applying a magnetic field [97].

3.1 A 3D Topological Insulator in Bi_2Se_3, Bi_2Te_3, and Sb_2Te_3

The Bi_2Se_3 family of materials as topological insulators has been introduced by Chao-Xing Liu and Shou-Cheng Zhang et al. [64]. Their group derived a low-energy effective Hamiltonian of the Bi_2Se_3 crystal structure using its

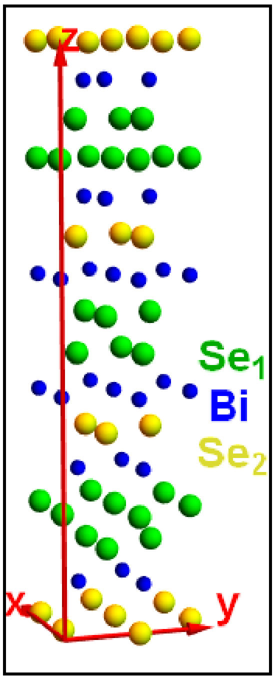

FIGURE 3.1: (Left) Crystal structure of Bi_2Se_3. Bismuth selenide consists of one selenium layer (green), which is followed by a bismuth layer, another selenium layer, and a bismuth and selenium layer where the stacking occurs along the z axis. The x and y axis lie in the plane perpendicular to the stacking direction. The crystal obeys a mirror symmetry with the mirror plane normal lying in the x-y plane and pointing in y direction. (Right, obtained from [64]) The formation of the band structure of Bi_2Se_3. Note the inversion of valence and conduction band after the application of spin-orbit coupling - these bands have opposite parity. (I) Hybridization (II) Anti-bonding/Bonding (III) Crystal-Field-Splitting (IV) Spin-Orbit-Coupling

crystal symmetries and time-reversal invariance. The Hamiltonian was justified further by a more extensive derivation using symmetry arguments and $\mathbf{k} \cdot \mathbf{p}$ -theory [98].

The crystal structure of Bi_2Se_3 is rhombohedral and in the space group D_{3d}^5. It exhibits inversion symmetry, twofold rotation along the x direction, threefold rotation along the z direction, and time-reversal symmetry. It consists of layers of bismuth and selenium that are stacked in z direction as triangle layers in the order A-B-C-A-B-C-A-$\cdots$, shown in figure 3.1. While different quintuples of Bi_2Se_3 are weakly coupled by van der Waals forces, the chemical bonding within the quintuple layer is very strong. With an electron configuration of $6s^2 6p^3$ for bismuth and $4s^2 4p^4$ for selenium, the outmost

	Parameters according to [98]			Parameters according to [99]		
	Bi_2Se_3	Bi_2Te_3	Sb_2Te_3	Bi_2Se_3	Bi_2Te_3	Sb_2Te_3
A_0 [eVÅ]	3.330	2.870	3.400	2.513	4.003	3.694
B_0 [eVÅ]	2.260	0.300	0.840	1.836	0.900	1.174
M_0 [eV]	−0.280	−0.300	−0.220	−0.169	−0.296	−0.182
M_1 [eVÅ^2]	6.860	2.790	19.640	3.353	9.258	22.136
M_2 [eVÅ^2]	44.500	57.380	48.510	29.375	177.355	51.320
C_0 [eV]	−0.008	−0.180	0.001	0.048	−0.123	0.023
C_1 [eVÅ^2]	5.740	6.550	−12.390	1.410	2.667	−14.211
C_2 [eVÅ^2]	30.400	49.680	−10.780	13.906	154.457	−6.972

TABLE 3.1: Material parameters according to [98] and [99] for all involved materials. In this thesis, the set on the right hand side [99] will be used for the most part. In some cases the left hand side parameter set [98] will be used to underline differences that occur. While the derivation of the parameters in [98] relies on the atomic orbital wave functions and on symmetry considerations and $\mathbf{k} \cdot \mathbf{p}$-theory, the parameters from [99] are derived solely on the basis of $\mathbf{k} \cdot \mathbf{p}$-theory with spinor wave functions derived with the extended linearized augmented plane wave method (ELAPW).

shells of both materials are p orbitals and, hence, the s orbitals are neglected. To obtain the four essential bands around the Fermi level, several effects on the bismuth and selenium bands are considered and labelled (I) to (IV) as indicated in figure 3.1. In the first stage (I), hybridization of bismuth orbitals and selenium orbitals leads to the repulsion of levels. Because the system is inversion invariant, these states can be combined to bonding and antibonding states with a definite parity (II). This leads to two sets of states with opposite parity around the Fermi energy. Crystal field splitting (III) leads to a splitting into $p_{x,y}$ and p_z orbitals. Due to the layered structure in z direction, the x-y plane is different from the z direction in the atomic plane. Finally, spin-orbit coupling (IV) leads to the inversion of the bands so that the band that was previously below (above) the Fermi energy with negative (positive) parity now is above (below) the Fermi level. After symmetry considerations, the resultant bands in the order $|P1_z^+, \uparrow\rangle$, $|P2_z^-, \downarrow\rangle$, $|P1_z^+, \downarrow\rangle$, $|P2_z^-, \uparrow\rangle$ lead to the model Hamiltonian

$$H_{Zhang} = \epsilon\left(k\right) + \begin{pmatrix} M(k) & B_0 k_z & 0 & A_0 k_- \\ B_0 k_z & -M(k) & A_0 k_- & 0 \\ 0 & A_0 k_+ & M(k) & -B_0 k_z \\ A_0 k_+ & 0 & -B_0 k_z & -M(k) \end{pmatrix} + \mathcal{O}\left(k^2\right) \tag{3.1}$$

where $\epsilon\left(k\right) = C_0 + C_1 k_z^2 + C_2(k_x^2 + k_y^2)$ represents particle-hole asymmetry, $M(k) = M_0 + M_1 k_z^2 + M_2(k_x^2 + k_y^2)$, and $k_\pm = k_x \pm i k_y$. For the $|P1_z^\tau, \sigma\rangle$, $|P2_z^\tau, \sigma\rangle$ basis states, σ represents the the spin eigenvalues and τ represents the parity eigenvalues which can also be interpreted as a two level pseudospin system. The parameters A_0, C_i, M_i, and B_0 are material specific to Bi_2Se_3, Bi_2Te_3, and Sb_2Te_3 and were determined numerically. In an attempt to refine these material parameter, ab initio calculations were conducted and found another set of parameters representing the respective materials. Both sets of parameters are listed in table 3.1. The model Hamiltonian (3.1) resembles Dirac's equation when written as

$$H_{Dirac} = \epsilon\left(k\right) + \left[A_0\left(k_x\alpha_x + k_y\alpha_y\right) + B_0 k_z \alpha_z + M\left(k\right)\beta\right] + \mathcal{O}\left(k^2\right) \tag{3.2}$$

with $\alpha_a = \sigma_a \otimes \tau_1$, $\beta = \mathbb{1} \otimes \tau_3$, and $a, i \in \{x, y, z\}$. σ_a and τ_i are the Pauli matrices. As such, it is also denoted as Dirac-like Hamiltonian. The Hamiltonian derived in this section serves as basis of this thesis. Results obtained here are also applicable to any other material with this type of Hamiltonian, for example the Dirac semimetal Cd_3As_2 [100, 101] or other topological insulators such as $Bi_2Te_2I_2$ [102].

Chapter 4

Confined 3D Topological Insulator with no external fields

The central consideration of this chapter is a harmonic potential extending along the z-direction of the material, the stacking direction which is used as confining potential. Usually, confinement is applied by introducing infinite hard walls, that is, by restricting the Hamiltonian to a certain space and the wave function is set to vanish outside this space. Compared to this, a downside of the soft harmonic potential that is used here would be that it introduces a force towards the center of the material. On the other hand, fundamentally, the transition crystal-boundary-vacuum is, arguably, more realistic because the forces exerted by the crystal will not end abruptly but decay smoothly on a certain length scale while exiting the crystal structure. With hard-wall confinements, by definition, there is no possibility for the description of wave functions outside the crystal. The main reason for this choice of confining potential, however, is that it is simple and that it will prove to fit in well with the rest of the model while still being a realizable experimental setting in optical lattices.

It has been proposed [66, 103] that Topological Insulators can be realized in two-dimensional hexagonal optical lattices with a light-induced periodic vector potential. Furthermore, it has been shown that an optical lattice can be used as quantum simulators of relativistic lattice fermions in 3 + 1 dimensions where the effective physical system is represented by a 3D Topological Insulator [67]. For 3D $\mathbb{Z}_2$ Topological Insulators such as Bi_2Se_3, Bi_2Te_3, and Sb_2Te_3, optical lattice simulations have been realized in optical flux lattices that generate non-abelian gauge fields such that Time-Reversal Symmetry is not broken and with non-trivial $\mathbb{Z}_2$ invariant [69, 104, 105]. Furthermore, the confining potential can modelled similarly to the harmonic potential used here and can be made arbitrarily sharp as shown in [106]. As such, the validity of the model presented here and its results may be verified under such circumstances at least qualitatively. At the same time, this model can serve as a verification of the experimental setup and it can give insights into its further properties. Topological Insulators in optical lattices, in turn, drive the development of Topological Quantum Computing [68].

4.1 Model Hamiltonian for a Confined 3D Topological Insulator

In this study, the low energy approximation (3.1) is used as basis for a soft confinement of the materials Bi_2Se_3, Bi_2Te_3, and Sb_2Te_3. A mass confined potential of the form

$$\mathcal{V}(z) = V(z)\left(\mathbb{1} \otimes \tau_z\right) = \begin{pmatrix} V(z) & 0 & 0 & 0 \\ 0 & -V(z) & 0 & 0 \\ 0 & 0 & V(z) & 0 \\ 0 & 0 & 0 & -V(z) \end{pmatrix} \tag{4.1}$$

is considered. Here, $V(z)$ takes on the form of the usual harmonic potential

$$V(z) = \frac{1}{2} m_{\|} \Omega_\gamma^2 z^2 \tag{4.2}$$

with mass $m_{\|}$ and Ω_γ defined with respect to the material parameters as

$$m_{\|} = \frac{\hbar^2}{2M_1} \quad \text{and} \quad \Omega_\gamma = \gamma \frac{A_0^2}{M_2 \hbar}. \tag{4.3}$$

The magnitude of the confinement potential is parametrised by γ. The smaller γ becomes, the wider the parabola opens up and allows for less restricted movement which is illustrated in figure 3.1. After introducing this potential, the total Hamiltonian of the system reads

$$H = \epsilon(k) + \begin{pmatrix} M(k) & B_0 k_z & 0 & A_0 k_- \\ B_0 k_z & -M(k) & A_0 k_- & 0 \\ 0 & A_0 k_+ & M(k) & -B_0 k_z \\ A_0 k_+ & 0 & -B_0 k_z & -M(k) \end{pmatrix} + \mathcal{V}(z). \tag{4.4}$$

As is, the advantage of the harmonic oscillator potential is not immediately apparent. The idea is to obtain a full harmonic oscillator Schrödinger equation and make use of its harmonic oscillator (HO) wave functions in order to solve the system. The first step towards this is to carry out the replacement $k_z \to -\mathrm{i}\partial_z$. This allows to rewrite the Hamiltonian as

$$H = \epsilon(k) + \begin{pmatrix} \mathscr{M}(k) + H_O & -\mathrm{i}B_0\partial_z & 0 & A_0 k_- \\ -\mathrm{i}B_0\partial_z & -\mathscr{M}(k) - H_O & A_0 k_- & 0 \\ 0 & A_0 k_+ & \mathscr{M}(k) + H_O & \mathrm{i}B_0\partial_z \\ A_0 k_+ & 0 & \mathrm{i}B_0\partial_z & -\mathscr{M}(k) - H_O \end{pmatrix} \tag{4.5}$$

where the effective gap parameter $\mathscr{M}(k)$ and the harmonic oscillator Hamiltonian H_O read

$$\mathscr{M}(k) = M_0 + M_2\mathbf{k}_\perp^2 \quad \text{and} \quad H_O = -\frac{\hbar^2}{2m_\parallel}\partial_z^2 + \frac{1}{2}m_\parallel\Omega_\gamma^2 z^2, \tag{4.6}$$

respectively, where $\mathbf{k}_\perp^2 = k_x^2 + k_y^2$ and $k_\pm = k_x + ik_y$. The solution to the Schrödinger equation for the harmonic oscillator Hamiltonian, $H_O\Phi(z) = \mathcal{E}\Phi(z)$, are regular harmonic oscillator functions

$$\Phi_n(z) = \frac{1}{\sqrt{2^n n!}}\left(\frac{m_\parallel\Omega_\gamma}{\pi\hbar}\right)^{1/4} \mathrm{e}^{-\frac{m_\parallel\Omega_\gamma z^2}{2\hbar}}\mathcal{H}_n\left(\sqrt{\frac{m_\parallel\Omega_\gamma}{\hbar}}z\right), \tag{4.7}$$

where $\mathcal{H}_n$ denote Hermite polynomials

$$\mathcal{H}_n(z) = (-1)^n \mathrm{e}^{z^2}\frac{\mathrm{d}^n}{\mathrm{d}z^n}\left(\mathrm{e}^{-z^2}\right) \tag{4.8}$$

and the prefactor of z is called the natural length of the harmonic oscillator or, here, the harmonic oscillator length $l_\gamma = \sqrt{\hbar/(m_\parallel\Omega_\gamma)} = \sqrt{2M_1/(E_\perp\gamma)}$. Furthermore, its energy eigenvalues are the energies of the harmonic oscillator

$$\mathcal{E}_n^0 = \hbar\Omega_\gamma\left(n + \frac{1}{2}\right). \tag{4.9}$$

It is convenient to split the Hamiltonian into a part that is solvable analytically, H_0, and two further parts, H_ϵ, which represents the particle-hole asymmetry $\epsilon_{\mathbf{k}_\perp}$, and $H_\parallel(z)$, which includes the z-dependent terms that can not be included in the harmonic oscillator Hamiltonian. It becomes apparent that

H_0 becomes block diagonal when the order of the base orbitals is changed so that $|P2_z^-, \downarrow\rangle$ and $|P2_1^-, \uparrow\rangle$ switch positions. This results in the order $\{|P1_z^+, \uparrow\rangle$, $|P2_1^-, \uparrow\rangle$, $|P1_z^+, \downarrow\rangle$, $|P2_z^-, \downarrow\rangle\}$ and H_0, H_ϵ, and $H_{\|}$ then read

$$H_0 = \begin{pmatrix} \mathcal{M}_{\mathbf{k}_\perp} & \mathcal{A}^*_{\mathbf{k}_\perp} & 0 & 0 \\ \mathcal{A}_{\mathbf{k}_\perp} & -\mathcal{M}_{\mathbf{k}_\perp} & 0 & 0 \\ 0 & 0 & \mathcal{M}_{\mathbf{k}_\perp} & \mathcal{A}_{\mathbf{k}_\perp} \\ 0 & 0 & \mathcal{A}^*_{\mathbf{k}_\perp} & -\mathcal{M}_{\mathbf{k}_\perp} \end{pmatrix}, \quad H_{\|} = -\left(\sigma_y \otimes \tau_y\right) B_0 \frac{\hat{p}_z}{\hbar}, \tag{4.10}$$

and $H_\epsilon = \epsilon_{\mathbf{k}_\perp}$, respectively, where $\hat{p}_z$ is the momentum operator in z direction, $\hat{p}_z = -i\hbar\partial_z$, and $\mathbf{k}_\perp$ is short for (k_x, k_y), i.e. $\mathcal{M}_{\mathbf{k}_\perp} = \mathcal{M}(k_x, k_y)$. The convention is taken that, in terms of the form $\sigma_i \otimes \tau_j$, σ_i is always to the left of the Kronecker matrix product $\otimes$ while τ_i is always to the right of it. H_0 is invariant under a rotation in the k_x-k_y plane. For $k_x = k' \operatorname{Cos}(\varphi)$ and $k_y = k' \operatorname{Sin}(\varphi)$, it follows

$$k_x^2 + k_y^2 = (k')^2 \text{ and } k_x \pm ik_y = k'[\operatorname{Cos}(\varphi) + i \operatorname{Sin}(\varphi)] \tag{4.11}$$

which results in the same Hamiltonian for a rotation of axes around the z axis. For later convenience, $A_0 k_\pm$ is summarized by the τ_x-τ_y term $\mathcal{A}_{\mathbf{k}_\perp} = A_0 k_\pm$. The goal is now to find an analytical solution for

$$H_0 \psi_{\mathbf{k}_\perp}(z) = \mathcal{E}_n \psi_{\mathbf{k}_\perp}(z) \tag{4.12}$$

that can be used as Ansatz for the perturbative solution to the whole Hamiltonian. Since H_0 is of the form

$$H_0 = \begin{pmatrix} h_0 & 0 \\ 0 & h_0^* \end{pmatrix}, \tag{4.13}$$

it is possible to solve the two blocks separately and split the Schrödinger equation into two parts

$$\begin{aligned} h_0\, \psi^{(\uparrow)}_{\mathbf{k}_\perp}(z) &= \mathcal{E}\, \psi^{(\uparrow)}_{\mathbf{k}_\perp}(z) \\ h_0^*\, \psi^{(\downarrow)}_{\mathbf{k}_\perp}(z) &= \mathcal{E}\, \psi^{(\downarrow)}_{\mathbf{k}_\perp}(z) \end{aligned} \tag{4.14}$$

where the asterisk represents complex conjugation. H_0 is invariant under the time-reversal operator

$$\mathcal{T} = i\sigma_y \otimes \mathbb{1}_{2\times 2}\mathcal{K}$$

and h_0 is invariant under the operation $\mathscr{T} = i\sigma_y \mathcal{K}$. Assuming that $\psi^{(\uparrow/\downarrow)}_{\mathbf{k}_\perp}(z)$ can be factorized, the Ansatz

$$\psi^{(\uparrow)}_{n\mathbf{k}_\perp}(z) = \psi^{0(\uparrow)}_{n\mathbf{k}_\perp} \Phi_n(z) \tag{4.15}$$

is used, making use of the harmonic oscillator functions $\Phi_n(z)$. With this, the effective gap parameter $\mathcal{M}$ can be expressed in terms of the HO energies as

$$\mathcal{M}_{n\,\mathbf{k}_\perp} = M_0 + M_2 \mathbf{k}_\perp^2 + \mathcal{E}_n^0 \tag{4.16}$$

and the energy eigenvalues of h_0 read

$$\mathcal{E} = \mathcal{E}^{\alpha}_{n\,\mathbf{k}_\perp} = \alpha\sqrt{(\mathcal{M}_{n\,\mathbf{k}_\perp})^2 + |\mathcal{A}_{\mathbf{k}_\perp}|^2} \tag{4.17}$$

where α can take on the values $+1$ or -1. This can be rewritten in terms of the fundamental energy and momentum measures of the system

$$E_\perp = \frac{(A_0)^2}{M_2} \quad \text{and} \quad q_0 = \frac{A_0}{M_2}. \tag{4.18}$$

Along with a definition of the coupling strength

$$\gamma_{\|} = \frac{B_0^2}{A_0^2}\frac{M_2}{2M_1}, \quad \gamma_0 = \frac{M_0}{E_\perp}, \quad \text{and} \quad \gamma_\epsilon = \frac{C_1}{2M_1}, \tag{4.19}$$

it results in

$$\mathcal{E}^{(\alpha)}_{n\,\mathbf{k}_\perp} = \alpha E_\perp \sqrt{\left[\gamma\left(n + \frac{1}{2}\right) + \gamma_0 + \left(\frac{\mathbf{k}_\perp}{q_0}\right)^2\right]^2 + \left(\frac{\mathbf{k}_\perp}{q_0}\right)^2} \tag{4.20}$$

where γ_ϵ is associated with the particle-hole asymmetry term $\epsilon_{\mathbf{k}_\perp}$. Note here, that the first term under the root, $[\mathcal{M}_{n\,\mathbf{k}_\perp}/E_\perp]^2$ determines the (un-)inverted character of the bands and further determines whether the gap is closed or not. This will be discussed further in section 4.2. The non harmonic oscillator function contributions to the eigenvectors, $\psi^{0(\uparrow)}_{n\,\mathbf{k}_\perp}$, can be written with respect to $\mathcal{E}^{(\alpha)}_{n\,\mathbf{k}_\perp}$ and $\mathcal{M}_{n\,\mathbf{k}_\perp}$ as

$$\psi^{0(\uparrow,\alpha)}_{n\,\mathbf{k}_\perp} = \begin{pmatrix} \sqrt{\frac{\mathcal{A}^*_{\mathbf{k}_\perp}}{|\mathcal{A}_{\mathbf{k}_\perp}|}\frac{\mathcal{E}^{(\alpha)}_{n\,\mathbf{k}_\perp}+\mathcal{M}_{n\,\mathbf{k}_\perp}}{2\mathcal{E}^{(\alpha)}_{n\,\mathbf{k}_\perp}}} \\ \alpha\sqrt{\frac{\mathcal{A}_{\mathbf{k}_\perp}}{|\mathcal{A}_{\mathbf{k}_\perp}|}\frac{\mathcal{E}^{(\alpha)}_{n\,\mathbf{k}_\perp}-\mathcal{M}_{n\,\mathbf{k}_\perp}}{2\mathcal{E}^{(\alpha)}_{n\,\mathbf{k}_\perp}}} \end{pmatrix}. \tag{4.21}$$

Due to the structure of the two blocks, h_0 and h_0^*, the wave functions of the two blocks are related by complex conjugation $\psi^{(\downarrow,\alpha)}_{n\,\mathbf{k}_\perp}(z) = \psi^{(\uparrow,\alpha)}_{n\,\mathbf{k}_\perp}(z)^*$. For the Hamiltonian H_0 one then gets the two solutions

$$\psi^{(+,\alpha)}_{n\,\mathbf{k}_\perp}(z) = |+\rangle \otimes \psi^{(\uparrow,\alpha)}_{n\,\mathbf{k}_\perp}(z) \quad \text{and} \quad \psi^{(-,\alpha)}_{n\,\mathbf{k}_\perp}(z) = |-\rangle \otimes \psi^{(\downarrow,\alpha)}_{n\,\mathbf{k}_\perp}(z) \tag{4.22}$$

which are simplified by the notation $\psi^{(\sigma,\alpha)}_{n\,\mathbf{k}_\perp}(z)$ where σ can take on the values $+1$ and -1 or $+$ and $-$ for convenience. $|\sigma\rangle$ represents the two spinors $(1\ 0)^T$ for $\sigma = 1$ and $(0\ 1)^T$ for $\sigma = -1$. Each state $\psi^{(\sigma,\alpha)}_{n\,\mathbf{k}_\perp}(z)$ is related to its time-reversal partner by $\mathcal{T}\psi^{(\sigma,\alpha)}_{n\,\mathbf{k}_\perp}(z) = \psi^{(-\sigma,\alpha)}_{n\,\mathbf{k}_\perp}(z)$.

The first part of the total Hamiltonian, H_0 is solved. What remains are the particle-hole asymmetry $H_{\epsilon_{\mathbf{k}_\perp}}$ and $H_\parallel$ which is called the coupling term because it couples the bands arising from the 2×2 two blocks in H_0. The Ansatz to the solution of H is made with a super position of H_0 wave functions $\psi^{(\sigma,\alpha)}_{n\,\mathbf{k}_\perp}(z)$

$$\Psi_{\mathbf{k}_\perp}(z) = \sum_{n\sigma\alpha} b^{(\sigma,\alpha)}_{n\mathbf{k}_\perp}\psi^{(\sigma,\alpha)}_{n\,\mathbf{k}_\perp}(z) \tag{4.23}$$

which leads to the Schrödinger equation

$$\Big[H_0 + H_\parallel + H_\epsilon\Big]\,\Psi_{\mathbf{k}_\perp}(z) = E\,\Psi_{\mathbf{k}_\perp}(z). \tag{4.24}$$

Each term within the square brackets will be treated separately and recombined later. The strategy in each case is to multiply a solution to H_0, $\psi^{(\tau,\beta)}_{m\,\mathbf{k}_\perp}(z)$, from the left. In bra/ket notation, starting with H_0 this results in

$$\begin{aligned} \sum_{n\sigma\alpha} b^{(\sigma,\alpha)}_{n\mathbf{k}_\perp}\langle m\tau\beta|H_0|n\sigma\alpha\rangle &= E\sum_{n\sigma\alpha}\langle m\tau\beta|n\sigma\alpha\rangle \\ b^{(\tau,\beta)}_{m\mathbf{k}_\perp}\mathcal{E}^{(\beta)}_{n\,\mathbf{k}_\perp} &= E b^{(\tau,\beta)}_{m\mathbf{k}_\perp} \end{aligned} \tag{4.25}$$

and can be rewritten as an effective Hamiltonian $\mathscr{H}_n$ with a spinor

$$b_{n\mathbf{k}_\perp} = \left(b^{(+,+)}_{0\,\mathbf{k}_\perp}, b^{(+,-)}_{0\mathbf{k}_\perp}, b^{(-,+)}_{0\,\mathbf{k}_\perp}, b^{(-,-)}_{0\,\mathbf{k}_\perp}, b^{(+,+)}_{1\,\mathbf{k}_\perp}, \dots, b^{(-,-)}_{n-1\,\mathbf{k}_\perp}\right)^T \tag{4.26}$$

and a diagonal matrix that converts H_0 energy eigenvalues to the formalism of $\mathscr{H}_n$

$$\mathscr{E}_n = \operatorname{diag}\left[\mathcal{E}^{(+)}_{n\,\mathbf{k}_\perp}, \mathcal{E}^{(-)}_{n\,\mathbf{k}_\perp}, \mathcal{E}^{(+)}_{n\,\mathbf{k}_\perp}, \mathcal{E}^{(-)}_{n\,\mathbf{k}_\perp}\right]. \tag{4.27}$$

The result is

$$\mathscr{H}_n = \begin{pmatrix} \mathscr{E}_0 & & & & & & \\ & \mathscr{E}_1 & & & & 0 & \\ & & \mathscr{E}_2 & & & & \\ & & & . & & & \\ & & & & . & & \\ & 0 & & & & . & \\ & & & & & & \mathscr{E}_{n-1} \end{pmatrix} \tag{4.28}$$

which is exact for $n \to \infty$ in

$$\mathscr{H}_n b_{n\mathbf{k}_\perp} = E b_{n\mathbf{k}_\perp} \tag{4.29}$$

and will be cut off as an approximation. Contributions by the coupling term and particle-hole asymmetry will introduce mostly off-diagonal elements to this effective Hamiltonian. Recalling $H_\parallel = -\left(\sigma_y \otimes \tau_y\right) B_0 \frac{\hat{p}_z}{\hbar}$, it is convenient to express $\hat{p}_z$ and z in terms of harmonic oscillator ladder operators

$$\frac{\hat{p}_z}{\hbar} = \mathrm{i}\sqrt{\frac{m_\parallel \Omega_\gamma}{2\hbar}}\left(a^\dagger - a\right) \quad \text{and} \quad z = \sqrt{\frac{\hbar}{2m_\parallel \Omega_\gamma}}\left(a^\dagger + a\right). \tag{4.30}$$

The contribution to $\mathscr{H}_n$ can then be expressed as

$$\begin{aligned} \sum_{n\sigma\alpha} b^{(\sigma,\alpha)}_{n\mathbf{k}_\perp} \langle m\tau\beta | H_\parallel | n\sigma\alpha\rangle &= \mathrm{i}\sqrt{\frac{m_\parallel \Omega_\gamma}{2\hbar}} B_0 \sum_{n\sigma\alpha} b^{(\sigma,\alpha)}_{n\mathbf{k}_\perp} \langle m\tau\beta | (\sigma_y \otimes \tau_y)(a - a^\dagger) | n\sigma\alpha\rangle \\ &= \mathrm{i} \sum_{n\sigma\alpha} \tau \delta_{\tau,-\sigma} b^{(\sigma,\alpha)}_{n\mathbf{k}_\perp} \tilde{C}^{nm}_{\alpha\beta\,\mathbf{k}_\perp} \langle m | a^\dagger - a | n\rangle \end{aligned} \tag{4.31}$$

with

$$\tilde{C}^{n,m}_{\alpha\beta\,\mathbf{k}_\perp} = \sqrt{\frac{\gamma\, E_\perp B_0^2}{16 M_1\, \mathcal{E}^{(\alpha)}_{n\,\mathbf{k}_\perp}\, \mathcal{E}^{(\beta)}_{m\,\mathbf{k}_\perp}}}\left[\alpha\sqrt{(\mathcal{E}^{(\beta)}_{m\,\mathbf{k}_\perp} + \mathcal{M}_{m\,\mathbf{k}_\perp})(\mathcal{E}^{(\alpha)}_{n\,\mathbf{k}_\perp} - \mathcal{M}_{n\,\mathbf{k}_\perp})}\right.$$
$$\left. - \beta\sqrt{(\mathcal{E}^{(\beta)}_{m\,\mathbf{k}_\perp} - \mathcal{M}_{m\,\mathbf{k}_\perp})(\mathcal{E}^{(\alpha)}_{n\,\mathbf{k}_\perp} + \mathcal{M}_{n\,\mathbf{k}_\perp})}\right]. \tag{4.32}$$

The evaluation of the ladder operator matrix element gives

$$\langle m|a^\dagger - a|n\rangle = \delta_{m-1,n}\sqrt{m} - \delta_{m+1,n}\sqrt{m+1}. \tag{4.33}$$

Because the relation

$$\tilde{C}^{n,m}_{\alpha\beta\,\mathbf{k}_\perp} = -\tilde{C}^{m,n}_{\beta\alpha\,\mathbf{k}_\perp} \tag{4.34}$$

holds, it is possible to rewrite (4.31) as

$$\sum_{n\sigma\alpha} b^{(\sigma,\alpha)}_{n\mathbf{k}_\perp} \langle m\tau\beta|H_\parallel|n\sigma\alpha\rangle = \mathrm{i}\sum_\alpha \tau\left[b^{(-\tau,\alpha)}_{m-1,\mathbf{k}_\perp} C^{m-1,m}_{\alpha\beta\,\mathbf{k}_\perp} + b^{(-\tau,\alpha)}_{m+1,\mathbf{k}_\perp} C^{m,m+1}_{\beta\alpha\,\mathbf{k}_\perp}\right] \tag{4.35}$$

with the definition $C^{n,m}_{\alpha\beta\,\mathbf{k}_\perp} = \sqrt{m}\,\tilde{C}^{n,m}_{\alpha\beta\,\mathbf{k}_\perp}$. In order to fit this into the same form as $\mathscr{H}_n$, the matrices Γ_n and $C_{n\,\mathbf{k}_\perp}$ are defined as

$$C_{n\,\mathbf{k}_\perp} = \begin{pmatrix} C^{n,n+1}_{++\,\mathbf{k}_\perp} & C^{n,n+1}_{+-\,\mathbf{k}_\perp} \\ C^{n,n+1}_{-+\,\mathbf{k}_\perp} & C^{n,n+1}_{--\,\mathbf{k}_\perp} \end{pmatrix} \quad \text{and} \quad \Gamma_n = \begin{pmatrix} 0 & +\mathrm{i}C_{n\,\mathbf{k}_\perp} \\ -\mathrm{i}C_{n\,\mathbf{k}_\perp} & 0 \end{pmatrix}. \tag{4.36}$$

$\mathscr{H}_n$ then takes on the form

$$\mathscr{H}_n = \begin{pmatrix} \mathscr{E}_0 & \Gamma_0 & & & & & \\ (\Gamma_0)^\dagger & \mathscr{E}_1 & \Gamma_1 & & 0 & & \\ & (\Gamma_1)^\dagger & \mathscr{E}_2 & \Gamma_2 & & & \\ & & \cdot & \cdot & \cdot & & \\ & & & \cdot & \cdot & \cdot & \\ & 0 & & & \cdot & \cdot & \cdot \\ & & & & & (\Gamma_{n-2})^\dagger & \mathscr{E}_{n-1} \end{pmatrix}. \tag{4.37}$$

In this representation, the structure of the system becomes more clear and the connotation of "coupling term" becomes apparent. For example, for $n = 2$ in $\mathscr{H}_n$, $H_\parallel$ couples the oscillator bands at $n = 0$ to the $n = 1$ bands. The larger the n, the more consecutive bands are coupled to each other as can be observed in

$$\mathscr{H}_2 = \begin{pmatrix} \mathscr{E}_0 & \Gamma_0 \\ (\Gamma_0)^\dagger & \mathscr{E}_1 \end{pmatrix}, \quad \mathscr{H}_3 = \begin{pmatrix} \mathscr{E}_0 & \Gamma_0 & 0 \\ (\Gamma_0)^\dagger & \mathscr{E}_1 & \Gamma_1 \\ 0 & (\Gamma_1)^\dagger & \mathscr{E}_2 \end{pmatrix}, \text{ etc.} \tag{4.38}$$

Finally, the particle-hole contribution to $\mathscr{H}_n$ is

$$\sum_{n\sigma\alpha} b^{(\sigma,\alpha)}_{n\mathbf{k}_\perp} \langle m\tau\beta | H_{\epsilon_{\mathbf{k}_\perp}} | n\sigma\alpha\rangle = \sum_{n\sigma\alpha} b^{(\sigma,\alpha)}_{n\mathbf{k}_\perp} \langle m\tau\beta | C_0 + C_1 \frac{\hat{p}_z^2}{\hbar^2} + C_2 \mathbf{k}_\perp^2 | n\sigma\alpha\rangle. \tag{4.39}$$

The parts with no z-dependence, $C_0 + C_2\mathbf{k}_\perp^2$, will only give an additive contribution to the diagonal entries of $\mathscr{H}_n$. The calculation for $\frac{\hat{p}_z^2}{\hbar^2}$ is very similar to the previous calculation with the main difference being the squared ladder operators which couples H_0 bands with band index n to bands with index $n \pm 2$. The other part consists of terms that involve both, raising and lowering operators and, thus, it also gives a correction term to the diagonal elements of $\mathscr{H}_n$. Specifically, one gets

$$-\frac{C_1 m_\parallel \Omega_\gamma}{2\hbar} b^{(\sigma,\alpha)}_{n\mathbf{k}_\perp} \langle m\tau\beta | (a^\dagger)^2 - 2(a^\dagger a + 1/2) + a^2 | n\sigma,\alpha\rangle \tag{4.40}$$

where the middle term, in combination with $C_0 + C_2\mathbf{k}_\perp^2$, leads to the diagonal correction

$$\mathscr{E}_n \to \mathscr{E}_n + E_\perp \left[\gamma\,\gamma_\epsilon (n + \frac{1}{2}) + \frac{C_0}{E_\perp} + \frac{C_2}{M_2}\frac{\mathbf{k}_\perp^2}{q_0^2} \right] \mathbb{1}_{4\times 4}. \tag{4.41}$$

The squared ladder operators give a contribution

$$E_\perp \sum_\alpha \left[D^{m-2,m}_{\alpha\beta,\mathbf{k}_\perp} b^{(\alpha,\tau)}_{m-2,\mathbf{k}_\perp} + D^{m,m+2}_{\beta\alpha,\mathbf{k}_\perp} b^{(\alpha,\tau)}_{m+2,\mathbf{k}_\perp} \right] \tag{4.42}$$

to the Schrödinger equation where

$$D^{n,m}_{\alpha\beta,\mathbf{k}_\perp} = -\frac{\gamma \cdot \gamma_\epsilon \sqrt{m(n+1)}}{4\sqrt{\mathcal{E}^{(\alpha)}_{n\,\mathbf{k}_\perp}\,\mathcal{E}^{(\beta)}_{m\,\mathbf{k}_\perp}}}\Bigg[\sqrt{\left(\mathcal{E}^{(\beta)}_{m\,\mathbf{k}_\perp} + \mathcal{M}_{m\,\mathbf{k}_\perp}\right)\left(\mathcal{E}^{(\alpha)}_{n\,\mathbf{k}_\perp} + \mathcal{M}_{n\,\mathbf{k}_\perp}\right)} + \alpha\beta\sqrt{\left(\mathcal{E}^{(\beta)}_{m\,\mathbf{k}_\perp} - \mathcal{M}_{m\,\mathbf{k}_\perp}\right)\left(\mathcal{E}^{(\alpha)}_{n\,\mathbf{k}_\perp} - \mathcal{M}_{n\,\mathbf{k}_\perp}\right)}\Bigg]. \tag{4.43}$$

Together along with the previous diagonal correction and the definitions

$$\Delta_n = \begin{pmatrix} D_n & 0 \\ 0 & D_n \end{pmatrix} \text{ and } D_n = \begin{pmatrix} D^n_{++} & D^n_{+-} \\ D^n_{-+} & D^n_{--} \end{pmatrix}, \tag{4.44}$$

the effective Hamiltonian $\mathscr{H}_n$ now reads

$$\mathscr{H}_n = \begin{pmatrix} \mathscr{E}_0 & \Gamma_0 & \Delta_0 & & & & \\ (\Gamma_0)^\dagger & \mathscr{E}_1 & \Gamma_1 & \Delta_1 & & 0 & \\ (\Delta_0)^\dagger & (\Gamma_1)^\dagger & \mathscr{E}_2 & \Gamma_2 & \Delta_2 & & \\ & \cdot & \cdot & \cdot & \cdot & \cdot & \\ & & \cdot & \cdot & \cdot & \cdot & \Delta_{n-3} \\ & 0 & & \cdot & \cdot & \cdot & \Gamma_{n-2} \\ & & & & (\Delta_{n-3})^\dagger & (\Gamma_{n-2})^\dagger & \mathscr{E}_{n-1} \end{pmatrix}. \tag{4.45}$$

Since Δ_n is real, the hermitian conjugation for it in $\mathscr{H}_n$ can be replaced by a regular transposition. But it is kept for the sake of clarity and aesthetics.

4.2 Properties of the System H_0

Before the simulation and discussion of the full model, it is instructive to take a closer look at the part of the model that is analytically solvable. It gives insight into the fundamentals of the system and an understanding of its characteristics. Therefore, the mathematical expressions derived in section 4.1 will be visualized using the program *Mathematica* in the version *11.2* which can be acquired from the Wolfram Research Company (http://www.wolfram.com/). The program will also be used for later numerical calculations and the code involved is accessible online [107].

A central part in the picture of the topological insulator is the harmonic potential used to confine the system. One question that arises naturally is: *how does one determine the exact size of the TI when the harmonic potential does not deliver a clear boundary to the system?* The answer is that the size of the material can only be approximated. One can obtain a first idea of the size by considering the harmonic oscillator length $l_\gamma = \sqrt{2M_1/(E_\perp \gamma)}$. This quantity will be used when comparing the different sizes for the three TI-materials.

As one of the most fundamental properties of any system, the energy eigenvalues of the H_0 model are a good starting point for the investigation. The basic structure of the dispersion in (4.20) follows a square rooted quartic behavior that forms a parabola shape or a square rooted quartic behavior that forms a W-shape (or M-shape). Both types of bands are visualized in figure 4.1. Essential for distinguishing between these two types of behavior is the gap parameter

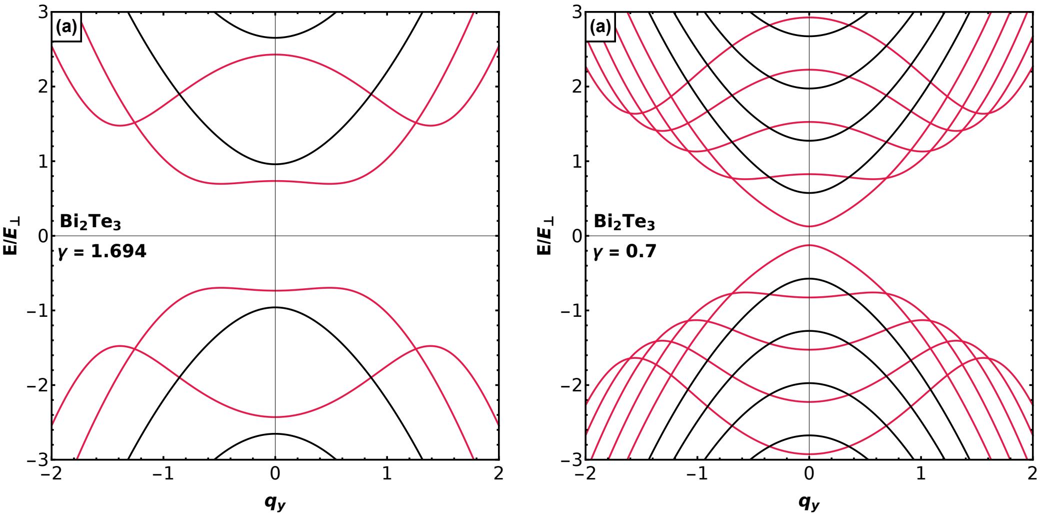

FIGURE 4.1: Band structure of H_0 for Bi_2Te_3: a) for an arbitrary $\gamma = 1.694$ which attributes to a width of 1 nm and b) for a smaller $\gamma = 0.7$ (wider TI) with a width of 1.71 nm. The red (black) bands denote (un-) inverted bands. The larger the width of the material, the more bands are inverted.

$$\mathcal{M}_{n\,\mathbf{q}_\perp} = E_\perp \left[\gamma \left(n + \frac{1}{2} \right) + \gamma_0 + \mathbf{q}_\perp^2 \right] \tag{4.46}$$

with the definition of $\mathbf{q}_\perp = \mathbf{k}_\perp / q_0$ and, more specifically, the interplay between oscillator energies

$$E_\perp \gamma \, (n + 1/2) \quad \text{and the material parameter} \quad M_0, \tag{4.47}$$

which is negative in all three materials. One interpretation of this behavior could be that the harmonic confinement competes with the material parameter M_0 which, in turn, is also a measure for the inverted character of a band. This means that, in this picture, inverted bands can be distinguished from uninverted bands by their W-shape in most of the cases. A precise definition can be extracted from (4.46) at $\mathbf{q}_\perp = 0$. A band with quantum number n is inverted if the gap parameter satisfies (note that $\gamma_0 < 0$)

$$\mathcal{M}_{n\,\mathbf{q}_\perp=0} = E_\perp \left[\gamma \left(n + \frac{1}{2} \right) + \gamma_0 \right] < 0. \tag{4.48}$$

The band character is therefore (i) dependent on the parameter γ, which is a measure for the strength and thus for the thickness of the material (where thickness grows with $1/\sqrt{\gamma}$), and (ii) dependent on the harmonic oscillator band index n. Hence, the thinner the material gets, the less likely a band is of inverted character and the larger the band index becomes, the less likely a band is of inverted character. To put it another way, as the γ parameter is getting smaller (material gets thicker), more and more bands become inverted as can be observed when comparing the H_0 band structure for Bi_2Te_3 in figure 4.1a and figure 4.1b.

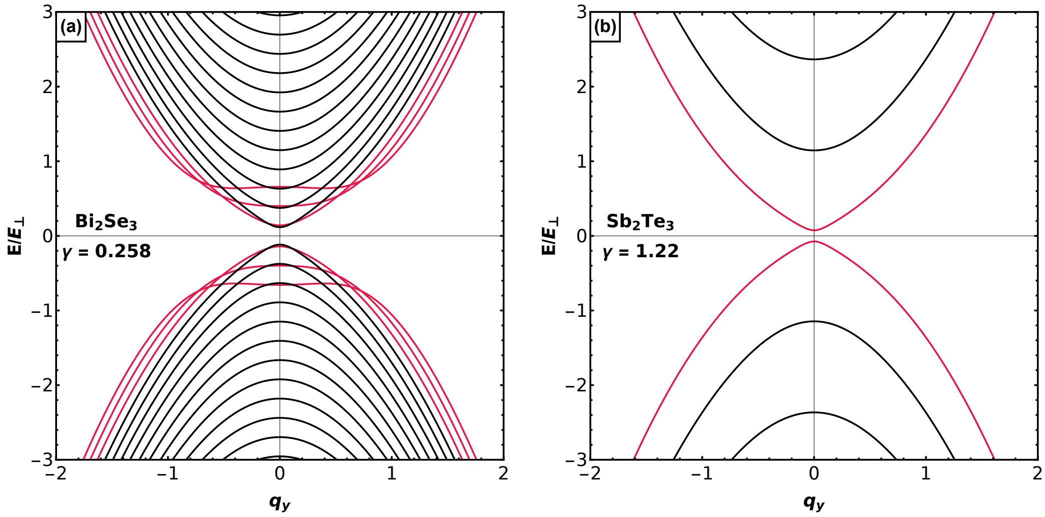

FIGURE 4.2: a) Energy dispersion of H_0 for Bi_2Se_3 at $\gamma = 0.258$. b) Band structure of H_0 for Sb_2Te_3 at $\gamma = 1.22$ (wider TI). Red (black) bands denote (un-)inverted bands and the respective values for γ correspond to a width of roughly 1 nm for both materials. Even though the width are similar, the shape of the band structures varies significantly.

Considering the band structure of the three material types, Bi_2Se_3, Bi_2Te_3, and Sb_2Te_3, even though the thickness of each respective topological insulator in figure 4.1b, figure 4.2a, and figure 4.2b is roughly equal at 1 nm, there still is a considerable difference in their band structure. While, for example, Bi_2Te_3 features several inverted bands, Sb_2Te_3 only has one inverted band. And while the characteristic energy $E_\perp$ for the aforementioned materials is similar, it is considerably smaller for Bi_2Se_3.

It is also noticeable that for Sb_2Te_3 in figure 4.2b the gap is nearly closed. For a random choice of γ and band index n this is coincidental but there are also situations when the gap is completely closed. They occur when the effective gap parameter at $\mathbf{q}_\perp = 0$ equals zero, so when the confinement energy of the harmonic oscillator exactly cancels the material parameter M_0 and thus when the condition

$$\gamma\left(n_c + \frac{1}{2}\right) + \gamma_0 = 0 \tag{4.49}$$

holds. To put it differently, the gap closes when an uninverted band turns inverted or vice versa. On one hand, this determines a critical n_c at any given width γ for which all bands with band number $n < n_c$ are inverted. On the other hand, it means that for any $n_c \geq 0$, there is a suitable material thickness, γ_c, so that the gap is closed.

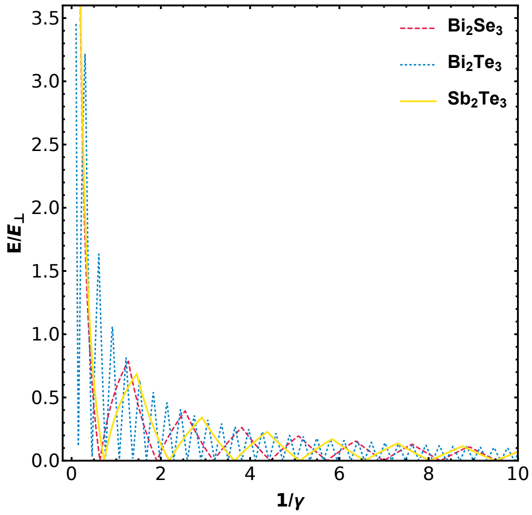

FIGURE 4.3: Periodicity of the gap closure in H_0. Pictured are Bi_2Te_3 (dotted), Bi_2Se_3 (dashed), and Sb_2Te_3 (thick). The gap opens and closes as the strength of the harmonic potential changes.

Another consequence is that the gap opens and closes periodically when the size of the material is increased or decreased. The periodic behavior can be summarized in the definition of the gap size Δ as

$$\Delta(\gamma) = 2\,\mathrm{Min}_n\left[\gamma\left(n + \frac{1}{2}\right) + \gamma_0\right] \tag{4.50}$$

where $\mathrm{Min}_n[f(n)]$ is defined as the minimum of f with respect to n (i.e. $\mathrm{Min}_n[n] = 0$ for $n \in \mathbb{N}$). The periodicity is not directly evident but when plotted it becomes clearer, as shown for all three materials in figure 4.3a. In this picture, the periodic gap closure that occurs with the change in size of the material can be explained by the interplay of confinement and inversion of bands. The curve enclosing the periodic behavior is dampened with increase in $1/\gamma$ because the energetic distance between the harmonic oscillator bands at $\mathbf{q}_\perp = 0$ decreases as γ increases. The period of the closure depends on the characteristic energy of the system $E_\perp$ and M_0 and is a constant, $\delta(1/\gamma_c) = -E_\perp/M_0$.

Another interesting point is the probability distribution in z direction of electrons that inhabit the H_0 bands. In the H_0 picture the main contribution results from the harmonic oscillator wave functions $\Phi_n(z)$. This is reasonable, considering the mathematical shape of the wave function is

$$\psi^{0(\alpha)}_{n\,\mathbf{q}_\perp}(z) = \begin{pmatrix} \sqrt{\frac{\mathcal{A}^*_{\mathbf{q}_\perp}}{|\mathcal{A}_{\mathbf{q}_\perp}|}\frac{\mathcal{E}^{(\alpha)}_{n\,\mathbf{q}_\perp}+\mathcal{M}_{n\,\mathbf{q}_\perp}}{2\mathcal{E}^{(\alpha)}_{n\,\mathbf{q}_\perp}}} \\ \alpha\sqrt{\frac{\mathcal{A}_{\mathbf{q}_\perp}}{|\mathcal{A}_{\mathbf{q}_\perp}|}\frac{\mathcal{E}^{(\alpha)}_{n\,\mathbf{q}_\perp}-\mathcal{M}_{n\,\mathbf{q}_\perp}}{2\mathcal{E}^{(\alpha)}_{n\,\mathbf{q}_\perp}}} \end{pmatrix} \Phi_n(z) \tag{4.51}$$

which reduces to the harmonic oscillator wave function density when taking the squared absolute value

$$\left|\psi^{0(\alpha)}_{n\,\mathbf{q}_\perp}(z)\right|^2 = |\Phi_n(z)|^2 \tag{4.52}$$

because it needs to be normalized. Thus, in the H_0 picture, the wave functions behave like HO wave functions and are considered bulk-like.

In order to get a better understanding of band inversion, the spin and pseudospin character of the bands can be studied. With respect to the present choice of basis state order, the pseudospin operator and the spin operator

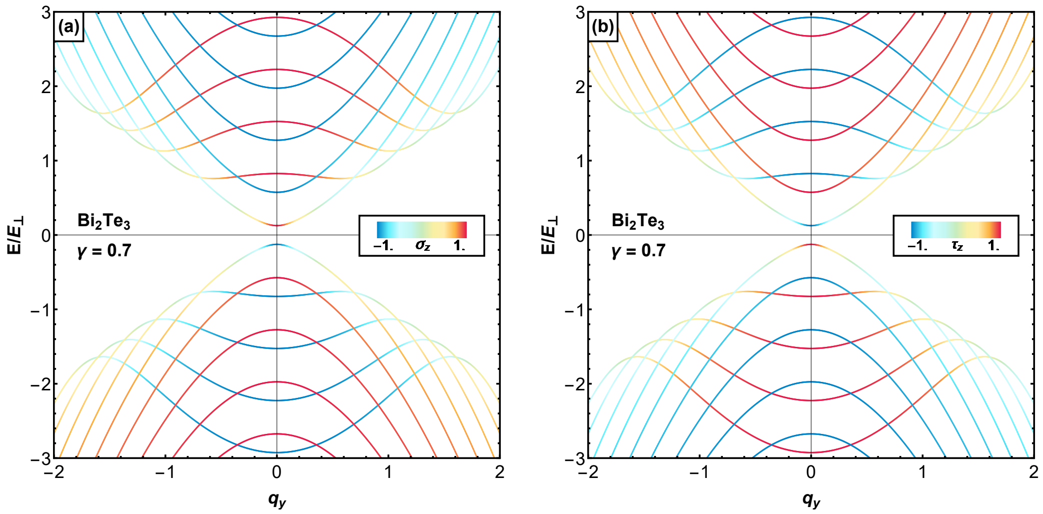

FIGURE 4.4: a) $\hat{S}_z$ expectation values of Bi_2Te_3 at $\gamma = 0.7$. All bands are doubly degenerate with opposite spin projection expectation values. b) The pseudospin projection expectation values are inverted with respect to the spin projection expectation values. All bands are doubly degenerate with negated pseudospin projection expectation values for the bands not pictured.

projected along z direction take on the forms

$$\hat{S}_z = \sigma_z \otimes \tau_z \quad \text{and} \quad \hat{T}_z = \mathbb{1}_{2\times 2} \otimes \tau_z, \tag{4.53}$$

respectively. The spin and pseudospin projection expectation values are then determined by

$$\langle \psi^{(\sigma,\alpha)}_{n\,\mathbf{q}_\perp} | \hat{S}_z | \psi^{(\sigma,\alpha)}_{n\,\mathbf{q}_\perp} \rangle \quad \text{and} \quad \langle \psi^{(\sigma,\alpha)}_{n\,\mathbf{q}_\perp} | \hat{T}_z | \psi^{(\sigma,\alpha)}_{n\,\mathbf{q}_\perp} \rangle, \tag{4.54}$$

respectively, where the involved integrals over the harmonic oscillator wave functions contributes a factor of one because they are not affected by non-z-dependent operators. The previous determination of the bands' inverted character by considering the zero points of Δ_γ can now be investigated more thoroughly by using the pseudospin projection expectation value distribution within a band as the previous method only took into account the result of the gap parameter at $\mathbf{q}_\perp = 0$. This method still reproduces the same behavior around $\mathbf{q}_\perp = 0$, but also visibly deviates and parts of the inverted bands' pseudospin expectation values become nearly neutral as can be seen in figure 4.4a.

Regarding spin projection expectation value texture, when the sets of quantum numbers $\{n, \alpha\}$ are equivalent, the expectation values for the wave functions with $\sigma = 1$ and $\sigma = -1$ are the same. For the pseudospin projection expectation values, bands with quantum numbers $\sigma = 1$ and $\sigma = -1$ take opposite expectation values, so $\langle \psi_{n\,\mathbf{q}_\perp}^{(+,\alpha)} | \hat{T}_z | \psi_{n\,\mathbf{q}_\perp}^{(+,\alpha)} \rangle = -\langle \psi_{n\,\mathbf{q}_\perp}^{(-,\alpha)} | \hat{T}_z | \psi_{n\,\mathbf{q}_\perp}^{(-,\alpha)} \rangle$ (figure 4.4b).

One can take away from these observations, first, that band inversion is reflected in the pseudospin z projection expectation values. Secondly, the bands involved show bulk like behavior and extend throughout the material in confinement direction. Thirdly, the periodicity of the gap is a direct consequence of the process of confinement because Ω_γ, which measures the energetic distance between two H_0 bands, becomes large as the material size decreases.

4.3 Properties of the Coupled System $H_0 + H_\parallel$

The full Hamiltonian $\mathscr{H}_n$ that does not include particle-hole asymmetry is given in (4.37) and, in general, looks like each set of four bands ($\mathscr{E}_n$) is coupled to its neighbours via the coupling terms Γ_n and Γ_{n-1}. Any attempt to get an appropriate analytically deducible approximation to the full Hamiltonian by only focusing on the low energy bands around the Fermi level or by applying for example Löwdin partitioning, also known as Schrieffer-Wolff or Foldy-Wouthuysen transformation [108], has failed or delivered very poor results. The most effective method is to cut off the Hamiltonian at a certain n that lies well beyond the critical n_c in the H_0 picture. Note here, that the energy dispersions of the H_0 picture are located on the diagonal of the full Hamiltonian $\mathscr{H}_n$. The n beyond which the approximation becomes accurate is determined by observing the change of band energies and eigenvectors with increasing n. As pointed out before, the simulation of the full Hamiltonian is carried out with the help of *Mathematica*. When the order of relative change between the energy eigenvalues of two Hamiltonians with consecutive n and $n+1$ is below 10^{-14}, which is roughly the standard precision for numerical *Mathematica* calculations, the approximation is deemed sufficiently accurate. However, the fact that n_c determines the magnitude of a sufficient n also means that the more inverted bands there are, the larger the dimensions of $\mathscr{H}_n$ have to be. Thus, the thicker the material gets, the harder it

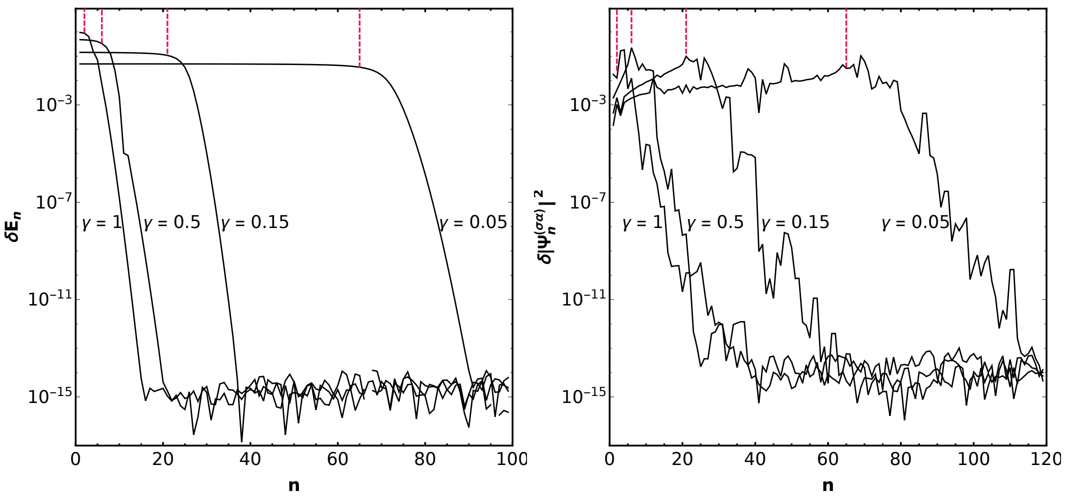

FIGURE 4.5: a) Convergence of band structure energy with increase in dimension of the total Hamiltonian $\mathscr{H}_n$. The dashed lines show the location of n_c. Convergence only occurs after all inverted H_0 bands with $n < n_c$ are included in the simulation. b) Convergence of $\mathscr{H}_n$ eigenvectors. Generally, the eigenvectors converge more slowly and their imaginary argument is subject to the *Mathematica* matrix solving algorithm and not a fixed value for different n.

is to receive satisfying results as can be seen in figure 4.5a for several material widths in Bi_2Te_3. As a result, the minimum in γ to get acceptable calculation timings is roughly $\gamma = 0.05$ where the dimension of the involved matrices exceeds $n = 100$. This attributes to $l_\gamma \sim \{25\ \text{Å}, 64\ \text{Å}, 58\ \text{Å}\}$ for the three materials Bi_2Se_3, Bi_2Te_3, and Sb_2Te_3, respectively. All of the following calculations are carried out for an approximated $\mathscr{H} = \mathscr{H}_{40}$ where $n = 40$ is large enough to obtain results with acceptable accuracy.

4.3.1 General Features of the $\mathscr{H}$ Band Structure

The change occurring in the band structure due to the band coupling between the H_0 bands fundamentally depends on the strength of the coupling parameter $\gamma_{\|}$, defined in (4.19). In Bi_2Se_3, the coupling parameter is comparably large and the structure of crossing bands in H_0 is mostly gone as can be observed in figure 4.6. On the other hand, when considering Bi_2Te_3 or Sb_2Te_3, $\gamma_{\|}$ is rather small and the remnants of the occurring anti-crossings are visible in the resultant band structure. In all cases q_x and q_y are still equivalent in the Hamiltonian and thus interchangeable. One main feature of the

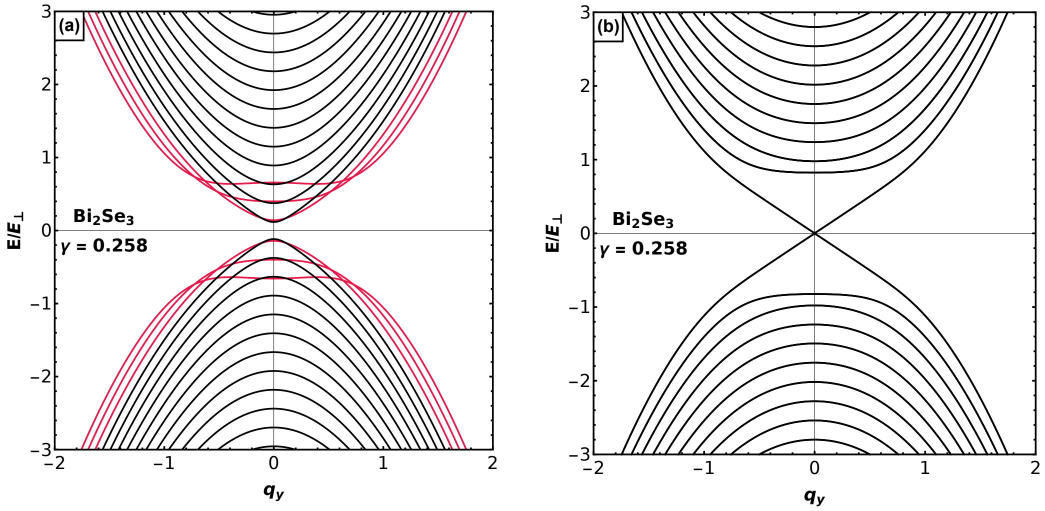

FIGURE 4.6: a) H_0 band structure of Bi_2Se_3 at $\gamma = 0.258$ and b) the band structure for the full Hamiltonian $\mathscr{H}$ at the same γ. The band coupling pushes the lowest band towards zero energy so that the Dirac cone is established even though the gap in the H_0 picture is quite significant.

band structure for all materials is the formation of the Dirac cone which, however, is only formed when the material is wide enough and confinement effects do not dominate. When γ becomes large and the confinement potential too steep, the ground state oscillator energy $\hbar\Omega_\gamma/2$ becomes large and no band in the H_0 picture is inverted anymore. Hence, when confinement effects dominate, the interplay between inverted and uninverted bands cannot lead to the formation of the Dirac cone. For Bi_2Se_3, the Dirac cone can be recognized/dissolves at around $\gamma = 0.65$. In contrast to the band structure for H_0, this Dirac cone stays in place not just for certain special values of γ but for all $\gamma < 0.65$. For the other two materials, the convergence towards a Dirac cone is faster and occurs at around $\gamma = 1.3$ (Bi_2Te_3) and $\gamma = 1.4$ (Sb_2Te_3). However, the cone for these two materials is less stable in the sense that the gap opens and closes again slightly as the material gets thicker and γ reaches lower values. Still, compared to the H_0 picture, the Dirac cones come into place for a larger range of γ. When comparing a H_0 band structure side by side to the corresponding band structure in the full $\mathscr{H}$ picture, anti-crossings that happen due to the band coupling become apparent in Bi_2Te_3 (figure 4.7a). Basically, bands with even (odd) harmonic oscillator quantum numbers that cross other even (odd) harmonic oscillator bands remain crossings. Other crossings where odd bands meet even bands turn into anti-crossings. This is the basic

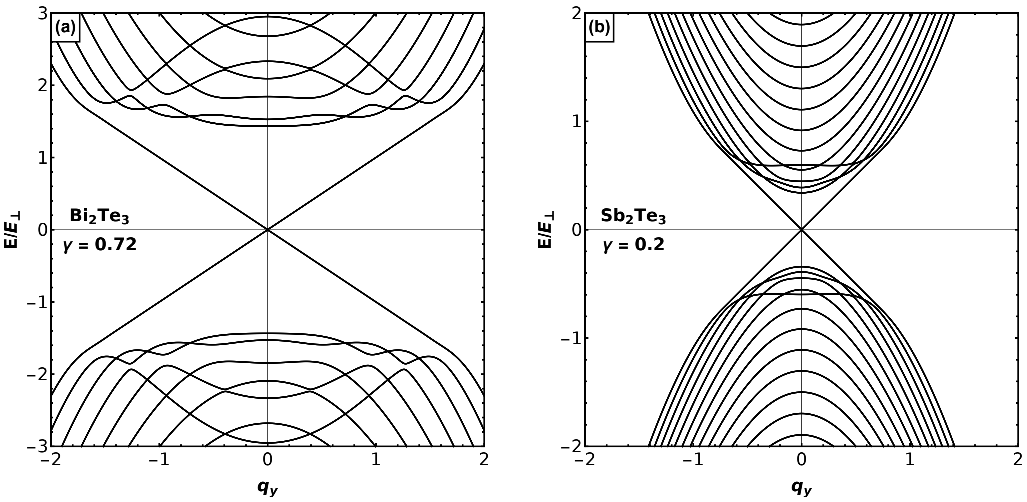

FIGURE 4.7: For Bi_2Te_3 (a) and Sb_2Te_3 (b) the lowest band also forms the Dirac cone due to the coupling of bands. Contrary to Bi_2Se_3, the structures of the bulk bands allow for band crossings and they resemble their respective structure in the H_0 picture.

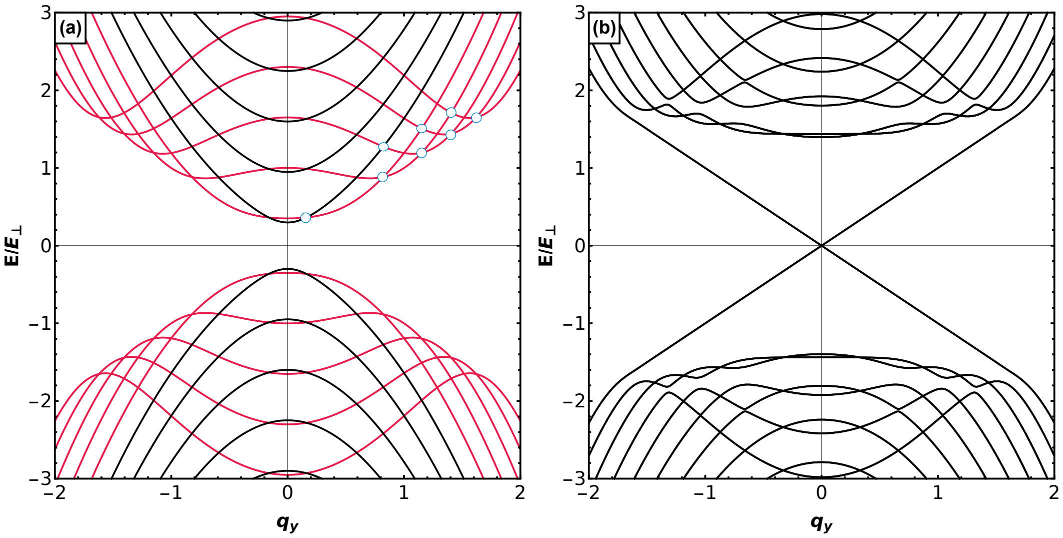

FIGURE 4.8: Establishment of Dirac Cone and band twisting from H_0 (a) to $\mathscr{H}$ (b) in Bi_2Te_3. The crossings indicated by the blue circles in a) turn into anti-crossings and lead to the formation of the Dirac cone. They also lead to a twisting effect between the two bands closest to the Dirac bands.

mechanism of how the Dirac cone is established visually in the $\mathscr{H}$ picture. It also leads to some interesting band formations. Comparing specifically the band structures of Bi_2Te_3 in the H_0 picture with structures in the $\mathscr{H}$ picture (figure 4.8) shows that some bands, as a result of this effect, establish a structure where they appear to be twisted around each other. For Sb_2Te_3, on the other hand, the interaction seems to have less impact on the band structure. Most crossings remain crossings and there is no specific structure verifiable. Out of the three materials, Sb_2Te_3 resembles its band structure in the H_0 picture the most. This is reasonable, considering its coupling strength of $\gamma_{\|} = 0.12$ which is small compared to Bi_2Te_3 ($\gamma_{\|} = 0.48$). Both of these materials, in turn, have small coupling strength compared to Bi_2Se_3 ($\gamma_{\|} = 2.34$) which shows no remnants in its band structure that can be identified as the result of band anti-crossings.

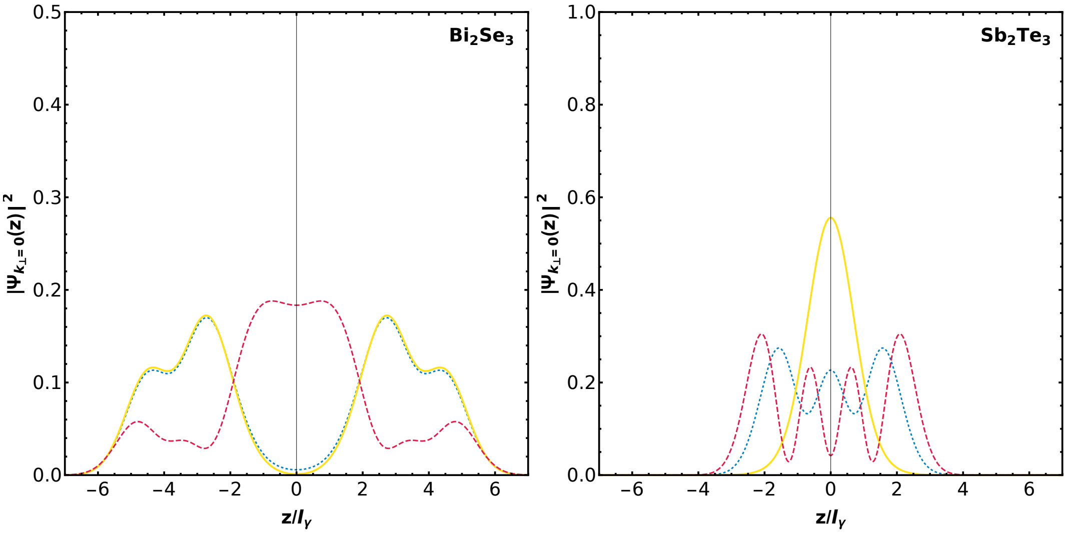

FIGURE 4.9: Dirac wave functions for Bi_2Se_3 and Sb_2Te_3 for $\gamma = 0.1$ and $\gamma = 0.15$, respectively. While the location of the Dirac wave functions tends to the surface with little probability in the center for Bi_2Se_3, the same cannot be said for Sb_2Te_3.

One key feature of topological insulators are the ungapped states that are located on the surface which was not the case for the previous harmonic oscillator wave functions. Contrary to the unperturbed system, in the current picture, there are now states for which the wave function densities are distributed around two peaks on the z axis. The probability of finding an electron in between these two peaks is non-zero when the material is very thin and on the verge of being confinement dominated, but it tends to zero as the material width increases. This applies to each of the three materials and is visualized in figure 4.9 and 4.10. However, for Bi_2Se_3 this decrease is non-periodic while for the other two materials the decline is periodic. The

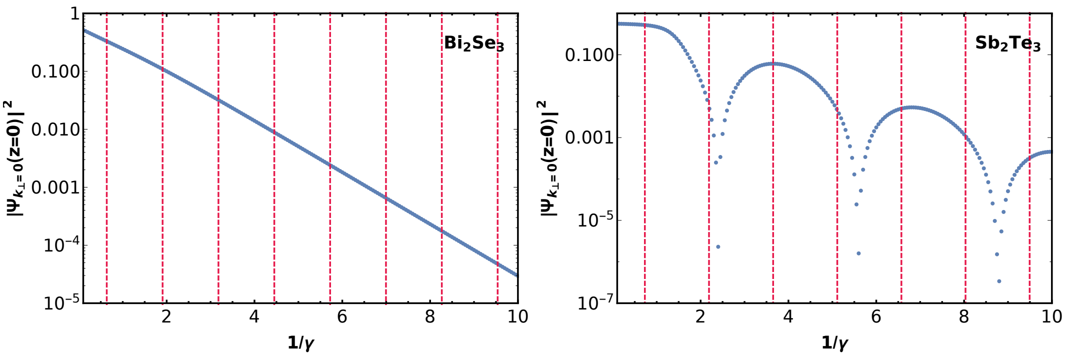

FIGURE 4.10: The Dirac wave function densities at $z = 0$ tend to zero with increase in size for both materials. However, for Sb_2Te_3, the density shows periodic behavior in $1/\gamma$. The dashed red lines denote the position ob the gap closures in the H_0 picture.

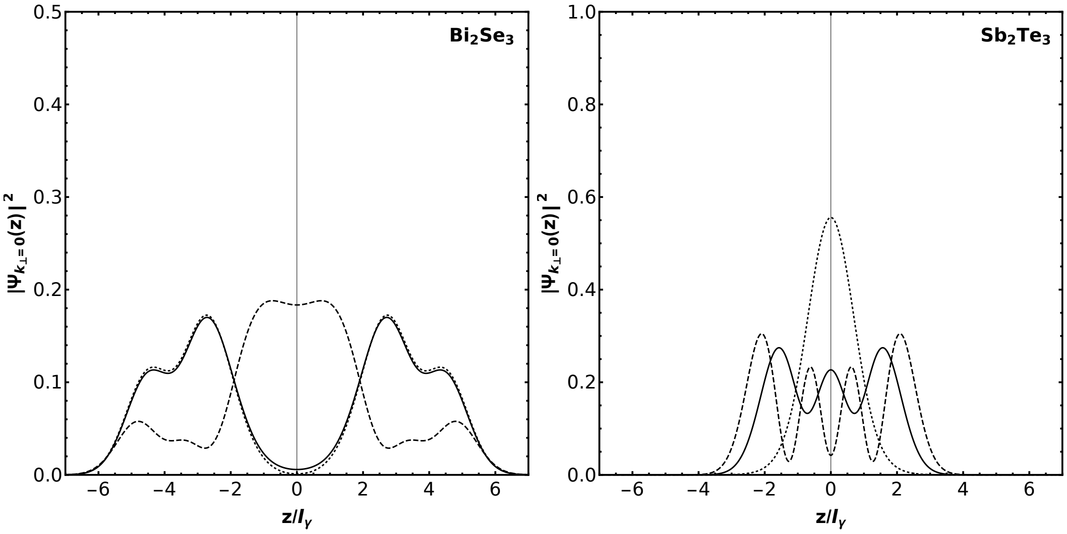

FIGURE 4.11: The three energy bands above the Fermi energy that are energetically closest to the Dirac band show clear bulk-like behavior for Sb_2Te_3 and semi-Dirac behavior for the two bands closest to the Bi_2Se_3 Dirac cone. As the distance to the Dirac cone in terms of energy increases, the Bi_2Se_3 bands become more bulk-like, too. The dotted blue lines depict the wave function densities of the energy band that are, energy wise, closest to the Dirac band. The thick yellow lines represent the second closest bands to the Dirac band and the dashed red lines show the bands third closest to the Dirac band.

periodicity may be explained by the same properties that lead to the periodic gap in the H_0 picture.

As for the bulk bands, most of them are very similar to the harmonic oscillator wave functions from before, meaning that they are mostly distributed throughout the material but their probability distributions are deformed. This behavior is illustrated in figure 4.11 for Bi_2Se_3 and Sb_2Te_3 where the deformation is stronger in the former material. One can define a condition to determine the edge of a material in positive and negative z direction in the following way. The smallest (largest) z_e for which $\left|\psi_{\mathbf{q}_\perp}(z)\right|^2 < 10^{-5}$ for all $z > z_e$ ($z < z_e$) defines the edge of the material. For all bands observed, it is possible to find such a pair of $\pm z_e$ which makes it feasible to assign a size to the respective material. Because the Dirac bands are located around the supposed edge of the material, $\pm z_e$, it may be concluded that the Dirac states are located on the surfaces of the materials whereas the bulk bands are spread throughout the material. The value $2\,z_e(\gamma)\,l_\gamma$ may then be used as a measure for the width of the materials.

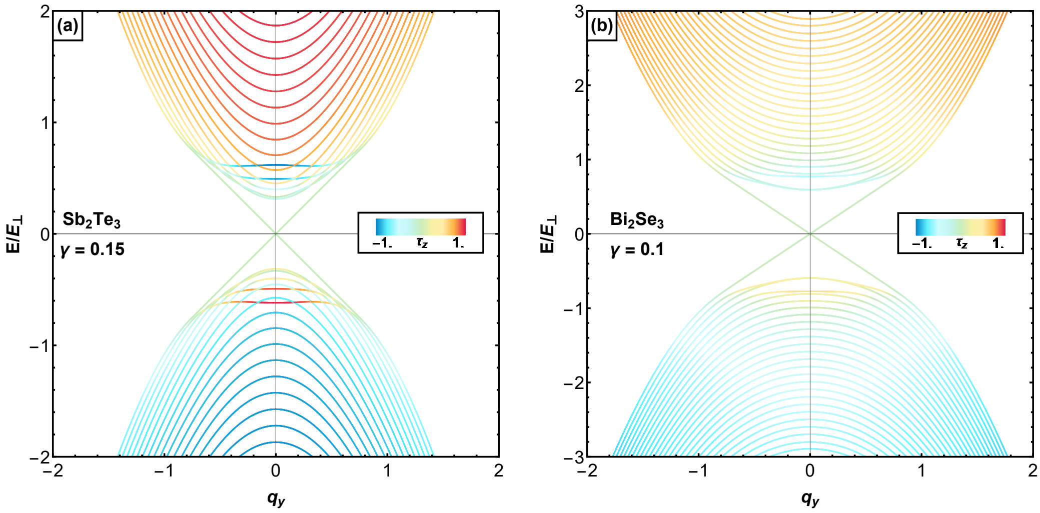

FIGURE 4.12: Pseudospin projection expectation value distribution for a) Sb_2Te_3 and b) Bi_2Se_3 at $\gamma = 0.15$ and $\gamma = 0.1$, respectively. While the inverted character of bands is very clear in Sb_2Te_3, it is less clear for Bi_2Se_3. For both materials, the Dirac cone is neutral in $\hat{T}_z$ expectation values.

There are some bands, however, whose density distributions are very similar to the distributions of the Dirac bands. They show large peaks at the edges and have only minor appearances in the bulk. These are the states that are, energy wise, closest to the Dirac bands and the effect decreases, the further away the specific band is from the Dirac cone. The bands closest to the Dirac cone are also the states that form an additional degeneracy which will be addressed in section 4.3.3.

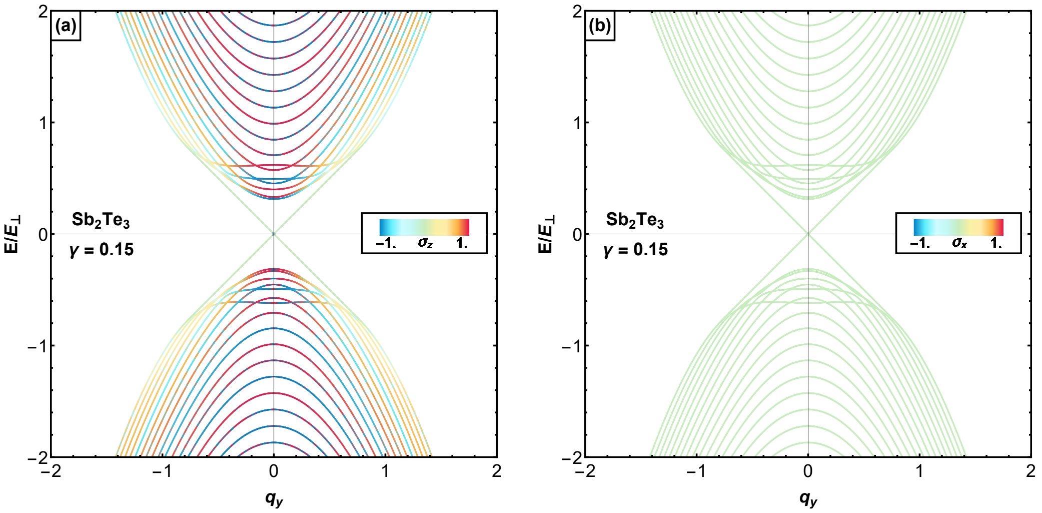

FIGURE 4.13: Spin projection expectation value distribution a) in $\hat{S}_z$ projection and b) in $\hat{S}_x$ projection for Sb_2Te_3. While values for $\hat{S}_z$ in the Dirac cone equal ± 1 at $\mathbf{q} = 0$, the rest of it is spin neutral. Bulk bands are spin up in their z projection expectation values with their respective degeneracy partner being spin down. The $\hat{S}_x$ expectation values are zero for all bands in all materials.

As for the spin and pseudospin projection expectation value distributions, Dirac cones are expected to be pseudospin neutral and the bulk bands shall reflect the inverted character of the bands involved. Both expectations are satisfied in all the materials for the pseudospin projection in z direction, $\hat{T}_z$, as long as they are not too thin. When the materials get too thin, there are no inverted bands at all. The general structure of the inversion, however, strongly depends on the specific material. For example, while H_0 bands in Bi_2Te_3 and Sb_2Se_3 can be retraced, the band coupling in Bi_2Se_3 is too strong and only a vague idea of the previous H_0 structure can be identified. Examples of these behaviors for Sb_2Se_3 and Bi_2Se_3 are shown in figure 4.12. Considering the pseudospin expectation values in x and y projection does not deliver much further insight into the system, as both, the expectation values of $\hat{T}_x$ and of $\hat{T}_y$, equal zero in all bands. The same occurs for the expectation values of the real spin operator projections, $\hat{S}_x$ and $\hat{S}_y$, as can be seen in figure 4.13b. The expectation values of the spin projection along the z axis are non-zero in all bands except for the Dirac cone and regions close to it, where it tends to zero. Note that each band is doubly degenerate with one degeneracy instance taking on a positive spin expectation value while the other one takes on the opposite value, i.e. $\langle \hat{S}_z \rangle = \pm c_0$, where c_0 is an arbitrary value between 0 and 1.

4.3.2 Gap Behavior

As mentioned in the previous section, in all three materials the gap of the surface states tends towards zero exponentially with increasing material size, even in situations where the gap size is of order $E_\perp$ in the unperturbed picture. However, the gap size at any given specific width parameter γ is subject to change and the specific gap behavior depends on the model parameters of the different materials (A_0, M_0, etc.). For Bi_2Te_3 and Sb_2Te_3 with compara-

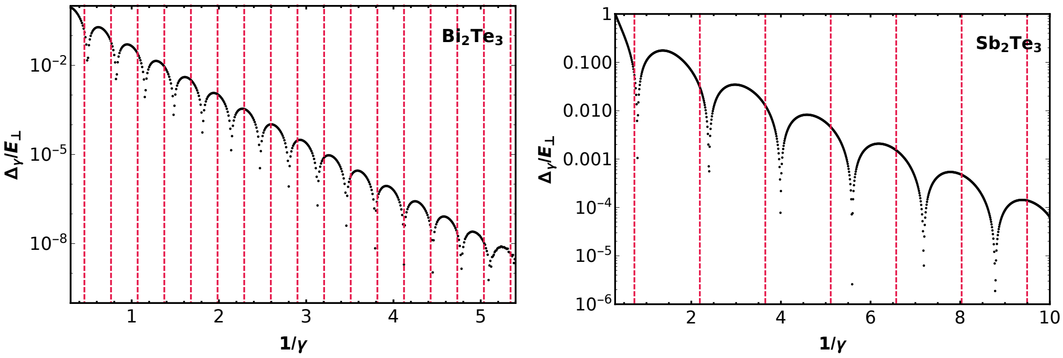

FIGURE 4.14: Band gap Δ_γ for Bi_2Te_3 and Sb_2Te_3. The dashed red lines depict the gap closures in the H_0 picture. For both materials the oscillation remains but with a slightly increased period of oscillation.

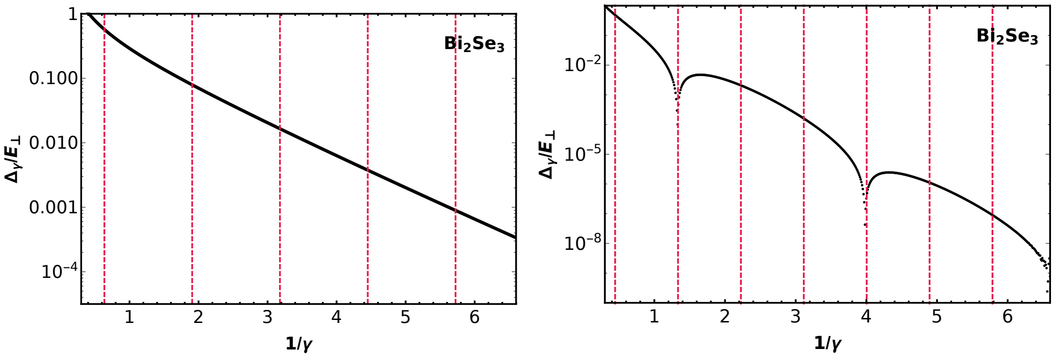

FIGURE 4.15: Band gap Δ_γ for Bi_2Se_3 assuming different sets of parameters [99] (left) and [98] (right). While one set leads to gap oscillations like in the other materials, the other set leads to a smooth exponential decay of the gap.

bly small coupling parameter $\gamma_\parallel$, the gap still exhibits a periodic behavior with varying size of material. However, the dampening that also occurs in the H_0 picture is enhanced significantly by the coupling of bands so that the gap size converges to zero much more rapidly. Furthermore, just like in the wave function oscillations at $\mathbf{q} = 0$ and $z = 0$ for varying γ from figure 4.10, the period of the oscillations is not in agreement with the H_0 oscillations anymore and the deviation from the H_0 oscillations depends on the strength of the band coupling parameter $\gamma_\parallel$. Thus, the gap behavior of Sb_2Te_3 in the full model resembles its behavior in the H_0 model more than for Bi_2Te_3 and the period of gap oscillations in these two materials is consistent with $\delta(1/\gamma_c) \sim 1/\gamma_{M_0}$, the period of the H_0 system oscillations, which corresponds to a period $\delta l_\gamma \sim \sqrt{M_1/M_0}$ for oscillation of the gap as a function of the effective 2D-system width scale l_γ. In contrast, the gap for Bi_2Se_3 doesn't show any periodic behavior and converges smoothly towards zero. The observed absence of gap oscillations suggests that Bi_2Se_3 can be classified as a strongly coupled topological insulator while Bi_2Te_3 and Sb_2Te_3 (figure 4.14) can be classified as a weakly coupled topological insulators. As such, these systems may be comparable to the layered 2D Topological Insulators in [53].

	Parameters according to [98]	Parameters according to [99]
	Gap oscillates	No oscillation
A_0 [eVÅ]	3.330	2.513
B_0 [eVÅ]	2.260	1.836
M_1 [eVÅ^2]	6.860	3.353
M_2 [eVÅ^2]	44.500	29.375

TABLE 4.1: Relevant model parameters of $\gamma_\parallel$ for the gap behavior in Bi_2Se_3 for two different sets of material parameters.

The material parameters used in these gap calculations are the parameters given in [99]. When considering the parameters given in [98], the periodic behavior is also observable in Bi_2Se_3 but with much longer gap oscillations that surpass the oscillation period size of the H_0 model for this material by a factor of three (figure 4.15). Hence, there may be a smooth transition from periodic to non-periodic gaps when the right parameters are modified. Keeping in mind the definition of the coupling strength $\gamma_\parallel = \frac{B_0^2}{A_0^2}\frac{M_2}{2M_1}$ and comparing the relevant parameters of Bi_2Se_3 in table 4.1, a suitable parameter to simulate the transition from non-periodic to periodic gap behavior, is M_1, because it

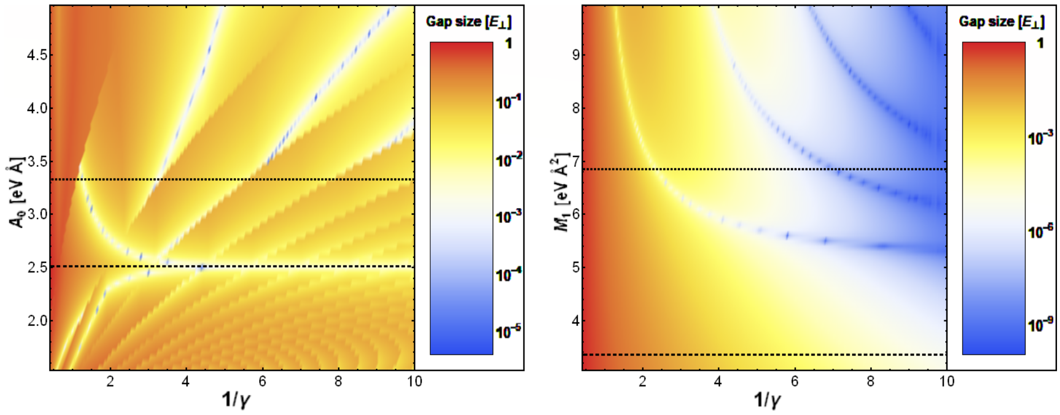

FIGURE 4.16: Change of gap behavior with material parameters M_1 and A_0, starting at the set of parameters for Bi_2Se_3 with no gap oscillations. While for M_1 there seems to be a smooth transition between periodic and non-periodic gap, for A_0, any small deviations increasing or decreasing its value lead to a periodic gap. Dashed (dotted) lines indicate the value of A_0 or M_1 for the parameter set with smooth (periodic) gap.

changes by a factor of two between the two sets of parameters and it does not contribute to the harmonic oscillator band energy distances $E_\perp$. Another interesting parameter to monitor is A_0, for the opposite reason: it is tied to $E_\perp$ and part of the σ_x and σ_y terms in the Hamiltonian and thus present in several measures of the system. Investigation of the gap size with varying material parameter results in interesting structures. Starting with the parameters that have been used for all previous calculations, when increasing M_1, the gap oscillations start to appear slowly and their frequency gets higher, the larger M_1 becomes. Notably, there seem to be regions of M_1 where the gap can get especially small (dark blue areas in figure 4.16). When considering the change of A_0, the underlying structure is even more appealing. Apparently, the value A_0 takes on in Bi_2Se_3, in interplay with all other material parameters, leads to the material gap being located in a "valley" with no oscillations along the $\frac{1}{\gamma}$-axis. However, even slight deviations to A_0 would result in oscillations of the material.

4.3.3 Four-fold Degeneracies

The twisting of bands previously mentioned and shown in figure 4.17a, also leads to further degeneracies on top of the already two-fold degenerate model. Since with decreasing γ more and more inverted bands get involved in the

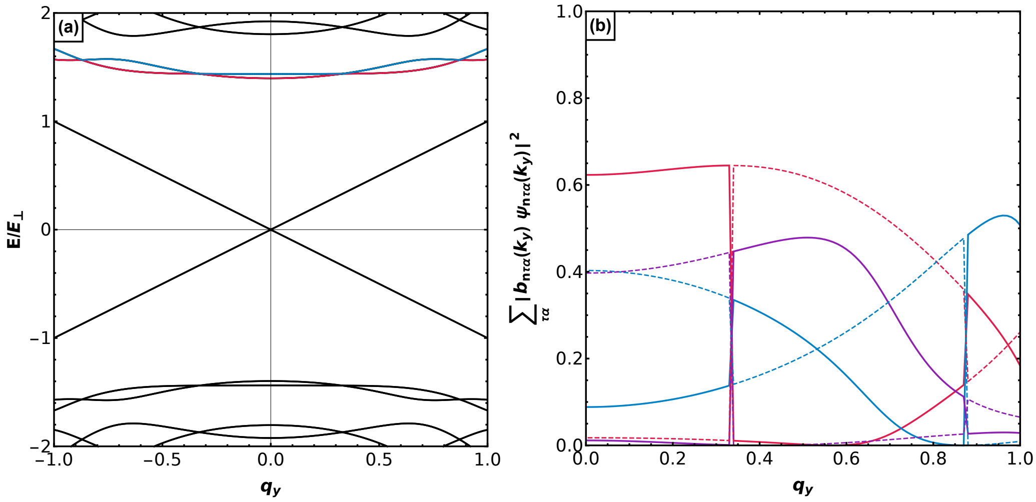

FIGURE 4.17: (a) Band structure of Bi_2Te_3 for a width of $\gamma = 0.65$. At this point, the bands of interest in red and blue are still separated and non-degenerate. The "twisting" of the bands occurs due to weak coupling of H_0 obeying two rules: (i) crossings between odd and even bands yield anti crossings, (ii) crossings between the same symmetry remain crossings. (b) The contributions of the oscillator prefactors as function of q_y where the red (blue) band in (a) is represented by the thick (dashed) lines.

$\mathscr{H}$ band formation around the Fermi level, the twisting effect becomes finer until two (each two-fold degenerate) bands become four-fold degenerate. By looking at the wave function densities of these states, the origin of the symmetry can not be established. All four states show the same density distribution as seen in figure 4.18b. Moreover, two of the four displayed wave functions exhibit spin up, while the other two exhibit spin down. The respective spin expectation values of these states only account for a degeneracy of factor two. More insight is gained by comparing the harmonic oscillator prefactors of two wave functions with equal spin expectation values as shown in figure 4.19, $|b_{n\mathbf{q}}^{(\alpha+)} \psi_{n\alpha\mathbf{q}}|^2$, defined in (4.23). While one pair of states is dominated by prefactors where n is uneven, the other pair is dominated by prefactors with even n. Notably, the harmonic oscillator function that, energy wise, is closest to a certain n in the H_0 picture, contributes the most to the full wave function.

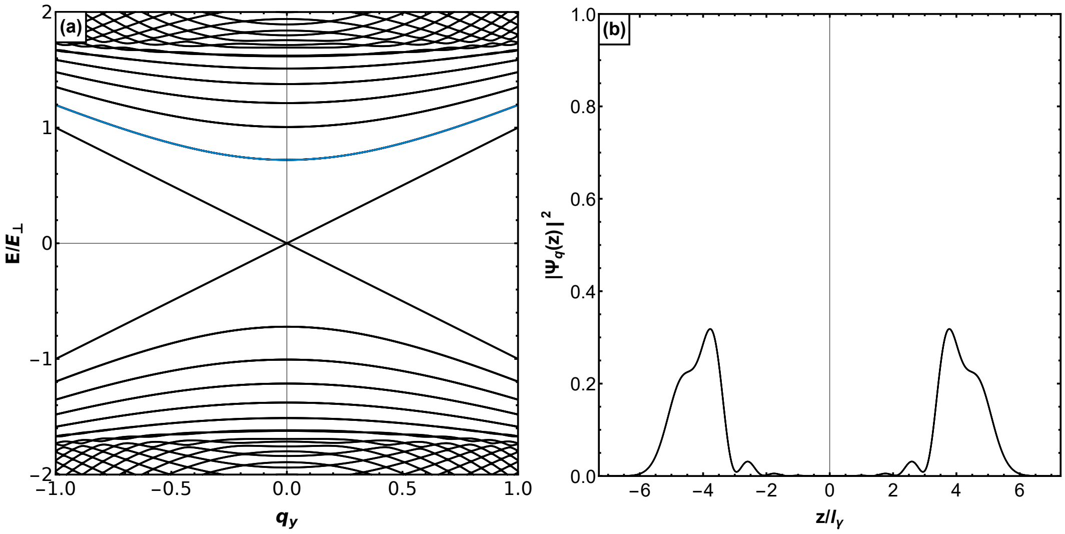

FIGURE 4.18: (a) Band structure of Bi_2Te_3 for a width of $\gamma = 0.15$. As the TI gets wider from $\gamma = 0.65$ in figure 4.17 to $\gamma = 0.15$ the bands colored in blue and red approach each other energetically and become degenerate. The wave function densities of the four degenerate bands in (b) are equal and lie on top of each other.

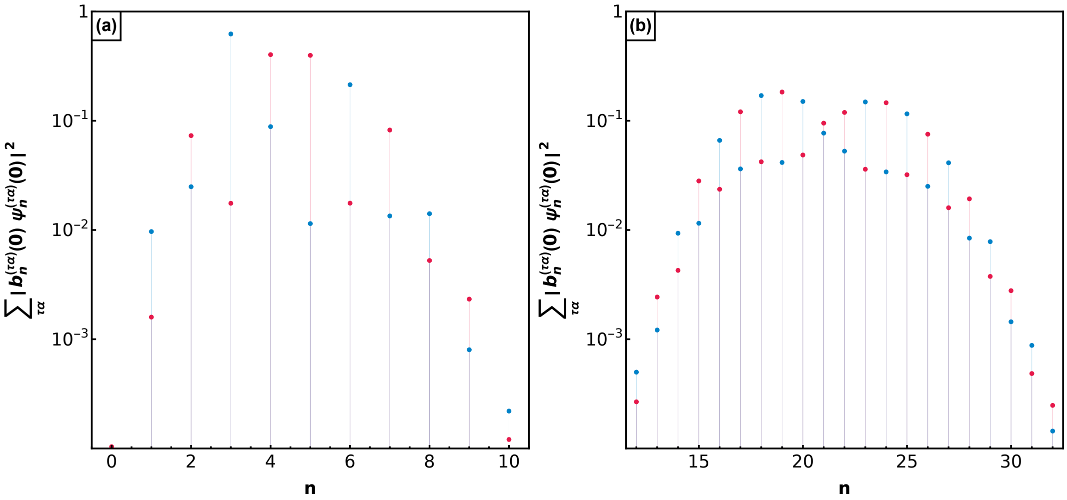

FIGURE 4.19: The decomposition of the wave function into its oscillator function prefactors for Bi_2Te_3 at (a) $\gamma = 0.15$ and (b) $\gamma = 0.65$. The wave function densities of the four degenerate bands are equal but the decomposition into their oscillator function prefactors shows variations.

4.4 Properties of the Full system $H_0 + H_\parallel + H_\epsilon$

The calculations so far did not account for the particle-hole asymmetry term $\epsilon_{\mathbf{q}_\perp}$ which is defined as

$$\epsilon_{\mathbf{q}_\perp} = C_0 - C_1\partial_z^2 + E_\perp \frac{C_2}{M_2}\mathbf{q}_\perp^2 = \tilde{\epsilon}_{\mathbf{q}_\perp} - C_1\partial_z^2 \tag{4.55}$$

and it lifts the symmetry between particles and holes which results in the deformation of the band structure and in a shift of the gap that varies with C_0. Only its part with derivative in z has to be treated perturbatively, the rest can be included in H_0 to give the shifted HO energy levels

$$\mathcal{E}^{(\alpha)}_{n\,\mathbf{q}_\perp} = \tilde{\epsilon}_{\mathbf{q}_\perp} + \alpha E_\perp \sqrt{\left[\gamma\left(n+\frac{1}{2}\right) + \gamma_0 + \mathbf{q}_\perp^2\right]^2 + \mathbf{q}_\perp^2}. \tag{4.56}$$

The diagonal nature of the Hamiltonian H_ϵ also means that particle-hole asymmetry has no effect on the spin structure within a band in the H_0 picture because, for a diagonal scalar addition, the eigenvectors of H_0 don't change. As for the full system $H = H_0 + H_\parallel + H_\epsilon$, the effects of H_ϵ are presented in figure 4.20 and figure 4.21. In the case of Bi_2Te_3, for the most part, H_ϵ results

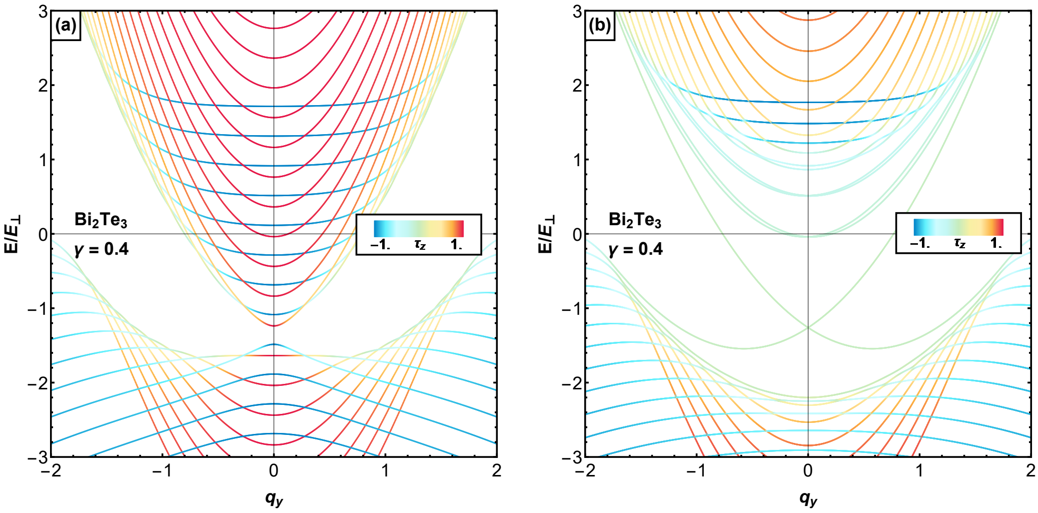

FIGURE 4.20: (a) The particle-hole asymmetry deforms the H_0 bands which translates directly to the full model in (b). Pictured is Bi_2Te_3 at $\gamma = 0.4$. Notable is the absence of the four-fold degeneracy discussed in section 4.3.3 and the non-linear behavior of the Dirac cones.

in the deformation and shift of the band structure where the parabolic nature of $\tilde{\epsilon}_{\mathbf{q}_\perp}$ is still recognizable within it. It also still leads to the formation of a Dirac cone with neutral pseudospin expectation value texture for the projection along the z axis, however, its linear behavior is gone. Its influence on Bi$_2$Se$_3$ is less significant and the Dirac cone is still well separated from the rest of the bands but the deformation is still clearly visible. As for Sb$_2$Te$_3$, some bulk bands are close to the Dirac point, even though the extent of the deformation on the rest of the band structure is small. However, the change in spin expectation value texture for $\hat{T}_z$ is quite significant. Some bands get so close to the Dirac cone crossing that non-zero pseudospin expectation values are in close proximity to the crossing. Moreover, the previous twisting of bands discussed in section 4.3.3 becomes less obvious and some of the bulk bands' pseudospin expectation value textures for $\hat{T}_z$ becomes inverted. Similarly, in Bi$_2$Te$_3$, the twisting of bands vanishes from the bands closest to the Dirac cone and appears in some of the higher bands instead and, except for at $\mathbf{q}_\perp = 0$, the four-fold degeneracy is lifted, too. In general, the magnitude of the pseudospin expectation values for the bands above and close to the Dirac cone decreases and, around $\mathbf{q}_\perp = 0$, these bands resemble a Dirac cone on their own. For Bi$_2$Se$_3$ the four-fold degeneracy is *not* lifted.

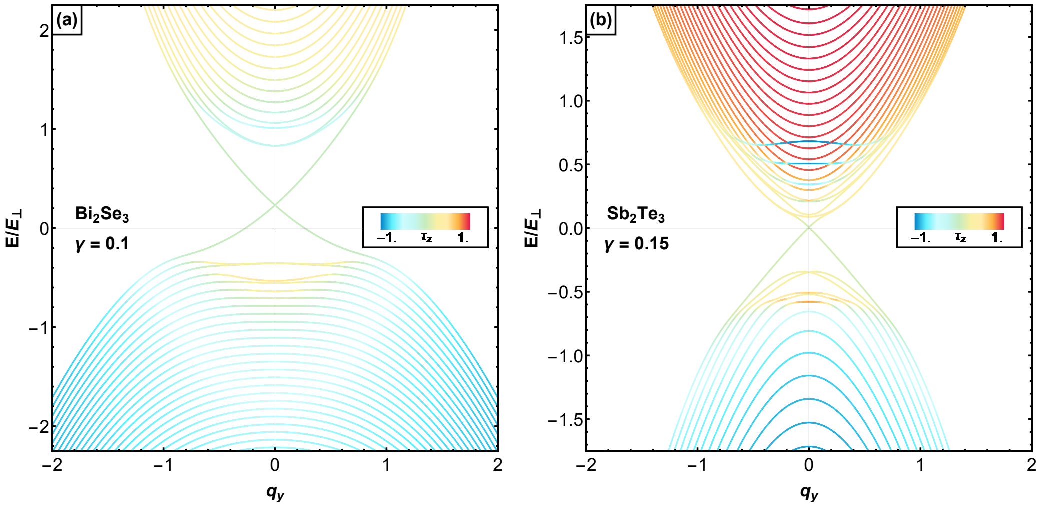

FIGURE 4.21: The particle-hole asymmetry also leads to the deformation of Bi$_2$Se$_3$ at $\gamma = 0.1$ (a) and Sb$_2$Te$_3$ at $\gamma = 0.15$ (b). While the cone crossing in Bi$_2$Se$_3$ is shifted, the impact on the rest of the band structure is small. The opposite is true for Sb$_2$Te$_3$ in which some bulk bands coincide with the Dirac cone.

Looking at the gap behavior, the general magnitude of the gap does not change even though its position with respect to the Fermi energy does. However, the oscillation period is affected by $\epsilon_{\mathbf{q}_\perp}$ and it becomes slightly smaller for both, Bi_2Te_3 and Sb_2Te_3 (figure 4.22). The same occurs for the behavior of the Dirac wave function at the center of the material - even though the general appearance and magnitude of the periodic behavior stays the same, the period slightly varies. Also, for both, Bi_2Te_3 and Sb_2Te_3, the position of the Dirac crossing with respect to the Fermi energy changes with material size. While for Sb_2Te_3 the crossing is driven below the Fermi level with increasing confinement strength, for Bi_2Te_3 the position of the crossing increases with confinement strength but never crosses the Fermi energy.

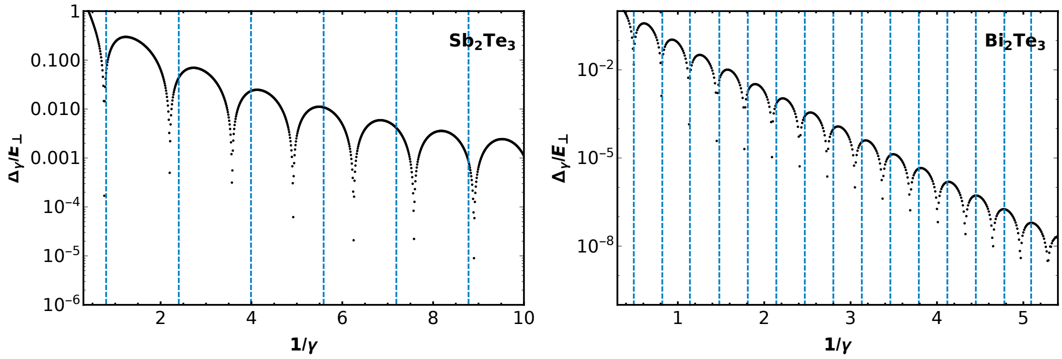

FIGURE 4.22: Shown are the gap oscillations with particle-hole asymmetry present. The dashed blue lines indicate the approximate positions of the gap minima in the particle-hole symmetric system $H_0 + H_{\|}$. For both pictured materials the period of oscillations decreases with the introduction of the asymmetry. For Bi_2Se_3 the gap remains non oscillatory.

When regarding the wave functions in general, only moderate change occurs. For the Dirac cones, the wave functions actually exhibit the same probability distributions at $\mathbf{q}_\perp = 0$ but deviate slightly otherwise with a non-zero probability to appear in the middle of the materials. The major part of the probability is still located on the surface of the material (figure 4.23). The change in the bulk bands is more notable but their general form stays the same, too.

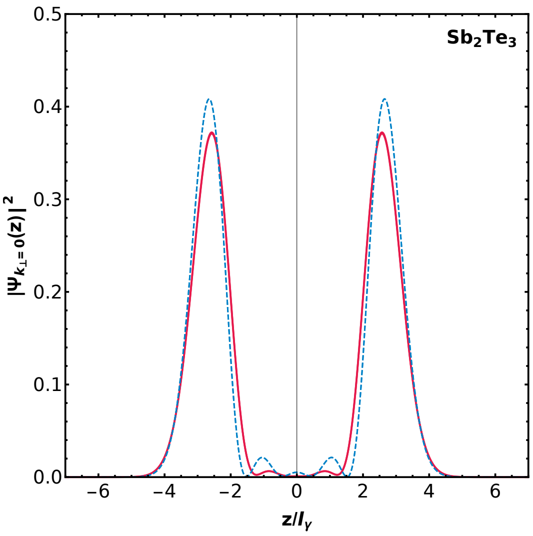

FIGURE 4.23: In contrast to the particle-hole symmetric system (red), the Dirac bands for Sb$_2$Te$_3$ with particle-hole asymmetry (blue, dashed) have a non vanishing probability density at the center of the material for $|q_y| > 0$.

4.5 Classification of observed results

Bi$_2$Se$_3$, Bi$_2$Te$_3$, and Sb$_2$Te$_3$ have been the subject of many studies in the past few years. Among these, there have been quite a few treating the band structure of the three materials, also observing Dirac cones for the surface states and band structures that are in qualitative agreement with the band structure results presented here [98, 109]. A feature that has been observed in several theoretical works with hard-wall confinement or open boundaries

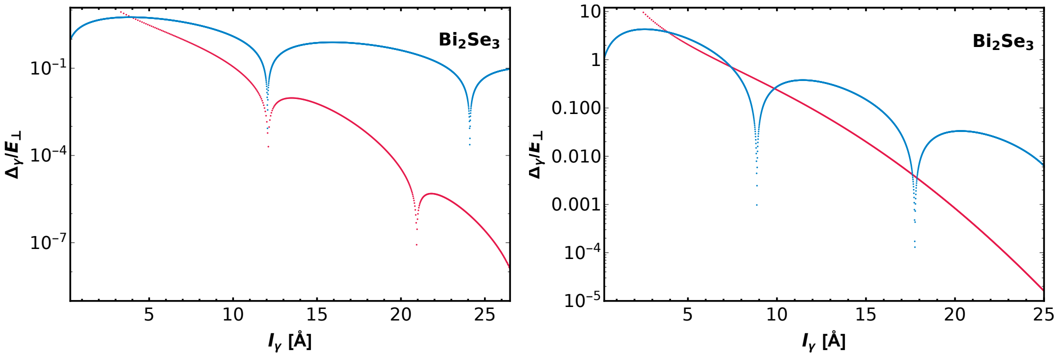

FIGURE 4.24: Comparison of the gap oscillations derived in [110] (blue) with the gap behavior obtained with $\mathscr{H}$ (red) for the material parameter set [98] (left) and [99] (right) for Bi$_2$Se$_3$. Notable is the lack of gap oscillations for the parameter set [99] in $\mathscr{H}$.

is the decaying oscillatory gap presented in section 4.3.2. The exponential decay/increase of the gap size is a property characteristic to the process of confinement as, fundamentally, particles in a box-type setup feel an increase in zero-point energy when the shape of the box is narrowed or sharpened. This behavior can be observed in the study presented here and is confirmed in several studies experimentally and theoretically [111–114]. The gap oscillations are also confirmed qualitatively by several other studies [109, 115, 116] and are in poor to good quantitative agreement with [110] as can be seen in figures 4.24 and 4.25. However, the non-oscillatory behavior of Bi_2Se_3 for the material parameter set given in [99] is not reproduced in [110] (figure 4.24) and the exponential decay of the gap size and the gap oscillation period deviates significantly for Bi_2Te_3.

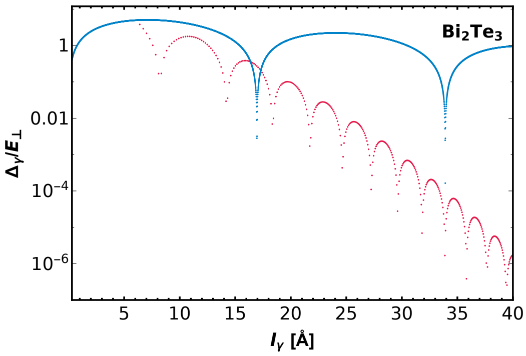

FIGURE 4.25: Comparison of the gap behavior derived in [110] (blue) with the gap behavior determined with the full Hamiltonian $\mathscr{H}$ (red) for Bi_2Te_3. Magnitude and oscillations are not in good agreement at all.

Moreover, the form of the surface state wave functions presented here is in qualitative agreement with the surface state wave functions determined in [113]. The same is true for the spin textures around the Dirac cone observed in [98, 116]. However, for all points of comparison, while being in good qualitative agreement, the length scale measure l_γ adopted throughout this study does not appear to be accurate and underestimates the realistic size of the material.

4.6 Summary

In this chapter the effects of a harmonic-oscillator-type confinement on the Bi_2Se_3 Topological Insulator family model Hamiltonian was investigated.

Overall, while there are quantitative deviations, the obtained results are in qualitative agreement with previous studies. An interesting outcome is the non-existence of gap oscillations in Bi_2Se_3 which is contrary to common literature. The investigation into model parameter space in section 4.3.2 in fact reveals that this is an almost singular behavior that only occurs for a specific combination of model parameters.

One thing that this model illustrates delightfully is the interplay of band inversion, size quantization, and band mixing when comparing the results for the analytically solvable part H_0 and the full model $\mathscr{H}$. Bare oscillator bands of H_0 tend to retain their pseudospin properties even after level repulsion due to the coupling in $\mathscr{H}$. Also, the expected inverted pseudospin distribution and the Dirac cone, whose formation can also be attributed to repulsing bare oscillator bands, are present and serve as evidence for the topological nature of the material. Finally, the location of the Dirac states on the surface of the material is confirmed, too, and an additional four-fold degeneracy is observed.

Chapter 5

Confined 3D Topological Insulator in a Magnetic Field

The stability of topological insulators relies on topology but also on the symmetries involved. Specifically time-reversal symmetry is a crucial ingredient. Thus, any perturbations that leave these symmetries intact, will not alter the topological structure of the system. The magnetic field, however, breaks time-reversal symmetry and the behavior of the system when symmetries are broken is fundamentally interesting. Moreover, it has been theorized that, in some cases, magnetic fields result in interesting results like the formation of Weyl cones [97].

In this section the effects of a magnetic field directed along the x axis as shown in section 3.1 is investigated. Due to the invariance of the Hamiltonian to a rotation in the k_x-k_y plane as shown in the previous chapter (4.11), it suffices to consider the magnetic field directed only into one direction within the x-y plane.

Generally, the magnetic field impact on crystals consists of a Zeeman term and a contribution due to the vector potential that is introduced into the Hamiltonian by Peierls substitution. As with the model without magnetic field, the objective is to determine an analytically solvable Hamiltonian H_0 that is perturbed by the band coupling term $H_{\|}$, the particle-hole asymmetry term H_{ϵ}, and the additional terms arising due to magnetic field effects. The Zeeman Hamiltonian is given in [98] but is rearranged to fit the different ordering basis states here. The g-factor values for this model are listed in table

	Parameters according to [98]			Parameters according to [99]		
	Bi_2Se_3	Bi_2Te_3	Sb_2Te_3	Bi_2Se_3	Bi_2Te_3	Sb_2Te_3
g_{1z}	-25.40	-50.34	-14.45	-9.41	-168.18	-18.00
g_{2z}	4.10	6.88	14.32	1.67	9.71	10.80
g_{1p}	-4.12	-2.67	-2.43	-4.83	-4.64	-4.29
g_{2p}	4.80	3.43	16.55	-3.10	-4.57	-15.36

TABLE 5.1: Magnetic material parameters according to [98] and [99] for all involved materials. The g factors each have two contributions: the orbital g factor resulting from each atomic orbital and a higher order contribution that can be related to the effective mass [98].

5.1 and the Zeeman Hamiltonian H_Z reads

$$H_Z = \frac{\mu_B}{2} \begin{pmatrix} g_{1z}B_z & 0 & g_{1p}B_- & 0 \\ 0 & -g_{2z}B_z & 0 & g_{2p}B_+ \\ g_{1p}B_+ & 0 & -g_{1z}B_z & 0 \\ 0 & g_{2p}B_- & 0 & g_{2z}B_z \end{pmatrix} \tag{5.1}$$

where $\mu_B = \frac{e\hbar}{2m_e}$ is the Bohr magneton in SI units and $B_\pm = B_x \pm \mathrm{i}B_y$. Since only a magnetic field in one direction is considered, this Hamiltonian reduces to

$$H_Z(B) = B\,\frac{\mu_B}{2}\,(\sigma_x \otimes G) \quad \text{with} \quad G = \begin{pmatrix} g_{1p} & 0 \\ 0 & g_{2p} \end{pmatrix} \tag{5.2}$$

and $B = B_x$. Because the non-zero elements of (5.2) don't fit into the block structure of H_0, it will be treated as perturbation of $\mathscr{H}_n$. What is left is the effects of the Peierls substitution. In order to get an effective magnetic field in x-direction, one can define the vector potential

$$\mathbf{A} = \begin{pmatrix} 0 \\ -B\,z \\ 0 \end{pmatrix} \tag{5.3}$$

which is then introduced into the Hamiltonian H_0 by the replacement within the wave vectors

$$\mathbf{k} \to \mathbf{k} - \frac{e}{\hbar}\mathbf{A}. \tag{5.4}$$

Hence, the actual replacement only takes place in k_y

$$k_y \to k_y + \frac{eB}{\hbar} z = k_y + \frac{z}{l_B^2}\,\mathrm{Sgn}(eB) \tag{5.5}$$

where the magnetic length is defined as $l_B(B) = \sqrt{\frac{\hbar}{eB}}$. Reviewing H_0 when it still contains the pure harmonic oscillator operator H_O in (4.5), one finds that the essential terms for the replacement are $\mathscr{M}_{n\,\mathbf{k}_\perp}$, H_O, and $A_0 k_\pm$. Moreover, one notes that it is possible to include parts of the Peierls substitution in the harmonic oscillator operator to get a shifted harmonic oscillator with effective frequency $\Omega_\mu(l_\gamma, l_B)$. The result of the considerations outlined on the following pages is a Hamiltonian that has the same structure as H_0 but with modifications to its elements. It has the form

$$H_0(B) = \begin{pmatrix} \mathcal{M}_{\mathbf{k}_\perp}(B) & \mathcal{A}^*_{\mathbf{k}_\perp}(B) & 0 & 0 \\ \mathcal{A}_{\mathbf{k}_\perp}(B) & -\mathcal{M}_{\mathbf{k}_\perp}(B) & 0 & 0 \\ 0 & 0 & \mathcal{M}_{\mathbf{k}_\perp}(B) & \mathcal{A}_{\mathbf{k}_\perp}(B) \\ 0 & 0 & \mathcal{A}^*_{\mathbf{k}_\perp}(B) & -\mathcal{M}_{\mathbf{k}_\perp}(B) \end{pmatrix} \tag{5.6}$$

where the parameters $\mathcal{M}_{\mathbf{k}_\perp}(B)$ and $\mathcal{A}_{\mathbf{k}_\perp}(B)$ now depend on the magnetic field. Starting with $\mathscr{M}_{\mathbf{k}_\perp}$, Peierls substitution leads to the modification

$$\mathscr{M}_{\mathbf{k}_\perp} \to M_0 + M_2\left(\mathbf{k}_\perp^2 + k_y \frac{z}{l_B^2}\mathrm{Sgn}(eB) + \frac{z^2}{l_B^4}\right) \tag{5.7}$$

where the z-dependent terms can be combined with the potential terms in H_O to

$$H_O \to -\frac{\hbar^2}{2m_\parallel}\partial_z^2 + M_2 k_y \frac{z}{l_B^2}\mathrm{Sgn}(eB) + M_2\frac{z^2}{l_B^4} + M_1\frac{z^2}{l_\gamma^4}. \tag{5.8}$$

With the definition of the effective oscillator length

$$\frac{M_1}{l_\mu^4} = \frac{M_1}{l_\gamma^4} + \frac{M_2}{l_B^4} \tag{5.9}$$

and the application of the binomial formula, one obtains

$$H_O = -\frac{\hbar^2}{2m_\parallel}\partial_z^2 + \frac{M_1}{l_\mu^4}\left[z + \mathrm{Sgn}(eB)\, l_B^2\left(1 - \frac{l_\mu^4}{l_\gamma^4}\right)k_y\right]^2 - M_2 k_y^2\left(1 - \frac{l_\mu^4}{l_\gamma^4}\right). \tag{5.10}$$

By moving the squared k_y term into $\mathscr{M}_{\mathbf{k}_\perp}$ and with the substitution

$$z \to z + \mathrm{Sgn}(eB) l_B^2 \left(1 - \frac{l_\mu^4}{l_\gamma^4}\right) k_y \tag{5.11}$$

in H_O, the same structure as without magnetic field is recovered, apart from a change in $\mathbf{k}_\perp^2$ as

$$\mathbf{k}_\perp^2 \to k_x^2 + \frac{l_\mu^4}{l_\gamma^4} k_y^2 \tag{5.12}$$

and thus

$$\mathscr{M}_{\mathbf{k}_\perp}(B) = M_0 + M_2 \left(k_x^2 + \frac{l_\mu^4}{l_\gamma^4} k_y^2\right) \quad \text{and} \quad H_O(B) = -\frac{\hbar^2}{2m_\parallel}\partial_z^2 + \frac{M_1}{l_\mu^4} z^2. \tag{5.13}$$

Due to the linear nature of the substitution, ∂_z does not change. However, the off diagonal parts of the two H_0 blocks, $A_0 k_\pm$ involve parts linear in z. Carrying out the Peierls substitution and substituting (5.11) results in

$$A_0 k_\pm \to A_0 \left(k_x \pm \mathrm{i} \frac{l_\mu^4}{l_\gamma^4} k_y \pm \mathrm{Sgn}(eB) \frac{z}{l_B^2}\right). \tag{5.14}$$

Treating the z-dependent part as perturbation and keeping the rest, $\mathcal{A}_{\mathbf{k}_\perp}$ can be treated as before with the redefinition

$$\mathcal{A}_{\mathbf{k}_\perp}(B) = A_0 \left(k_x + \mathrm{i} \frac{l_\mu^4}{l_\gamma^4} k_y\right). \tag{5.15}$$

As a result, the magnetic field effects on H_0 are summarized by the two Hamiltonians

$$H_Z(B) = B \frac{\mu_B}{2} (\sigma_x \otimes G) \quad \text{and} \quad H_B(B) = A_0 \frac{z}{l_B^2} (\sigma_z \otimes \tau_y) \,\mathrm{Sgn}(eB). \tag{5.16}$$

What remains is the change of H_ϵ after Peierls substitution. As before, derivatives do not change and substituting (5.11) results in

$$\epsilon_{\mathbf{k}_\perp}(B) = C_0 + C_1 k_z^2 + C_2 \left[k_x^2 + \left(\frac{l_\mu^4}{l_\gamma^4} k_y + \frac{z}{l_B^2} \mathrm{Sgn}(eB)\right)^2\right]. \tag{5.17}$$

5.1 Approximation of Magnetic Effects on H_0

Before considering the perturbation, the previous calculations open up the question of the impact of the magnetic field on the harmonic oscillator properties - its wave functions and ladder operators. After the substitutions, H_O is of the form of a harmonic oscillator with

$$m_{\|} = \frac{\hbar^2}{2M_1} \quad \text{and} \quad \Omega_\mu(B) = \frac{2M_1}{l_\mu^2 \hbar}. \tag{5.18}$$

Ω_μ can also be written in terms of the previous $\Omega_\gamma = \gamma \frac{A_0}{M_2 \hbar} := \frac{1}{\hbar}\Omega'_\gamma$ and the cyclotron frequency $\Omega_B = \frac{eB}{m_e} := \frac{1}{\hbar}\Omega'_B$

$$\Omega_\mu(B) = \sqrt{\Omega_\gamma^2 + \frac{M_2}{M_1}\Omega_B^2} := \frac{1}{\hbar}\Omega'_\mu(B) = \frac{1}{\hbar}\sqrt{(\Omega'_\gamma)^2 + \frac{M_2}{M_1}(\Omega'_B)^2}. \tag{5.19}$$

Combined, one can write the expressions of the operators $-\mathrm{i}\partial_z = \frac{\hat{p}_z}{\hbar}$ and $\hat{z}$ in terms of harmonic oscillator ladder operators a and $a^\dagger$

$$\frac{\hat{p}_z}{\hbar} = \frac{\mathrm{i}}{\hbar}\sqrt{\frac{\hbar}{2} m_{\|}\Omega_\mu(B)}\left(a^\dagger - a\right) = \mathrm{i}\sqrt{\frac{\Omega'_\mu(B)}{4M_1}}\left(a^\dagger - a\right) \tag{5.20}$$

and

$$\hat{z} = \sqrt{\frac{\hbar}{2}\frac{1}{m_{\|}\Omega_\mu(B)}}\left(a^\dagger + a\right) = \sqrt{\frac{M_1}{\Omega'_\mu(B)}}\left(a^\dagger + a\right). \tag{5.21}$$

This means that, apart from the changes already done to $\mathscr{M}_{\mathbf{k}_\perp}$, in $\mathcal{M}_{n\,\mathbf{q}_\perp}$ ($\mathbf{q}_\perp = \mathbf{k}_\perp / q_0$), the only other changes occur in the oscillator frequency and one gets the effective gap parameter

$$\mathcal{M}_{n\,\mathbf{q}_\perp}(B) = E_\perp\left[\gamma_0 + \left(q_x^2 + \frac{l_\mu^4}{l_\gamma^4}q_y^2\right) + \frac{\Omega'_\mu(B)}{E_\perp}\left(n + \frac{1}{2}\right)\right]. \tag{5.22}$$

The magnetic field has no influence on $H_{\|}$ - it contains derivatives which are not affected by the change of variables because the variables are only shifted by linear addition. Therefore, the calculation for this stays the same and one gets Γ_n and $\mathcal{E}_n$ like in (4.37) but with $\mathcal{M}_{n\,\mathbf{k}_\perp}$ and $\mathscr{E}^{(\alpha)}_{n\,\mathbf{k}_\perp}$ being replaced by their versions in a magnetic field, specifically

$$\mathscr{E}_{n\,\mathbf{q}_\perp}^{(\alpha)}(B) = \alpha E_\perp \sqrt{\left[\frac{\Omega'_\mu}{E_\perp}\left(n+\frac{1}{2}\right)+\gamma_0+q_x^2+\frac{l_\mu^4}{l_\gamma^4}q_y^2\right]^2+\left|\frac{\mathcal{A}_{\mathbf{q}_\perp}}{E_\perp}\right|^2} \tag{5.23}$$

where

$$\frac{\Omega'_\mu(B)}{E_\perp} = \sqrt{\gamma^2+\frac{4M_1M_2^3}{A_0^4}\frac{1}{l_B^4}}. \tag{5.24}$$

This leaves determining the $\mathscr{H}_n$ representations of H_Z and H_B. Particle-hole asymmetry being neglected, an overview over all terms involved to determine $\mathscr{H}_n$ is

$$H_B = \mathrm{i}\frac{A_0}{l_B^2}\begin{pmatrix} 0 & -z & 0 & 0 \\ z & 0 & 0 & 0 \\ 0 & 0 & 0 & z \\ 0 & 0 & -z & 0 \end{pmatrix},\ H_\parallel = \mathrm{i}B_0\begin{pmatrix} 0 & 0 & 0 & -\partial_z \\ 0 & 0 & \partial_z & 0 \\ 0 & \partial_z & 0 & 0 \\ -\partial_z & 0 & 0 & 0 \end{pmatrix},$$
$$\text{and } H_Z = \frac{\mu_B B}{2}\begin{pmatrix} 0 & 0 & g_{1p} & 0 \\ 0 & 0 & 0 & g_{2p} \\ g_{1p} & 0 & 0 & 0 \\ 0 & g_{2p} & 0 & 0 \end{pmatrix}. \tag{5.25}$$

Calculating the Zeeman contributions to $\mathscr{H}_n$ is done by sandwiching

$$H_Z = B\left[\sigma_x \otimes \begin{pmatrix} g_{1p} & 0 \\ 0 & g_{2p} \end{pmatrix}\right] \tag{5.26}$$

between $\langle m\tau\beta|$ and $\sum_{n\sigma\alpha} b_{n\,\mathbf{q}_\perp}^{(\sigma,\alpha)}|n\sigma\alpha\rangle$. One gets

$$\int_{-\infty}^{\infty}\mathrm{d}z\,\frac{\mu_B}{2}B\sum_{n\sigma\alpha} b_{n\mathbf{q}_\perp}^{(\sigma,\alpha)}\left[\langle\tau|\sigma_x|\sigma\rangle\otimes\left(\left(\psi_{m\mathbf{q}_\perp}^{(\tau,\beta)}(z)\right)^*\begin{pmatrix} g_{1p} & 0 \\ 0 & g_{2p} \end{pmatrix}\psi_{m\mathbf{q}_\perp}^{(\tau,\beta)}(z)\right)\right]. \tag{5.27}$$

Carrying out the integral in z gives a Kronecker delta δ_{nm} due to the harmonic oscillator functions and the σ_x part gives a $\delta_{\sigma,-\tau}$:

$$\frac{\mu_B}{2}B\sum_\alpha b_{m\mathbf{q}_\perp}^{(-\tau,\alpha)}\left[\left(\psi_{m\mathbf{q}_\perp}^{(\tau,\beta)}\right)^*\begin{pmatrix} g_{1p} & 0 \\ 0 & g_{2p} \end{pmatrix}\psi_{m\mathbf{q}_\perp}^{(-\tau,\alpha)}\right]. \tag{5.28}$$

Similar to $\Gamma_{n\mathbf{q}_\perp}$, what is left can be expressed first as

$$S^{\beta,+}_{m\mathbf{q}_\perp} b^{(-\tau,+)}_{m\mathbf{q}_\perp} + S^{\beta,-}_{m\mathbf{q}_\perp} b^{(-\tau,-)}_{m\mathbf{q}_\perp} \tag{5.29}$$

with

$$\begin{aligned} S^{\alpha,\beta}_{m\tau\mathbf{q}_\perp} = S^{\beta,\alpha}_{m\tau\mathbf{q}_\perp} = B\frac{\mu_B}{2}\Bigg[& g_{1p}\frac{\mathcal{A}^{(-\tau)}_{\mathbf{q}_\perp}}{|\mathcal{A}_{\mathbf{q}_\perp}|}\sqrt{\frac{(\mathcal{E}^{(\beta)}_{m\,\mathbf{q}_\perp}+\mathcal{M}_{m\,\mathbf{q}_\perp})(\mathcal{E}^{(\alpha)}_{m\,\mathbf{q}_\perp}+\mathcal{M}_{n\,\mathbf{q}_\perp})}{4\mathcal{E}^{(\beta)}_{m\,\mathbf{q}_\perp}\mathcal{E}^{(\alpha)}_{m\,\mathbf{q}_\perp}}} \\ & + \alpha\beta g_{2p}\frac{\mathcal{A}^{(\tau)}_{\mathbf{q}_\perp}}{|\mathcal{A}_{\mathbf{q}_\perp}|}\sqrt{\frac{(\mathcal{E}^{(\beta)}_{m\,\mathbf{q}_\perp}-\mathcal{M}_{m\,\mathbf{q}_\perp})(\mathcal{E}^{(\alpha)}_{m\,\mathbf{q}_\perp}-\mathcal{M}_{n\,\mathbf{q}_\perp})}{4\mathcal{E}^{(\beta)}_{m\,\mathbf{q}_\perp}\mathcal{E}^{(\alpha)}_{m\,\mathbf{q}_\perp}}}\Bigg] \end{aligned} \tag{5.30}$$

and the generalization of the complex conjugation of the off diagonal terms to

$$\mathcal{A}^{(\tau)}_{\mathbf{q}_\perp} = \begin{cases} \mathcal{A}_{\mathbf{q}_\perp} & \tau = 1 \\ (\mathcal{A}_{\mathbf{q}_\perp})^* & \tau = -1 \end{cases}. \tag{5.31}$$

This leads to the replacement $\mathcal{E}_n \to \mathcal{E}_n + \lambda_n$ in $\mathscr{H}_n$ when introducing the definitions

$$S_{n,\tau,\mathbf{q}_\perp} = \begin{pmatrix} S^{+,+}_{n\tau\mathbf{q}_\perp} & S^{+,-}_{n\tau\mathbf{q}_\perp} \\ S^{-,+}_{n\tau\mathbf{q}_\perp} & S^{-,-}_{n\tau\mathbf{q}_\perp} \end{pmatrix}, \quad \text{and} \quad \lambda_n = \begin{pmatrix} 0 & S_{n+\mathbf{q}_\perp} \\ (S_{n+\mathbf{q}_\perp})^\dagger & 0 \end{pmatrix}. \tag{5.32}$$

For the determination of the H_B matrix elements, it is convenient to use the representation

$$H_B = \mathrm{Sgn}(eB)\,(\sigma_z \otimes \tau_y)\,A_0\frac{z}{l_B^2}. \tag{5.33}$$

Sandwiching this between $\langle m\tau\beta|$ and $\sum_{n\sigma\alpha} b^{(\sigma,\alpha)}_{n\mathbf{q}_\perp}|n\sigma\alpha\rangle$ gives

$$\mathrm{Sgn}(eB)\frac{A_0}{l_B^2}\sum_{n\sigma\alpha} b^{(\alpha,\sigma)}_{n\mathbf{q}_\perp}\left[\langle\tau|\sigma_z|\sigma\rangle \otimes \left(\left(\psi^{(\tau,\beta)}_{m\mathbf{q}_\perp}\right)^* \tau_y\,\psi^{(\sigma,\alpha)}_{n\mathbf{q}_\perp}\right)\right]\langle m|z|n\rangle \tag{5.34}$$

where the oscillator functions are summarized in the braket notation $|n\rangle$. With the definition of the position operator (5.21) one gets $\tau\delta_{\sigma,\tau}$ for the σ_z matrix element and $\delta_{m,n+1}\sqrt{n+1}$ and $\delta_{m,n-1}\sqrt{n}$ for the oscillator function matrix element. The result is

$$\sum_{\alpha}\left[b^{(\sigma,\alpha)}_{m+1,\mathbf{q}_\perp}\left(\mathrm{i}L^{\alpha,\beta}_{m+1,m,\tau}\right)+b^{(\sigma,\alpha)}_{m-1,\mathbf{q}_\perp}\left(\mathrm{i}L^{\beta,\alpha}_{m+1,m,\tau}\right)^{*}\right] \tag{5.35}$$

with

$$\begin{aligned} L^{\beta,\alpha}_{n,m,\tau} = \frac{\tau A_0}{l_B^2}\sqrt{\frac{M_1 n}{\Omega'_\mu}}\Bigg[& \alpha\frac{\mathcal{A}^{(\tau)}_{\mathbf{q}_\perp}}{|\mathcal{A}_{\mathbf{q}_\perp}|}\sqrt{\frac{(\mathcal{E}^{(\beta)}_{m\,\mathbf{q}_\perp}+\mathcal{M}_{m\,\mathbf{q}_\perp})(\mathcal{E}^{(\alpha)}_{n\,\mathbf{q}_\perp}-\mathcal{M}_{n\,\mathbf{q}_\perp})}{4\mathcal{E}^{(\beta)}_{m\,\mathbf{q}_\perp}\mathcal{E}^{(\alpha)}_{n\,\mathbf{q}_\perp}}} \\ & -\beta\frac{\mathcal{A}^{(-\tau)}_{\mathbf{q}_\perp}}{|\mathcal{A}_{\mathbf{q}_\perp}|}\sqrt{\frac{(\mathcal{E}^{(\beta)}_{m\,\mathbf{q}_\perp}-\mathcal{M}_{m\,\mathbf{q}_\perp})(\mathcal{E}^{(\alpha)}_{n\,\mathbf{q}_\perp}+\mathcal{M}_{n\,\mathbf{q}_\perp})}{4\mathcal{E}^{(\beta)}_{m\,\mathbf{q}_\perp}\mathcal{E}^{(\alpha)}_{n\,\mathbf{q}_\perp}}}\Bigg] \end{aligned} \tag{5.36}$$

where the relation $(L^{\beta,\alpha}_{n,m,\tau}/\sqrt{n})^{*} = -L^{\beta,\alpha}_{m,n,\tau}/\sqrt{m}$ holds. With the further definition

$$\Lambda_n = \mathrm{i}\begin{pmatrix} L^{++}_{n+1,n,+} & L^{-+}_{n+1,n,+} & 0 & 0 \\ L^{+-}_{n+1,n,+} & L^{--}_{n+1,n,+} & 0 & 0 \\ 0 & 0 & L^{++}_{n+1,n,-} & L^{+-}_{n+1,n,-} \\ 0 & 0 & L^{-+}_{n+1,n,-} & L^{--}_{n+1,n,-} \end{pmatrix} \tag{5.37}$$

this result can be incorporated into $\mathscr{H}_n$.

Due to the changes in the particle-hole asymmetric term $\epsilon_{\mathbf{q}_\perp}$ in (5.17) there arise further contributions in the full Hamiltonian. Firstly, the terms linear in z lead to the evaluation of the term

$$2k_y\frac{C_2}{l_B^2}\left(1+\frac{M_2}{M_1}\frac{l_\mu^4}{l_B^4}\right)\sum_{n\sigma\alpha} b^{(\sigma,\alpha)}_{n,\mathbf{q}_\perp}\langle m\tau\beta|z|n\sigma\alpha\rangle \tag{5.38}$$

which results in a correction $\Lambda_n \to \Lambda_n + \Lambda_n^{\epsilon}$ by using the expression of z as harmonic oscillator ladder operators, where

$$\Lambda_n^{\epsilon} = \begin{pmatrix} d^{++}_{n+1,n,+} & d^{+-}_{n+1,n,+} & 0 & 0 \\ d^{-+}_{n+1,n,+} & d^{--}_{n+1,n,+} & 0 & 0 \\ 0 & 0 & d^{++}_{n+1,n,-} & d^{-+}_{n+1,n,-} \\ 0 & 0 & d^{+-}_{n+1,n,-} & d^{--}_{n+1,n,-} \end{pmatrix} \tag{5.39}$$

and

$$d_{nm}^{\alpha\beta} = 2q_y \frac{C_2}{l_B^2}\left(1 + \frac{M_2}{M_1}\frac{l_\mu^4}{l_B^4}\right)\sqrt{\frac{M_1}{\Omega'_\mu}}\left[\sqrt{\frac{(\mathcal{E}_{m\,\mathbf{q}_\perp}^{(\beta)} + \mathcal{M}_{m\,\mathbf{q}_\perp})(\mathcal{E}_{n\,\mathbf{q}_\perp}^{(\alpha)} + \mathcal{M}_{n\,\mathbf{q}_\perp})}{4\mathcal{E}_{m\,\mathbf{q}_\perp}^{(\beta)}\mathcal{E}_{n\,\mathbf{q}_\perp}^{(\alpha)}}} \right.$$
$$\left. + \alpha\beta\sqrt{\frac{(\mathcal{E}_{m\,\mathbf{q}_\perp}^{(\beta)} - \mathcal{M}_{m\,\mathbf{q}_\perp})(\mathcal{E}_{n\,\mathbf{q}_\perp}^{(\alpha)} - \mathcal{M}_{n\,\mathbf{q}_\perp})}{4\mathcal{E}_{m\,\mathbf{q}_\perp}^{(\beta)}\mathcal{E}_{n\,\mathbf{q}_\perp}^{(\alpha)}}}\right]. \tag{5.40}$$

The contribution of $z^2 = \frac{M_1}{\Omega'_\mu}((a^\dagger)^2 + 2(a^\dagger a + 1) + a^2)$ is summarized in

$$\frac{C_2}{l_B^4}\frac{M_1}{\Omega'_\mu}\sum_{n\sigma\alpha} b_{n,\mathbf{q}_\perp}^{(\sigma,\alpha)}\langle m\tau\beta|(a^\dagger)^2 + 2(a^\dagger a + 1) + a^2|n\sigma\alpha\rangle. \tag{5.41}$$

This can be divided into a part proportional to the harmonic oscillator energies that serves as correction to the diagonal elements in $\mathscr{H}_n$ and a part with squared ladder operators which is a correction to the Δ_n matrices determined in (4.44). Δ_n then takes on the form $\Delta_n \to \Delta_n + \Delta_n^B$ where

$$\Delta_n^B = \begin{pmatrix} D_n^B & 0 \\ 0 & D_n^B \end{pmatrix}, \; D_n^B = \begin{pmatrix} \delta_{++}^n & \delta_{+-}^n \\ \delta_{-+}^n & \delta_{--}^n \end{pmatrix}, \tag{5.42}$$

and

$$\delta_{nm}^{\alpha\beta} = \frac{C_2 M_1}{l_B^4 \Omega'_\mu}\sqrt{n}\sqrt{n-1}\left[\sqrt{\frac{(\mathcal{E}_{m\,\mathbf{q}_\perp}^{(\beta)} + \mathcal{M}_{m\,\mathbf{q}_\perp})(\mathcal{E}_{n\,\mathbf{q}_\perp}^{(\alpha)} + \mathcal{M}_{n\,\mathbf{q}_\perp})}{4\mathcal{E}_{m\,\mathbf{q}_\perp}^{(\beta)}\mathcal{E}_{n\,\mathbf{q}_\perp}^{(\alpha)}}} \right.$$
$$\left. + \alpha\beta\sqrt{\frac{(\mathcal{E}_{m\,\mathbf{q}_\perp}^{(\beta)} - \mathcal{M}_{m\,\mathbf{q}_\perp})(\mathcal{E}_{n\,\mathbf{q}_\perp}^{(\alpha)} - \mathcal{M}_{n\,\mathbf{q}_\perp})}{4\mathcal{E}_{m\,\mathbf{q}_\perp}^{(\beta)}\mathcal{E}_{n\,\mathbf{q}_\perp}^{(\alpha)}}}\right]. \tag{5.43}$$

Finally, the impact of particle-hole asymmetry on the diagonal elements $\mathcal{E}_n$ can be summarized in the replacement

$$\begin{aligned}\mathcal{E}_n \to \mathcal{E}_n + E_\perp \Bigg[&\frac{C_0}{E_\perp} + \frac{C_2}{M_2}\mathbf{q}_\perp^2 + \frac{\Omega'_\mu C_1}{2M_1 E_\perp}(n+\frac{1}{2}) - 2\frac{C_2 M_1}{E_\perp \Omega'_\mu l_B^4}(n+\frac{1}{2}) \\ &+ q_y^2 \frac{C_2}{M_1}\frac{l_\mu^4}{l_B^4}\left(2+\frac{M_2}{M_1}\frac{l_\mu^4}{l_B^4}\right)\Bigg]\end{aligned} \tag{5.44}$$

in addition to the Zeeman terms added before. After combining these results, one gets the total Hamiltonian for the numeric simulation

$$\mathscr{H}_n = \left(\begin{array}{ccccccc} \mathcal{E}_0 & \Gamma_0+\Lambda_0 & \Delta_0 & & & & \\ (\Gamma_0+\Lambda_0)^\dagger & \mathcal{E}_1 & \Gamma_1+\Lambda_1 & \Delta_1 & & & \\ (\Delta_0)^\dagger & (\Gamma_1+\Lambda_1)^\dagger & \mathcal{E}_2 & \Gamma_2+\Lambda_2 & \Delta_2 & & \\ & . & . & . & . & . & \\ & & . & . & . & . & . \end{array}\right). \tag{5.45}$$

5.2 Properties of the System $H_0(B)$

As before, for the topological insulator with no external fields, it is of interest to what extent the magnetic field changes the unperturbed system H_0. Due to the redefinition of the harmonic oscillator frequency to $\Omega_\mu(B) = \sqrt{\Omega^2 + M_2/M_1\,\Omega_B^2}$ in (5.19), it is apparent that a Pythagorean positive shift occurs for all energy bands. Further changes occur at $q_y \neq 0$ due to the impact of the magnetic field on $\mathcal{M}_{n\,\mathbf{q}_\perp}$ and $\mathcal{A}_{\mathbf{q}_\perp}$. There also is a small asymmetry between the q_y terms in both these expressions now because $\mathcal{A}_{\mathbf{q}_\perp}$ picks up the q_y prefactor $(l_\mu/l_\gamma)^4$ and $\mathcal{M}_{n\,\mathbf{q}_\perp}$ picks up the q_y prefactor $(l_\mu/l_\gamma)^2$. However, due to the magnitude of this factor deviating from 1 only marginally, for example $l_\mu/l_\gamma = 0.999$ at $B = 2\text{T}$ for Bi_2Se_3, the overall impact of the magnetic field on the effective gap parameter is small. l_μ/l_γ is shown as function of B in figure 5.1 for all three materials.

The wave functions derived from $\mathcal{M}_{n\,\mathbf{q}_\perp}(B)$ and $\mathcal{A}_{\mathbf{q}_\perp}(B)$ change accordingly. Thus, overall, the change is small and, just like in the non-magnetic case, the spinor contributions to the full H_0 wave functions have to be normalized and the probability density only depends on the harmonic oscillator functions. This also means that their spin and pseudospin expectation values

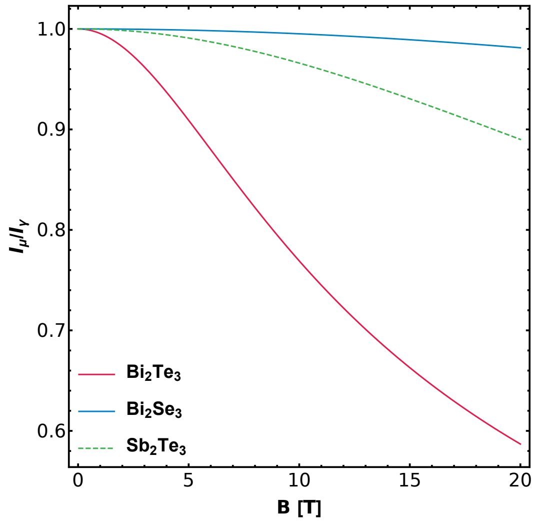

FIGURE 5.1: Shown are the ratios of the parameters l_μ and l_γ as function of the magnetic field for Bi_2Se_3 (blue), Bi_2Te_3 (red), and Sb_2Te_3 (green, dashed). The impact of magnetic fields on Bi_2Se_3 is much lower than on the other two materials.

do not deviate from their non magnetic versions apart from being slightly shifted energy wise.

5.3 Properties of the Coupled System $H_0(B) + H_\parallel + H_B(B) + H_Z(B)$

The simulation of the full Hamiltonian in a magnetic field is conducted in the same fashion as the non-magnetic Hamiltonian before. The accuracy of the calculation is decreasing slightly, meaning that the n chosen for $\mathscr{H}_n$ has to be larger than before to attain the same accuracy but the system converges at similar speed.

A central property of topological insulators is their time-reversal symmetry which is essential for the stability of the system. Thus, time-reversal symmetry-breaking external perturbations are expected to impact the model more than other perturbations. With the magnetic field being such a time-reversal symmetry-breaking field one would expect significant changes to the systems of the three materials. While the response to the magnitude of the applied magnetic field varies from material to material, their response in general is similar. The bulk bands split up into states separated by spin where the splitting is almost constant throughout momentum space. This

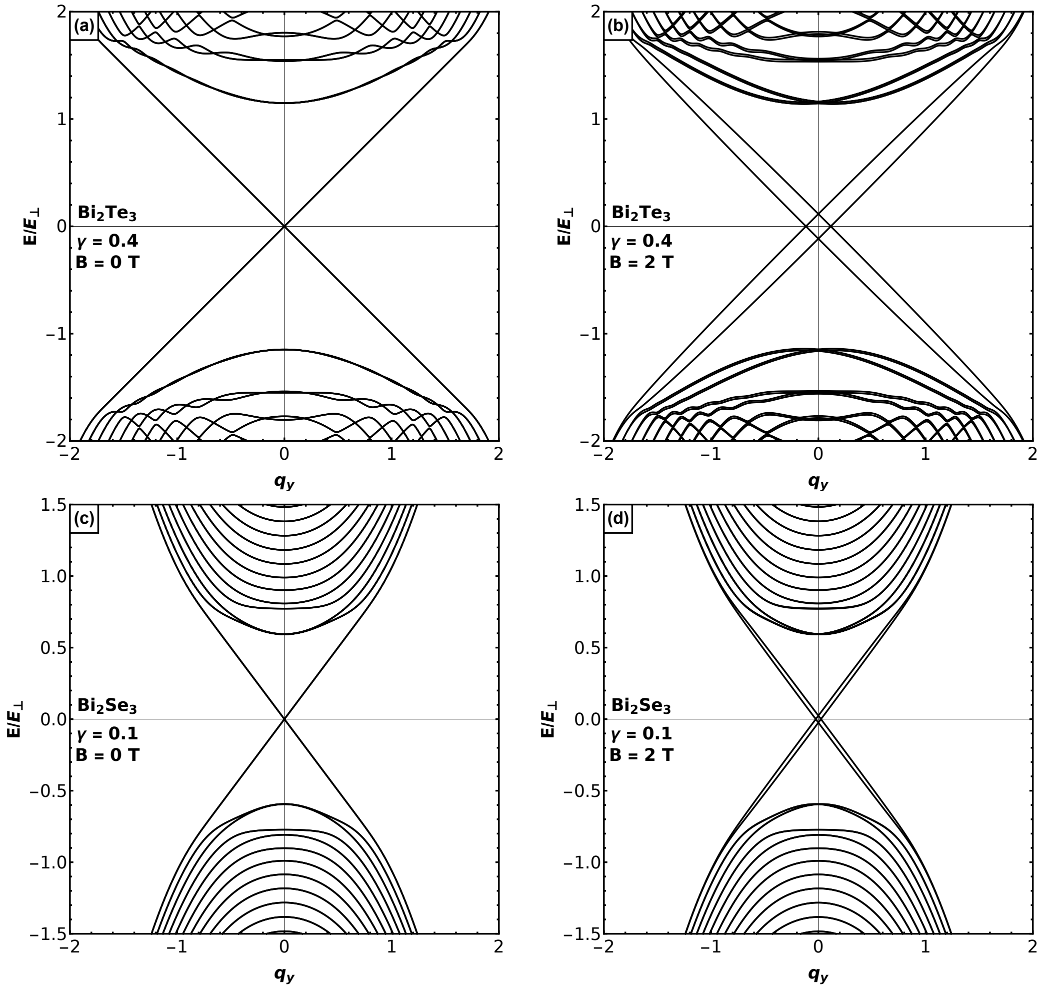

FIGURE 5.2: Band structure for Bi_2Te_3 (a,b) at $\gamma = 0.4$ and Bi_2Se_3 (c,d) at $\gamma = 0.1$. Notable are the cones being formed in both materials in (b,d) with a magnetic field of magnitude 2 T applied. The impact of the field on Bi_2Se_3 is significantly lower than for Bi_2Te_3 and, in general, the energy splitting in the Dirac bands is larger than in the bulk of the materials.

splitting lifts the four-fold degeneracy that was observed without magnetic field. While the response of Bi_2Te_3 and Sb_2Te_3 is quite strong, in comparison, for Bi_2Se_3 it is rather weak which can be observed in figure 5.2. If the magnetic field becomes very large, all bands are becoming flat and start to resemble Landau levels.

The change to the Dirac cones is more significant than to the bulk bands. First, the sheer magnitude of response to magnetic field is much larger than the response in energy splitting for the bulk bands. However, for the q_y that are in a range where the Dirac bands are energy wise located among the bulk bands, the splitting of the cones decreases significantly and shows the smaller splitting of the bulk bands. Second, the splitting of the Cones leads to the formation of two separate cones that resemble Weyl cones. Weyl fermions are represented by solutions to the zero mass Dirac equation and represent a special case of the Dirac equation. One crucial property of them is their spin momentum locking which means that, while particles moving in one direction are spin up (down), particles moving in the other direction have to be spin down (up). This leads to the investigation of the pseudospin and spin expectation values of the materials because it provides insight into the properties associated with Weyl fermions.

So far, the band structure has been illustrated on the q_y axis. With the magnetic field eliminating the symmetry between q_x and q_y, the definition of a more variable set of axes to project on is advantageous. For this, curves in q_x-q_y plane are defined in the following way. The "center" of the axis is located at $\mathbf{q}_0$ and the axis is defined through or around it. For example, to catch the spin behavior around a cone, it is sensible to set $\mathbf{q}_0$ to the crossing point of that cone and rotate around it at a given distance in momentum space to it, so that it is still well separated from the bulk bands. The axis is then defined along the curve

$$\mathbf{r}(\theta, \kappa) = \mathbf{q}_0 + \kappa \begin{pmatrix} \mathrm{Cos}(\theta) \\ \mathrm{Sin}(\theta) \end{pmatrix} \tag{5.46}$$

where κ measures the distance from the cone crossing point (or any point $\mathbf{q}_0$) in momentum space. For example, for $\theta = \pi/2$ and $\mathbf{q}_0 = (0, 0)$ the usual projection along the q_y axis is recovered while $\theta = 0$ gives the q_x axis. With these definitions and the spin expectation value texture shown in figure 5.3 and figure 5.4, it becomes apparent that the cones indeed feature Weyl fermion like states. For the cone states at $q_x = 0$ the spin-momentum locking is present in the z pseudospin projection expectation values and in the x pseudospin projection expectation values for the states with q_y fixed to the cone crossing point. This means that, when rotating the axis around the cone, so does the pseudospin projection in the $\hat{T}_z$-$\hat{T}_x$ spin plane. It is found that, for the axis rotation defined in (5.46), with $\mathbf{q}_0$ located at a cone crossing, pseudospin follows the rotation and is oriented along the pseudospin projection

$$-\mathrm{Cos}(\theta)\hat{T}_z + \mathrm{Sin}(\theta)\hat{T}_x. \tag{5.47}$$

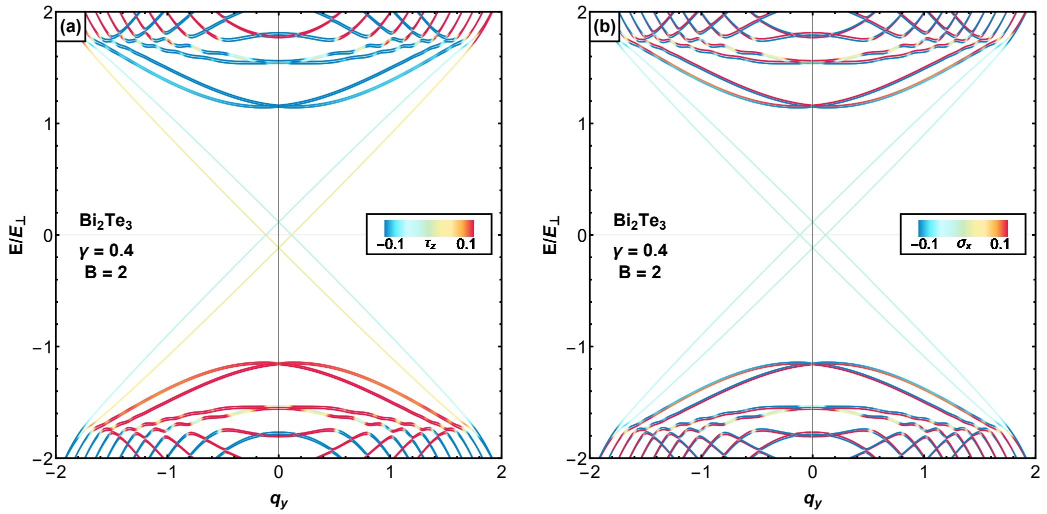

FIGURE 5.3: (a) Pseudospin expectation values for $\hat{T}_z$ in Bi$_2$Te$_3$ at $\gamma = 0.4$. (b) Real spin expectation values for $\hat{S}_x$. The expectation values of $\hat{S}_y$ vanish for all bands due to the magnetic field being aligned along the x-axis. For each split cone, right (left) moving particles show spin up (down), respectively.

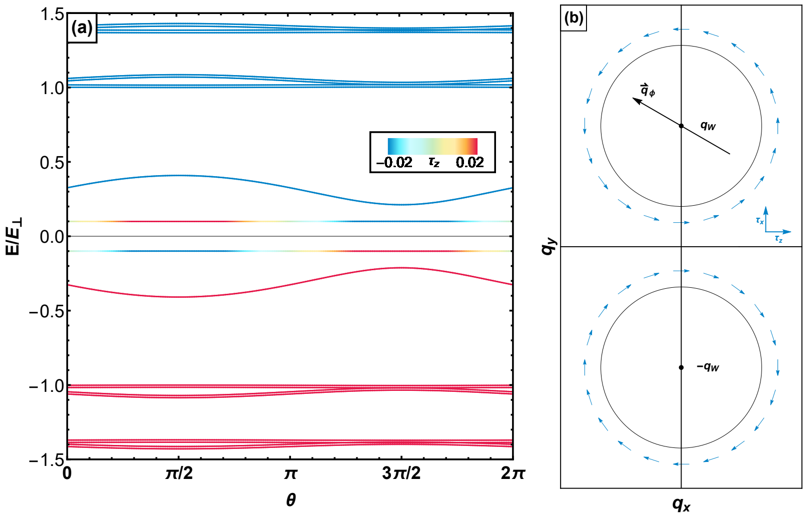

FIGURE 5.4: (a) Pseudospin expectation value plot of Bi$_2$Te$_3$ that shows pseudospin expectation value rotation for $\hat{T}_z$ around the split cones along the axis $\mathbf{r}(\theta, \kappa)$ for $\kappa = 0.1\, q_0$ and $\mathbf{q}_0 = (0, 0.1563)\, q_0$. As $\mathbf{r}(\theta, \kappa)$ rotates around the center of the cone, the expectation values of $\hat{T}_z$ oscillate from positive to negative and back. (b) Sketch of the pseudospin rotation within the $\hat{T}_z$-$\hat{T}_x$ plane with the rotation around the cones.

However, the magnitude of the pseudospin expectation values is small compared to the rest of the bands and lies within a range of ±0.1 but still non negligible compared to the neutral Dirac cones without magnetic field where pseudospin expectation values are essentially zero. The spin-momentum signature gets stronger with increasing magnetic field strength. For the bulk bands, the magnetic field has a smaller impact on the pseudospin expectation value distributions. However, it is notable that when bands move towards (away from) the Fermi level energetically, their pseudospin signature becomes weaker (stronger). As for real spin expectation values, electrons are expected to align along the direction of the magnetic field. Hence, the spin expectation value structure in z projection vanishes and is replaced by a spin expectation value distribution in x projection only. This is the case for all materials.

A property of Weyl fermions in Weyl semimetals is that the involved Weyl particles exhibit spin-momentum locking and that they are located in the bulk of the materials. Here, as it turns out, Weyl-like spin-momentum locking is observed in the cones that are located on the surface. The probability densities in figure 5.5 show this behavior for the Cone bands in Bi_2Te_3 but this structure occurs in all three materials. When considering the bulk wave functions, as before for the non-magnetic case, the bands energy wise closest to the cone bands show similar behavior where the probability densities are

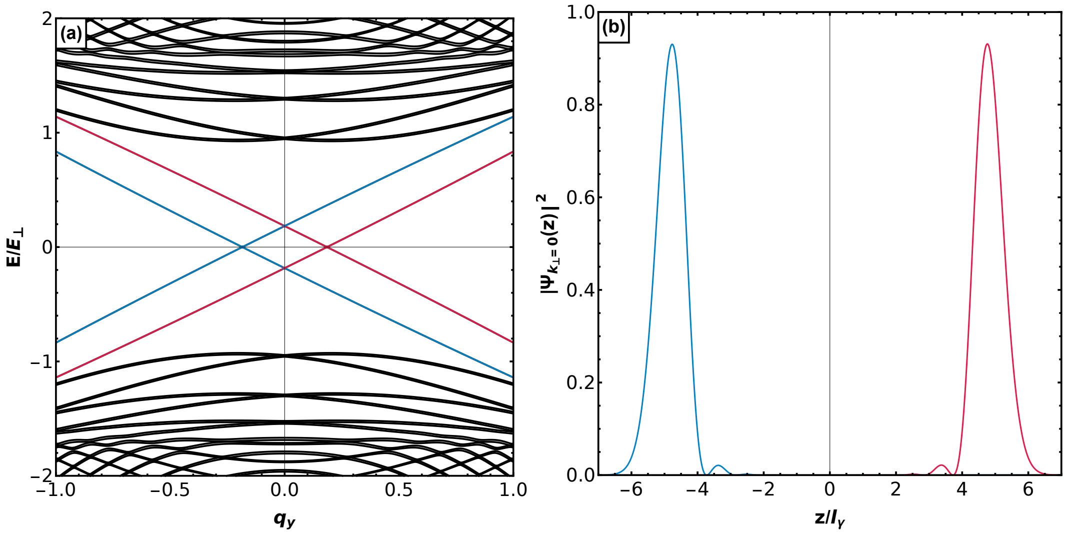

FIGURE 5.5: The respective probability densities for the red and blue cone depicted in (a) are pictured in (b). Notable is that the two cones are located on opposite sides of the material which opposes the picture of Weyl cones like in Weyl semimetals.

distributed preferably on one side (figure 5.6). However, this property decreases when considering bands with energy bands further away from the Fermi energy.

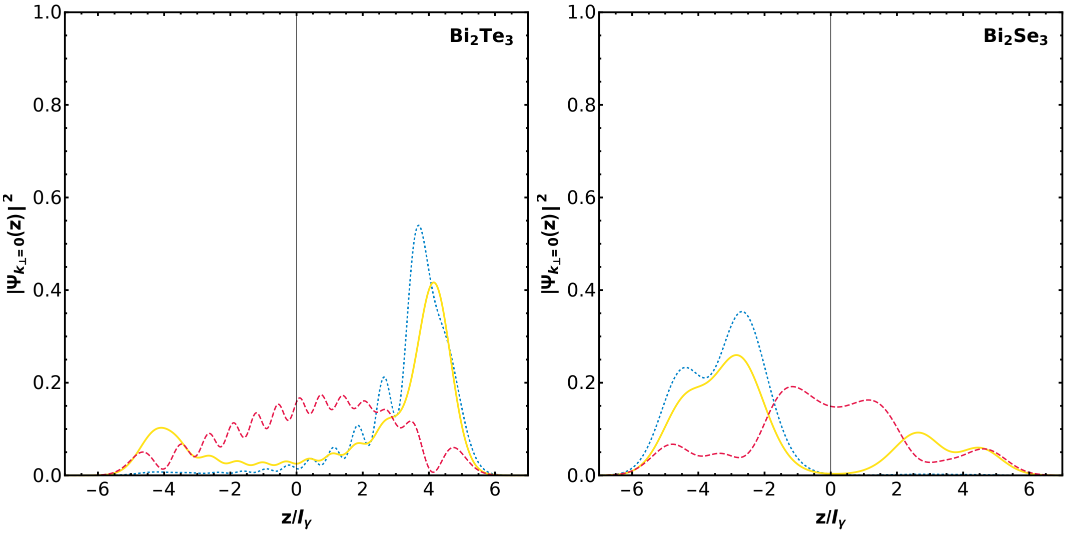

FIGURE 5.6: Probability density for the three band pairs closest to the Dirac band at $q_y = 0.1q_0$ for Bi_2Te_3 and Bi_2Se_3. The dotted blue lines depict the wave function densities of the energy band that are, energy wise, closest to the Dirac band. The thick yellow lines represent the second closest bands to the Dirac band and the dashed red lines show the bands third closest to the Dirac band. With further distance to the Dirac bands the bulk character of the bands increases.

Considering the apparent Weyl like behavior of the split cones could suggest the conclusion that the state the system is in, can actually be represented by a Graphene like model with the two Weyl cones being a representation of the K and K' points in Graphene. However, as expected, the Berry curvature vanishes numerically in all cases. This, in turn, would mean that the two cones can be described by a massless Graphene system. In line with this is the structure of the gaps of the cones which show no distinct structure and vanish numerically for all cases where split cones are present. On the other hand, when considering the cone located at $q_y = 0$ above or below the Fermi energy, the gap still shows the same structure as for the model without magnetic field (figure 5.7). One may conclude that the original Dirac cone is subject to a Zeeman splitting that leads to two cone crossings at the Fermi level with opposite momenta.

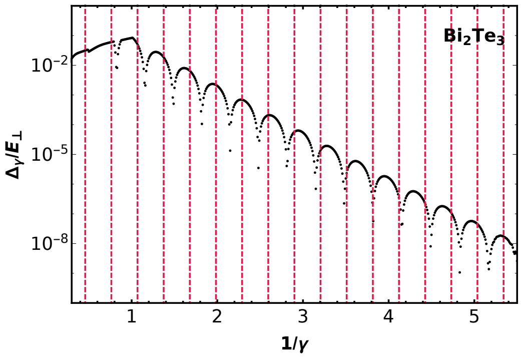

FIGURE 5.7: Gap behavior for the cones located at $q_y = 0$. The fact that the periodic gap closure does not occur in the split cones at the Fermi energy while the periodicity is still given for the cones above/below the Fermi energy, suggests that the splitting of the Dirac cone in momentum space can be seen as the result of a Zeeman shift.

5.4 Effective Low Energy Model: g-factors and Cone Splittings

To further investigate the splitting behavior of the Dirac cone subject to a magnetic field, it is useful to introduce an approximation to the full Hamiltonian that applies to the four Dirac bands around the Fermi level. The procedure here is to calculate these matrix elements for several values in **q** space and to recover the **q** dependencies consecutively as approximations.

For this, the explicit expressions $\Psi^a_{\mathbf{q}_\perp}(z)$ for a wave function representing band a, with *no* magnetic field present, are used. $\Psi^a_{\mathbf{q}_\perp}(z)$ is described by a set of $b^{(\alpha,\sigma,a)}_{n\,\mathbf{q}_\perp}$ as in (4.23), summarized to

$$\Psi^a_{\mathbf{q}_\perp}(z) = \sum_{n\sigma\alpha} b^{(\alpha,\sigma,a)}_{n\,\mathbf{q}_\perp} |n\sigma\alpha\rangle. \tag{5.48}$$

Then, let $a \in \{1,2,3,4\}$ be the four Dirac-state solutions for $H = H_0 + H_V + H_{||}$ with E_a as their respective energy eigenvalues and with $H_B(z,B) + H_Z(B)$ as perturbation. Taking the superposition of these four Dirac states as Ansatz for the full system $H_0 + H_V + H_{||} + H_B + H_Z$ this leads to

$$\Psi_{\mathbf{q}_\perp}(z) = \sum_a |a\rangle = \sum_a c_a \Psi^a_{\mathbf{q}_\perp} \tag{5.49}$$

where c_a is a complex number with $\sum_a |c_a|^2 = 1$. A new effective Schrödinger equation can be written as

$$\sum_{a,b} |b\rangle\langle b| \Big(H_0 + H_V + H_\parallel + H_B + H_Z \Big) |a\rangle = E \sum_a |a\rangle \tag{5.50}$$

and each matrix element arising due to the perturbation $H_B + H_Z$ reads

$$\langle a|H_B + H_Z|b\rangle = \frac{A_0}{l_B^2} \langle a| z \left(\sigma_z \otimes \tau_y\right) |b\rangle + B\frac{\mu_B}{2} \langle a| \left(\sigma_x \otimes G\right) |b\rangle. \tag{5.51}$$

Determining the matrix elements numerically results in an effective Hamiltonian H_E structured like

$$\begin{aligned} H_\mathrm{E}(\mathbf{q}_\perp, B, \gamma) =& E_\perp \left[\mathbb{1} \otimes \tau_z\right] \sqrt{q_x^2 + q_y^2} \\ & + \mu_0 B \left[r(\mathbf{q}_\perp, \gamma) \begin{pmatrix} 0 & \mathrm{e}^{\mathrm{i}\varphi} \\ \mathrm{e}^{-\mathrm{i}\varphi} & 0 \end{pmatrix} \otimes \tau_z + u(\mathbf{q}_\perp, \gamma)\, \mathbb{1} \otimes \tau_x \right], \end{aligned} \tag{5.52}$$

where $r(\mathbf{q}_\perp, \gamma)$ and $u(\mathbf{q}_\perp, \gamma)$ are approximating functions to the numerical data given by

$$r(\mathbf{q}, \gamma) = (62.44 q_y^2 + \tfrac{35.9}{\gamma} + 15.61) \tfrac{q_y^2}{q_x^2 + q_y^2} \tag{5.53}$$

$$u(\mathbf{q}, \gamma) = (62.48 q_x^2 + \tfrac{35.9}{\gamma} + 15.62) \tfrac{q_x^2}{q_x^2 + q_y^2} \tag{5.54}$$

for Bi_2Te_3 and

$$r(\mathbf{q}, \gamma) = (73.82 q_y^2 + \tfrac{4.543}{\gamma} - 1.93) \tfrac{q_y^2}{q_x^2 + q_y^2} \tag{5.55}$$

$$u(\mathbf{q}, \gamma) = (73.84 q_x^2 + \tfrac{4.544}{\gamma} - 1.93) \tfrac{q_x^2}{q_x^2 + q_y^2} \tag{5.56}$$

for Bi_2Se_3. The effective g-factor at $\mathbf{q}_\perp = 0$ can then be represented by either $\lim_{q_y \to 0} \lim_{q_x \to 0} r(\mathbf{q}_\perp, \gamma)$ or $\lim_{q_x \to 0} \lim_{q_y \to 0} u(\mathbf{q}_\perp, \gamma)$ and can be expressed as

$$\mathrm{Bi_2Te_3}: \quad g_\mathrm{E} \approx \lim_{q_y \to 0} \lim_{q_x \to 0} r(\mathbf{q}_\perp, \gamma) = \frac{35.9}{\gamma} + 15.61 = \frac{l_\gamma^2}{5.71} + 15.61 \tag{5.57}$$

$$\mathrm{Bi_2Se_3}: \quad g_\mathrm{E} \approx \lim_{q_y \to 0} \lim_{q_x \to 0} r(\mathbf{q}_\perp, \gamma) = \frac{4.543}{\gamma} - 1.93 = \frac{l_\gamma^2}{6.87} - 1.93. \tag{5.58}$$

For a small range of γ, this is in agreement with experimental results which found a range of $g_{\mathrm{Bi_2Se_3}} \approx 30$ [117] and g-factors of order 20 for $\mathrm{Bi_2Te_3}$ [118]

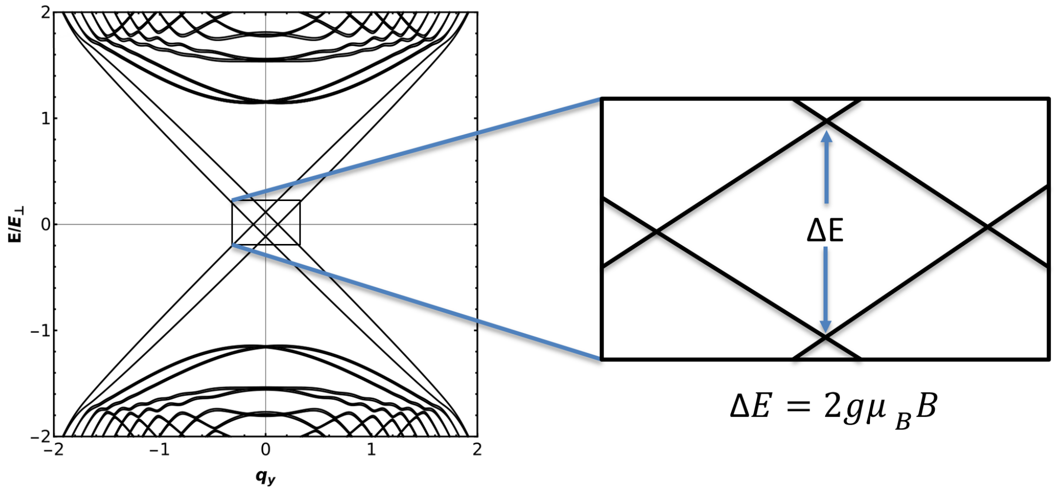

FIGURE 5.8: The g-factors related to the full numerical Hamiltonian $\mathscr{H}$ are determined by measuring the energy splitting of neighbouring Dirac bands at the origin.

in the bulk and $g_{\mathrm{Bi_2Se_3}} = -8.43$, $g_{\mathrm{Bi_2Te_3}} = -17.4$, and $g_{\mathrm{Sb_2Te_3}} = -2$ for the surface states [119]. Notable is the dependence of the g-factors on the Harmonic Oscillator parameter γ. It can be related to the Harmonic Oscillator length l_γ which is a measure for the size of the system. Thus, the behavior of the

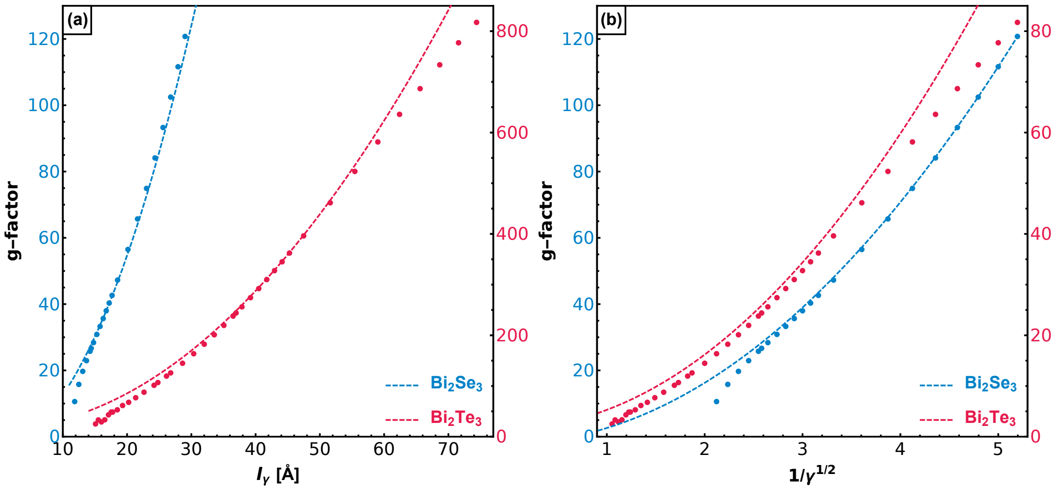

FIGURE 5.9: Shown are the effective g-factors of the surface states for $\mathrm{Bi_2Se_3}$ (blue) and $\mathrm{Bi_2Te_3}$ (red) over (a) the width of the material l_γ and (b) over $1/\gamma^{1/2}$ with normalized material parameters. The g-factors of both materials in this model depend on the width of the material and are approximated by (5.58) (dashed lines).

g-factors can be described by a function quadratic in l_γ and the major part of energy splitting in the magnetic field can be attributed to a two-band Zeeman splitting with effective g-factors shown in figure 5.9 for Bi_2Te_3 and Bi_2Se_3. The definition of the g-factors determined from the numerical approach is shown in figure 5.8. The g-factors are related to the energy splitting of to neighbouring Dirac bands ΔE by $\Delta E = \mu_B g B$. The splitting also manifests in the σ_x and σ_y terms in (5.52) which effectively represent Lorentz boosts in momentum space. The boost due to these terms also fits well with the numerical data given in figure 5.10. Remarkable is the strong dependence of the surface state g-factors on the size of the material which is already indicated by the z-dependency in (5.51) and also reflected in the numerical results.

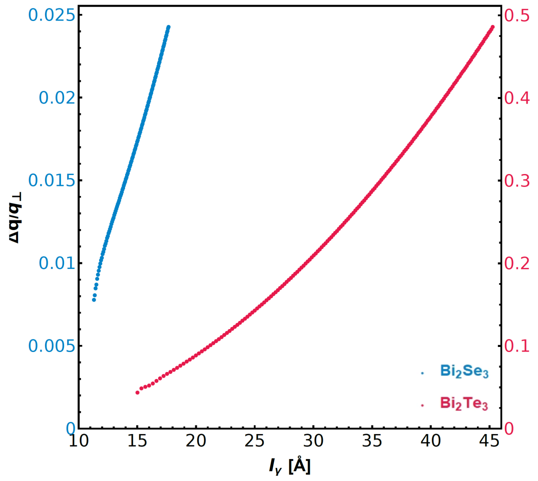

FIGURE 5.10: Shown is the distance between the cone crossings in momentum space over the width of the material l_γ in Å. The splitting in momentum space follows the same dependencies as the Zeeman splitting in energies.

5.5 Properties of the System $H_0(B) + H_{\parallel} + H_\epsilon(B) + H_B(B) + H_Z(B)$

Since the impact of the magnetic field on H_0 is negligible, as determined in section 5.2, the changes invoked by particle-hole asymmetry in a magnetic H_0 are nearly non-existent.

When investigating the full system, however, the changes are visible and can be significant. Most significantly, the splitting of the Dirac cone still occurs and the split cones are now at the according positions in momentum space shifted in energy by $\epsilon_{\mathbf{q}_\perp}$. Notable is also that the splitting for electrons is larger than for holes and that, the further the band is away from the Fermi level, the smaller is the impact of the magnetic field and the bands' splitting. Examples of this for Bi_2Se_3 and Bi_2Te_3 can be seen in figure 5.11. Just like for the system without particle-hole asymmetry, the magnitude of change varies between materials and it increases from Bi_2Se_3 over Bi_2Te_3 to Sb_2Te_3. Moreover, the gap doesn't change its behavior either. The periodicity is still present (absent) for the cone crossing at $q_y = 0$ in Bi_2Te_3 and Sb_2Te_3 (Bi_2Se_3) and the cone crossings of the split cones at the Fermi level remain numerically zero.

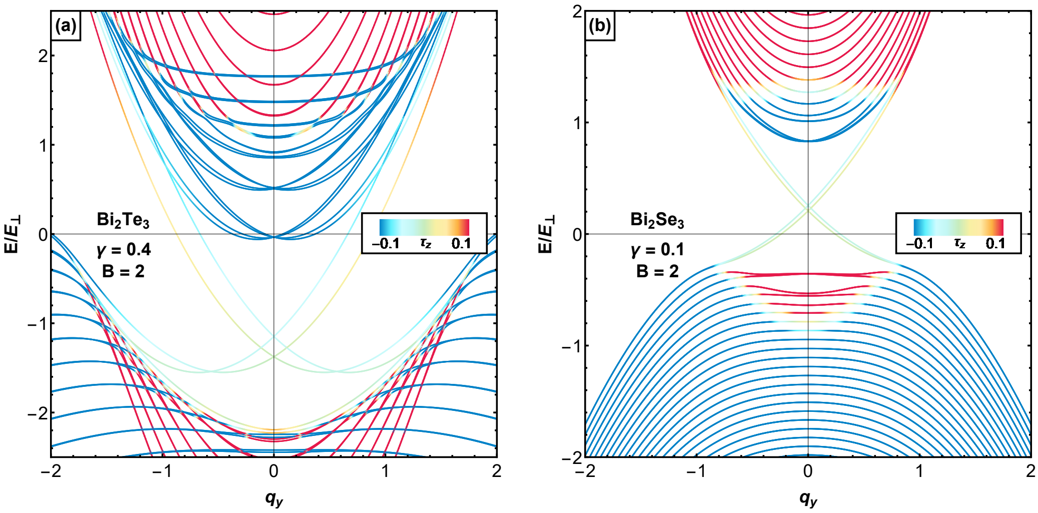

FIGURE 5.11: Band structure of (a) Bi_2Te_3 and (b) Bi_2Se_3 with particle-hole asymmetry present and magnetic field directed in x-direction and of magnitude 2 T.

The impact on the wave functions is small, too. The respective cone states still manifest on opposite sides of the materials and the bulk states show more bulk like behavior, the further they are from the Fermi level. However, the asymmetry leads to a different behavior for electrons which show bulk like behavior for lower distances to the Fermi energy than holes (figure 5.12). The asymmetry also manifests in the magnitude of pseudospin which is smaller for holes and larger for electrons. Finally, like for the particle-hole symmetric Hamiltonian, Berry Curvature vanishes in the whole q_x-q_y-plane and is thus topologically trivial.

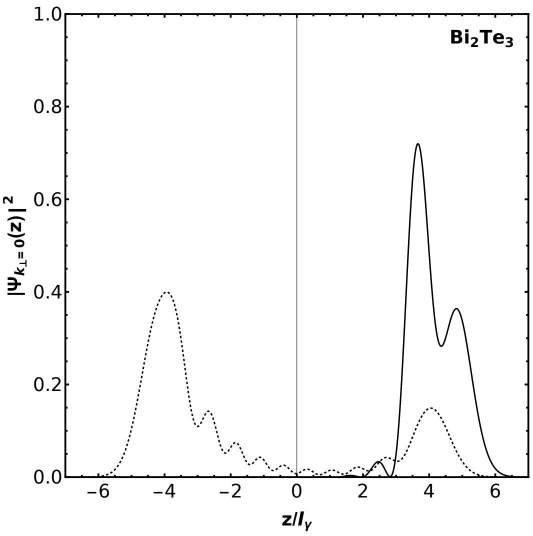

FIGURE 5.12: Wave function densities for bulk bands that are energy wise closest to the Dirac bands for holes (dashed) and electrons (thick) for Bi_2Te_3. While electrons behave like the Dirac states and are located on one side of the material, holes are located on both sides with a preference to one side. As bands further away from the Dirac bands are chosen, this behavior deteriorates towards bulk like band behavior.

5.6 Summary

In this chapter the effects of an in-plane magnetic field on the Bi_2Se_3 Topological Insulator family model Hamiltonian with a harmonic-oscillator-type confinement was investigated. The first central result here is the splitting of the Dirac cone into two separate cones that are located on opposite sides of the material which has been discussed in similar settings in [120, 121]. The pseudospin texture of these cones is remarkable in that it rotates around each cone as shown in figure 5.4. This is a feature that has also been observed in related studies [98, 116].

The splitting of the Dirac cones can be ascribed to an effective Zeeman splitting that increases the energy for one Dirac cone and decreases it for the other. This splitting energy difference is used to determine a g-factor associated with the in-plane magnetic field. Remarkable for these g-factors is that they strongly depend on the size of the material which has not been observed so far.

Chapter 6

Summary and Outlook

This project was set out to investigate the effects of a soft harmonic-oscillator-type quantum confinement on physical properties of the model Hamiltonian of the topological insulators Bi_2Se_3, Bi_2Te_3, and Sb_2Te_3. The materials in question represent quite different regions of the 3D-TI parameter space and, hence, exhibit distinctive features in the evolution of topological properties as the strength of the confinement is varied. The results obtained here are also straightforwardly generalized to any materials systems whose band structure is described by the same type of $\mathbf{k} \cdot \mathbf{p}$ Hamiltonian that forms the basis for the theoretical approach presented here, including Dirac semimetals [100, 101, 122] and other proposed topological insulators such as $Bi_2Te_2I_2$ [102].

The interplay of band inversion, size quantization, and band mixing is found to be governed by the relative magnitudes of unit-less parameters defined in (4.19). Characteristic features exhibited by the particular materials systems considered here can thus be rationalized in terms of the specific values of these parameters. Fundamentally, as the system size in the confined direction varies, the gaps of inverted bare-oscillator subbands are successively closing and reopening. The mixing of bare-oscillator subbands significantly modifies the bare-oscillator subband dispersions in the large-width regime ($\gamma < \gamma_{\|}$), establishing the vanishing-mass Dirac-like surface-state dispersion and eventually causing the disappearance of oscillations in the fundamental (lowest-subband) gap value. The robustness of TI phases with respect to band mixing and electron-hole asymmetry is established by tracking the evolution of band inversions by explicit consideration of the pseudospin value of eigenstates. In contrast, the occurrence of gap oscillations turns out to be a non-universal feature that cannot be viewed as a conclusive measure to monitor TI character in a quantum-confined system. Moreover, it is found that the parameter A_0 representing Bi_2Se_3 in this model lies in a region where small deviations lead to gap oscillations which may justify further investigations into the variation of model parameters. The effects of particle-hole asymmetry are mainly expressed as a deformation and shift of the band structure. Wave functions, pseudospin, and spin expectation values lose the symmetry between particles and holes, but the distinctive topological insulator properties remain.

When an in-plane magnetic field is applied, all three materials show an effective Zeeman splitting of the Dirac cone into two separate cones in $\mathbf{k}$ space. Due to the non-magnetic Hamiltonian's rotation invariance within the k_x-k_y plane, the two cones split in the direction the magnetic field is pointed at. The band splitting of the bulk band structure is weaker than the splitting of the Dirac cones in the surface states. The low energy effective Hamiltonian shows that the splitting of the cones originates from two sources. One being the Zeeman Hamiltonian in (5.2). The other contribution results from the vector potential of the in-plane magnetic field $\mathbf{A}$ which leads to effective Lorentz boosts in k_y and is summarized in H_B (5.25). The cones are located on opposite sides of the TI surface in confinement direction and show a rotation pattern with clockwise (counter clockwise) rotation of pseudospin expectation values projected into the T_x-T_z plane when rotating around a cone in $\mathbf{k}$ space. Calculations regarding the Berry curvature of the model Hamiltonian in a magnetic field delivered no visible curvature beyond numeric background noise. Particle-hole asymmetry has a similar effect on the full model Hamiltonian in a magnetic field as it has without magnetic field. The band structure is deformed and shifted but the qualitative properties, like the split Dirac cone on opposite sides of the material or the rotating pseudospin expectation values in $\mathbf{k}$ space remain present.

The conclusions presented in this thesis have been reached based on an approach where certain aspects of real materials were ignored. One of these is the finite size of thin-film samples in the plane perpendicular to the quantum-confined direction and any effects arising from the conducting lateral surfaces. However, apart from the edge-state structure in strong perpendicular magnetic fields [123], systems with a large-enough aspect ratio are well-described by models assuming them to be infinite in the transverse directions. A potential experimentally probeable outcome is the material-size-dependent effective g-factor for the surface states in all three materials which may be observed in the frame of topological insulators in ultra cold atom optical lattices that allow for harmonic confinement potentials [66, 103].

Bibliography

1. Gamow, G. *Biography of Physics* (Harper, 1961).
2. Kotulla, M. & Zülicke, U. Manipulating topological-insulator properties using quantum confinement. *New Journal of Physics* **19,** 073025. `http://stacks.iop.org/1367-2630/19/i=7/a=073025` (2017).
3. Goodstein, D. & Goodstein, J. Richard Feynman and the History of Superconductivity. *Physics in Perspective* **2,** 30–47. `http://dx.doi.org/10.1007/s000160050035` (2000).
4. Rowlinson, J. S. Thomas Andrews and the Critical Point. *Nature* **224,** 541–543. `https://www.nature.com/articles/224541a0` (1969).
5. Van Delft, D. & Kes, P. The discovery of superconductivity. *Physics Today* **63,** 38–43. `http://physicstoday.scitation.org/doi/10.1063/1.3490499` (2010).
6. Rutherford, E. F. The Scattering of α and β Particles by Matter and the Structure of the Atom. *Philosophical Magazine.* `https://doi.org/10.1080/14786440508637080` (1911).
7. Compton, A. H. A Quantum Theory of the Scattering of X-rays by Light Elements. *Phys. Rev.* **21,** 483–502. `https://link.aps.org/doi/10.1103/PhysRev.21.483` (1923).
8. Raman, C. V. & Krishnan, K. S. A New Type of Secondary Radiation. *Nature* **121,** 501–502. `https://doi.org/10.1038/121501c0` (1928).
9. Haslett, J. W. Phase Waves of Louis deBroglie. *American Journal of Physics* **40,** 1315–1320. `https://doi.org/10.1119/1.1986821` (1972).
10. Pauli, W. Über den Zusammenhang des Abschlusses der Elektronengruppen im Atom mit der Komplexstruktur der Spektren. *Zeitschrift für Physik* **31,** 765–783. `https://doi.org/10.1007/BF02980631` (1925).
11. Heisenberg, W. Über quantentheoretische Umdeutung kinematischer und mechanischer Beziehungen. *Zeitschrift für Physik* **33,** 879–893. `https://doi.org/10.1007/BF01328377` (1925).

12. Heisenberg, W. Über den anschaulichen Inhalt der quantentheoretischen Kinematik und Mechanik. *Zeitschrift für Physik* **43,** 172–198. `https://link.springer.com/article/10.1007/BF01397280` (1927).
13. Schrödinger, E. Quantisierung als Eigenwertproblem. *Annalen der Physik* **384,** 489–527. `https://onlinelibrary.wiley.com/doi/abs/10.1002/andp.19263840404` (1926).
14. Dirac, P. A. M. On the Theory of Quantum Mechanics. *Proc. Roy. Soc. A* **112,** 661–677. `https://royalsocietypublishing.org/doi/abs/10.1098/rspa.1926.0133` (1926).
15. Dirac, P. A. M. The quantum theory of the electron. *Proc. Roy. Soc. A* **117,** 610–624. `http://rspa.royalsocietypublishing.org/content/117/778/610` (1928).
16. London, F. & London, H. The electromagnetic equations of the supraconductor. *Proc. Roy. Soc. A* **149,** 71–88. `https://doi.org/10.1098/rspa.1935.0048` (1935).
17. Landau, L. D. On the theory of phase transitions. *Zh. Eks. Teor. Fiz.* **7,** 19–32 (1937).
18. Kondo, J. Resistance Minimum in Dilute Magnetic Alloys. *Progress of Theoretical Physics* **32,** 37–49. `https://academic.oup.com/ptp/article-lookup/doi/10.1143/PTP.32.37` (1964).
19. Wilson, K. G. The renormalization group: Critical phenomena and the Kondo problem. *Reviews of Modern Physics* **47,** 773–840. `https://doi.org/10.1103/RevModPhys.47.773` (1975).
20. Dyakonov, M. I. & Perel, V. I. Possibility of Orienting Electron Spins with Current. *JETP Lett.* **13,** 467. `http://jetpletters.ac.ru/ps/1587/article_24366.shtml` (1971).
21. Dyakonov, M. I. & Perel, V. I. Current-induced spin orientation of electrons in semiconductors. *Physics Letters A* **35,** 459–460. `http://www.sciencedirect.com/science/article/pii/0375960171901964` (1971).
22. Hirsch, J. E. Spin Hall Effect. *Phys. Rev. Lett.* **83,** 1834–1837. `http://link.aps.org/doi/10.1103/PhysRevLett.83.1834` (1999).
23. Murakami, S., Nagaosa, N. & Zhang, S.-C. Dissipationless Quantum Spin Current at Room Temperature. *Science* **301,** 1348–1351. `http://science.sciencemag.org/content/301/5638/1348` (2003).

24. Klitzing, K. v., Dorda, G. & Pepper, M. New Method for High-Accuracy Determination of the Fine-Structure Constant Based on Quantized Hall Resistance. *Phys. Rev. Lett.* **45,** 494–497. `http://link.aps.org/doi/10.1103/PhysRevLett.45.494` (1980).
25. Laughlin, R. B. Quantized Hall conductivity in two dimensions. *Physical Review B* **23,** 5632–5633. `https://journals.aps.org/prb/abstract/10.1103/PhysRevB.23.5632` (1981).
26. Thouless, D. J., Kohmoto, M., Nightingale, M. P. & den Nijs, M. Quantized Hall Conductance in a Two-Dimensional Periodic Potential. *Phys. Rev. Lett.* **49,** 405–408. `http://link.aps.org/doi/10.1103/PhysRevLett.49.405` (1982).
27. Halperin, B. I. Quantized Hall conductance, current-carrying edge states, and the existence of extended states in a two-dimensional disordered potential. *Physical Review B* **25,** 2185–2190. `https://journals.aps.org/prb/abstract/10.1103/PhysRevB.25.2185` (1982).
28. Berry, M. V. Quantal phase factors accompanying adiabatic changes. *Proc. R. Soc. Lond. A.* **392,** 1802. `https://royalsocietypublishing.org/doi/abs/10.1098/rspa.1984.0023` (1984).
29. Simon, B. Holonomy, the quantum adiabatic theorem, and Berry's phase. *Physical Review Letters* **51,** 2167–2170. `https://journals.aps.org/prl/abstract/10.1103/PhysRevLett.51.2167` (1983).
30. Wilczek, F. & Zee, A. Appearance of gauge structure in simple dynamical systems. *Physical Review Letters* **52,** 2111–2114. `https://journals.aps.org/prl/abstract/10.1103/PhysRevLett.52.2111` (1984).
31. Laughlin, R. B. Anomalous Quantum Hall Effect: An Incompressible Quantum Fluid with Fractionally Charged Excitations. *Phys. Rev. Lett.* **50,** 1395–1398. `http://link.aps.org/doi/10.1103/PhysRevLett.50.1395` (1983).
32. Semenoff, G. W. Condensed-Matter simulation of a three-Dimensional anomaly. *Physical Review Letters* **53,** 2449–2452. `https://journals.aps.org/prl/abstract/10.1103/PhysRevLett.53.2449` (1984).
33. Haldane, F. D. M. Model for a Quantum Hall Effect without Landau Levels: Condensed-Matter Realization of the "Parity Anomaly". *Phys. Rev. Lett.* **61,** 2015–2018. `http://link.aps.org/doi/10.1103/PhysRevLett.61.2015` (1988).

34. Chang, C.-Z. *et al.* Experimental Observation of the Quantum Anomalous Hall Effect in a Magnetic Topological Insulator. *Science* **340,** 167–170. `http://science.sciencemag.org/content/340/6129/167` (2013).
35. Avron, J. Y., Sadun, L., Segert, J. & Simon, B. Topological Invariants in Fermi Systems with Time-Reversal Invariance. *Physical review letters* **61,** 1329–1332. `https://journals.aps.org/prl/abstract/10.1103/PhysRevLett.61.1329` (1988).
36. Bravais, A. Mémoire sur les systèmes formés par des points distribués régulièrement sur un plan ou dans l'espace. *Journal de l'École Polytechnique* (1850).
37. Eves, H. W. *An introduction to the history of mathematics* `https://nla.gov.au/nla.cat-vn988803` (Holt, Rinehart and Winston, 1962).
38. Born, M. & Fock, V. Beweis des Adiabatensatzes. *Zeitschrift für Physik* **51,** 165–180. `https://doi.org/10.1007/BF01343193` (1928).
39. Kou, X., Fan, Y., Lang, M., Upadhyaya, P. & Wang, K. L. Magnetic topological insulators and quantum anomalous hall effect. *Solid State Communications* **215-216,** 34–53. `http://www.sciencedirect.com/science/article/pii/S0038109814004438` (2015).
40. Jeckelmann, B. & Jeanneret, B. The Quantum Hall Effect as an Electrical Resistance Standard. *Séminaire Pointcaré* **2,** 39–51. `http://www.bourbaphy.fr/jeanneret.pdf` (2004).
41. Kubo, R. Statistical-Mechanical Theory of Irreversible Processes. I. General Theory and Simple Applications to Magnetic and Conduction Problems. *Journal of the Physical Society of Japan* **12,** 570–586. `https://doi.org/10.1143/JPSJ.12.570` (1957).
42. Fruchart, M. & Carpentier, D. An introduction to topological insulators. *Comptes Rendus Physique* **14,** 779–815. `http://www.sciencedirect.com/science/article/pii/S1631070513001461` (2013).
43. Kane, C. L. & Mele, E. J. Quantum Spin Hall Effect in Graphene. *Phys. Rev. Lett.* **95,** 226801. `http://link.aps.org/doi/10.1103/PhysRevLett.95.226801` (2005).
44. Kane, C. L. & Mele, E. J. Z_2 Topological Order and the Quantum Spin Hall Effect. *Phys. Rev. Lett.* **95,** 146802. `https://journals.aps.org/prl/abstract/10.1103/PhysRevLett.95.146802` (2005).

45. Fukui, T. & Hatsugai, Y. Quantum Spin Hall Effect in Three Dimensional Materials: Lattice Computation of Z2 Topological Invariants and Its Application to Bi and Sb. *Journal of the Physical Society of Japan* **76,** 053702. `https://doi.org/10.1143/JPSJ.76.053702` (2007).
46. Fu, L. & Kane, C. L. Time reversal polarization and a Z_2 adiabatic spin pump. *Phys. Rev. B* **74,** 195312. `https://link.aps.org/doi/10.1103/PhysRevB.74.195312` (2006).
47. Fukui, T., Fujiwara, T. & Hatsugai, Y. Topological Meaning of Z2 Numbers in Time Reversal Invariant Systems. *Journal of the Physical Society of Japan* **77,** 123705. `https://doi.org/10.1143/JPSJ.77.123705` (2008).
48. Moore, J. E. & Balents, L. Topological invariants of time-reversal-invariant band structures. *Phys. Rev. B* **75,** 121306. `https://link.aps.org/doi/10.1103/PhysRevB.75.121306` (2007).
49. Qi, X.-L., Hughes, T. L. & Zhang, S.-C. Topological field theory of time-reversal invariant insulators. *Phys. Rev. B* **78,** 195424. `https://link.aps.org/doi/10.1103/PhysRevB.78.195424` (2008).
50. Wu, C., Bernevig, B. A. & Zhang, S.-C. Helical Liquid and the Edge of Quantum Spin Hall Systems. *Phys. Rev. Lett.* **96,** 106401. `https://link.aps.org/doi/10.1103/PhysRevLett.96.106401` (2006).
51. Xu, C. & Moore, J. E. Stability of the quantum spin Hall effect: Effects of interactions, disorder, and $\mathbb{Z}_2$ topology. *Phys. Rev. B* **73,** 045322. `https://link.aps.org/doi/10.1103/PhysRevB.73.045322` (2006).
52. Ryu, S., Schnyder, A. P., Furusaki, A. & Ludwig, A. W. W. Topological insulators and superconductors: tenfold way and dimensional hierarchy. *New Journal of Physics* **12,** 065010. `https://iopscience.iop.org/article/10.1088/1367-2630/12/6/065010` (2010).
53. Imura, K.-I., Okamoto, M., Yoshimura, Y., Takane, Y. & Ohtsuki, T. Finite-size energy gap in weak and strong topological insulators. *Phys. Rev. B* **86,** 245436. `https://link.aps.org/doi/10.1103/PhysRevB.86.245436` (2012).
54. Fu, L. Topological Crystalline Insulators. *Phys. Rev. Lett.* **106,** 106802. `https://link.aps.org/doi/10.1103/PhysRevLett.106.106802` (2011).

55. Rauch, T., Flieger, M., Henk, J., Mertig, I. & Ernst, A. Dual Topological Character of Chalcogenides: Theory for Bi_2Te_3. *Phys. Rev. Lett.* **112,** 016802. `https://link.aps.org/doi/10.1103/PhysRevLett.112.016802` (2014).
56. Min, H. *et al.* Intrinsic and Rashba spin-orbit interactions in graphene sheets. *Phys. Rev. B* **74,** 165310. `https://link.aps.org/doi/10.1103/PhysRevB.74.165310` (2006).
57. Yao, Y., Ye, F., Qi, X.-L., Zhang, S.-C. & Fang, Z. Spin-orbit gap of graphene: First-principles calculations. *Phys. Rev. B* **75,** 041401. `https://link.aps.org/doi/10.1103/PhysRevB.75.041401` (2007).
58. Bernevig, B. A. & Zhang, S.-C. Quantum Spin Hall Effect. *Phys. Rev. Lett.* **96,** 106802. `https://link.aps.org/doi/10.1103/PhysRevLett.96.106802` (2006).
59. Bernevig, B. A., Hughes, T. L. & Zhang, S.-C. Quantum Spin Hall Effect and Topological Phase Transition in HgTe Quantum Wells. *Science* **314,** 1757–1761. `http://science.sciencemag.org/content/314/5806/1757` (2006).
60. König, M. *et al.* Quantum Spin Hall Insulator State in HgTe Quantum Wells. *Science* **318,** 766–770. `http://science.sciencemag.org/content/318/5851/766` (2007).
61. Fu, L. & Kane, C. L. Topological insulators with inversion symmetry. *Phys. Rev. B* **76,** 045302. `http://link.aps.org/doi/10.1103/PhysRevB.76.045302` (2007).
62. Hsieh, D. *et al.* A topological Dirac insulator in a quantum spin Hall phase. *Nature* **452,** 970–974. `http://www.nature.com/nature/journal/v452/n7190/suppinfo/nature06843_S1.html` (2008).
63. Kohmoto, M., Halperin, B. I. & Wu, Y.-S. Diophantine equation for the three-dimensional quantum Hall effect. *Phys. Rev. B* **45,** 13488–13493. `https://link.aps.org/doi/10.1103/PhysRevB.45.13488` (1992).
64. Zhang, H. *et al.* Topological insulators in Bi_2Se_3, Bi_2Te_3, and Sb_2Te_3 with a single Dirac cone on the surface. *Nat Phys* **82,** 438–442. `http://dx.doi.org/10.1038/nphys1270` (2009).

65. Xia, Y. *et al.* Observation of a large-gap topological-insulator class with a single Dirac cone on the surface. *Nature* **5,** 398–402. `http://www.nature.com/nphys/journal/v5/n6/suppinfo/nphys1274_S1.html` (2009).

66. Stanescu, T. D., Galitski, V. & Das Sarma, S. Topological states in two-dimensional optical lattices. *Phys. Rev. A* **82,** 013608. `https://link.aps.org/doi/10.1103/PhysRevA.82.013608` (2010).

67. Bermudez, A. *et al.* Wilson Fermions and Axion Electrodynamics in Optical Lattices. *Phys. Rev. Lett.* **105,** 190404. `https://link.aps.org/doi/10.1103/PhysRevLett.105.190404` (2010).

68. Goldman, N. *et al.* Realistic Time-Reversal Invariant Topological Insulators with Neutral Atoms. *Phys. Rev. Lett.* **105,** 255302. `https://link.aps.org/doi/10.1103/PhysRevLett.105.255302` (2010).

69. Béri, B. & Cooper, N. R. $\mathbb{Z}_2$ Topological Insulators in Ultracold Atomic Gases. *Phys. Rev. Lett.* **107,** 145301. `https://link.aps.org/doi/10.1103/PhysRevLett.107.145301` (2011).

70. Zhang, X., Xiao, M., Cheng, Y., Lu, M.-H. & Christensen, J. Topological Sound. *Communications Physics* **1,** 97. `https://www.nature.com/articles/s42005-018-0094-4` (2018).

71. Fleury, R., Khanikaev, A. B. & Alù, A. Floquet topological insulators for sound. *Nature Communications* **7,** 11744. `https://doi.org/10.1038/ncomms11744` (2016).

72. Khanikaev, A. B. *et al.* Photonic topological insulators. *Nature Materials* **12,** 233–239. `https://doi.org/10.1038/nmat3520` (2012).

73. Jacobs, D. A., Miroshnichenko, A. E., Kivshar, Y. S. & Khanikaev, A. B. Photonic topological Chern insulators based on Tellegen metacrystals. *New Journal of Physics* **17,** 125015. `https://doi.org/10.1088/1367-2630/17/12/125015` (2015).

74. Delplace, P., Marston, J. B. & Venaille, A. Topological origin of equatorial waves. *Science* **358,** 1075–1077. `https://science.sciencemag.org/content/358/6366/1075` (2017).

75. Kitaev, A. Y. Unpaired Majorana fermions in quantum wires. *Physics-Uspekhi* **44,** 131–136. `https://iopscience.iop.org/article/10.1070/1063-7869/44/10S/S29` (2001).

76. Lutchyn, R. M., Sau, J. D. & Das Sarma, S. Majorana Fermions and a Topological Phase Transition in Semiconductor-Superconductor Heterostructures. *Phys. Rev. Lett.* **105,** 077001. `https://link.aps.org/doi/10.1103/PhysRevLett.105.077001` (2010).

77. Oreg, Y., Refael, G. & von Oppen, F. Helical Liquids and Majorana Bound States in Quantum Wires. *Phys. Rev. Lett.* **105,** 177002. `https://link.aps.org/doi/10.1103/PhysRevLett.105.177002` (2010).

78. Lahtinen, V. & Pachos, J. K. A Short Introduction to Topological Quantum Computation. *SciPost Phys.* **3,** 021. `https://scipost.org/10.21468/SciPostPhys.3.3.021` (2017).

79. Nadj-Perge, S. *et al.* Observation of Majorana fermions in ferromagnetic atomic chains on a superconductor. *Science* **346,** 602–607. `https://science.sciencemag.org/content/346/6209/602` (2014).

80. Mourik, V. *et al.* Signatures of Majorana Fermions in Hybrid Superconductor-Semiconductor Nanowire Devices. *Science* **336,** 1003–1007. `https://science.sciencemag.org/content/336/6084/1003` (2012).

81. Nielsen, H. & Ninomiya, M. The Adler-Bell-Jackiw anomaly and Weyl fermions in a crystal. *Physics Letters B* **130,** 389–396. `http://www.sciencedirect.com/science/article/pii/0370269383915290` (1983).

82. Burkov, A. A., Hook, M. D. & Balents, L. Topological nodal semimetals. *Phys. Rev. B* **84,** 235126. `https://link.aps.org/doi/10.1103/PhysRevB.84.235126` (2011).

83. Hasan, M. Z., Xu, S.-Y., Belopolski, I. & Huang, S.-M. Discovery of Weyl Fermion Semimetals and Topological Fermi Arc States. *Annual Review of Condensed Matter Physics* **8,** 289–309. `https://doi.org/10.1146/annurev-conmatphys-031016-025225` (2017).

84. Wolgast, S. *et al.* Low-temperature surface conduction in the Kondo insulator SmB_6. *Phys. Rev. B* **88,** 180405. `https://link.aps.org/doi/10.1103/PhysRevB.88.180405` (2013).

85. Kim, D. J. *et al.* Surface Hall Effect and Nonlocal Transport in SmB6: Evidence for Surface Conduction. *Scientific Reports* **3,** 3150. `https://doi.org/10.1038/srep03150` (2013).

86. Zhang, L., Ren, J., Wang, J.-S. & Li, B. Topological magnon insulator in insulating ferromagnet. *Phys. Rev. B* **87,** 144101. `https://link.aps.org/doi/10.1103/PhysRevB.87.144101` (2013).

87. Cai, W. *et al.* Observation of topological magnon insulator states in a superconducting circuit. *arXiv,* 1901.05683. `http://arxiv.org/abs/1901.05683` (2019).

88. Chen, L. *et al.* Topological Spin Excitations in Honeycomb Ferromagnet CrI_3. *Phys. Rev. X* **8,** 041028. `https://link.aps.org/doi/10.1103/PhysRevX.8.041028` (2018).

89. Wang, J., Lian, B., Qi, X.-L. & Zhang, S.-C. Quantized topological magnetoelectric effect of the zero-plateau quantum anomalous Hall state. *Phys. Rev. B* **92,** 081107. `https://link.aps.org/doi/10.1103/PhysRevB.92.081107` (2015).

90. Mondal, M. *et al.* Electric field modulated topological magnetoelectric effect in Bi_2Se_3. *Phys. Rev. B* **98,** 121106. `https://link.aps.org/doi/10.1103/PhysRevB.98.121106` (2018).

91. Khomskii, D. I. Magnetic monopoles and unusual dynamics of magnetoelectrics. *Nature Communications* **5,** 4793. `https://doi.org/10.1038/ncomms5793` (2014).

92. Zülicke, U. & Winkler, R. Magnetoelectric effect in bilayer graphene controlled by valley-isospin density. *Phys. Rev. B* **90,** 125412. `https://link.aps.org/doi/10.1103/PhysRevB.90.125412` (2014).

93. Kim, H.-J. *et al.* Dirac versus Weyl Fermions in Topological Insulators: Adler-Bell-Jackiw Anomaly in Transport Phenomena. *Phys. Rev. Lett.* **111,** 246603. `https://link.aps.org/doi/10.1103/PhysRevLett.111.246603` (2013).

94. Dai, X., Du, Z. Z. & Lu, H.-Z. Negative Magnetoresistance without Chiral Anomaly in Topological Insulators. *Phys. Rev. Lett.* **119,** 166601. `https://link.aps.org/doi/10.1103/PhysRevLett.119.166601` (2017).

95. Taskin, A. A. *et al.* Planar Hall effect from the surface of topological insulators. *Nature Communications* **8,** 1340. `https://doi.org/10.1038/s41467-017-01474-8` (2017).

96. Nandy, S., Taraphder, A. & Tewari, S. Berry phase theory of planar Hall effect in topological insulators. *Scientific Reports* **8,** 14983. `https://doi.org/10.1038/s41598-018-33258-5` (2018).

97. Cano, J. *et al.* Chiral anomaly factory: Creating Weyl fermions with a magnetic field. *Phys. Rev. B* **95,** 161306. `https://link.aps.org/doi/10.1103/PhysRevB.95.161306` (2017).

98. Liu, C.-X. *et al.* Model Hamiltonian for topological insulators. *Phys. Rev. B* **82,** 045122. `http://link.aps.org/doi/10.1103/PhysRevB.82.045122` (2010).

99. Nechaev, I. A. & Krasovskii, E. E. Relativistic $k \cdot p$ Hamiltonians for centrosymmetric topological insulators from *ab initio* wave functions. *Phys. Rev. B* **94,** 201410. `https://journals.aps.org/prb/abstract/10.1103/PhysRevB.94.201410` (2016).

100. Wang, Z., Weng, H., Wu, Q., Dai, X. & Fang, Z. Three-dimensional Dirac semimetal and quantum transport in Cd_3As_2. *Phys. Rev. B* **88,** 125427. `https://link.aps.org/doi/10.1103/PhysRevB.88.125427` (2013).

101. Xiao, X., Yang, S. A., Liu, Z., Li, H. & Zhou, G. Anisotropic Quantum Confinement Effect and Electric Control of Surface States in Dirac Semimetal Nanostructures. *Sci. Rep.* **5,** 7898. `https://www.nature.com/articles/srep07898` (2015).

102. Nechaev, I. A., Eremeev, S. V., Krasovskii, E. E., Echenique, P. M. & Chulkov, E. V. Quantum spin Hall insulators in centrosymmetric thin films composed from topologically trivial BiTeI trilayers. *Scientific Reports* **7,** 43666. `https://doi.org/10.1038/srep43666` (2017).

103. Stanescu, T. D., Galitski, V., Vaishnav, J. Y., Clark, C. W. & Das Sarma, S. Topological insulators and metals in atomic optical lattices. *Phys. Rev. A* **79,** 053639. `https://link.aps.org/doi/10.1103/PhysRevA.79.053639` (2009).

104. Cooper, N. R. Optical Flux Lattices for Ultracold Atomic Gases. *Phys. Rev. Lett.* **106,** 175301. `https://doi.org/10.1103/PhysRevLett.106.175301` (2011).

105. Zhang, D.-W., Zhu, Y.-Q., Zhao, Y. X., Yan, H. & Zhu, S.-L. Topological quantum matter with cold atoms. *Advances in Physics* **67,** 253–402. `https://doi.org/10.1080/00018732.2019.1594094` (2018).

106. Goldman, N. *et al.* Direct imaging of topological edge states in cold-atom systems. *Proceedings of the National Academy of Sciences* **110,** 6736–6741. `https://www.pnas.org/content/110/17/6736` (2013).

107. Kotulla, M. R. *Confinement Properties of Bi_2Se_3 Type 3D Topological Insulators* 2019. `https://doi.org/10.5281/zenodo.3234379`.

108. Winkler, R. *Spin-orbit coupling effects in two-dimensional electron and hole systems* `https://cds.cern.ch/record/684956` (Springer-Verlag Berlin Heidelberg, 2003).

109. Linder, J., Yokoyama, T. & Sudbø, A. Anomalous finite size effects on surface states in the topological insulator Bi_2Se_3. *Phys. Rev. B* **80,** 205401. `https://journals.aps.org/prb/abstract/10.1103/PhysRevB.80.205401` (2009).

110. Shan, W.-Y., Lu, H.-Z. & Shen, S.-Q. Effective continuous model for surface states and thin films of three-dimensional topological insulators. *New Journal of Physics* **12,** 043048. `https://iopscience.iop.org/article/10.1088/1367-2630/12/4/043048` (2010).

111. Zhang, Y. *et al.* Crossover of the three-dimensional topological insulator Bi_2Se_3 to the two-dimensional limit. *Nature Physics* **6,** 584–588. `https://doi.org/10.1038/nphys1689` (2010).

112. Yazyev, O. V., Moore, J. E. & Louie, S. G. Spin Polarization and Transport of Surface States in the Topological Insulators Bi_2Se_3 and Bi_2Te_3 from First Principles. *Phys. Rev. Lett.* **105,** 266806. `https://link.aps.org/doi/10.1103/PhysRevLett.105.266806` (2010).

113. Liu, C.-X. *et al.* Oscillatory crossover from two-dimensional to three-dimensional topological insulators. *Phys. Rev. B* **81,** 041307. `https://journals.aps.org/prb/abstract/10.1103/PhysRevB.81.041307` (2010).

114. Zhou, B., Lu, H.-Z., Chu, R.-L., Shen, S.-Q. & Niu, Q. Finite Size Effects on Helical Edge States in a Quantum Spin-Hall System. *Phys. Rev. Lett.* **101,** 246807. `https://journals.aps.org/prl/abstract/10.1103/PhysRevLett.101.246807` (2008).

115. Betancourt, J. *et al.* Complex band structure of topological insulator Bi_2Se_3. *J. Phys.: Condens. Matter* **28,** 395501. `https://iopscience.iop.org/article/10.1088/0953-8984/28/39/395501/meta` (2016).

116. Zhang, W., Yu, R., Zhang, H.-J., Dai, X. & Fang, Z. First-principles studies of the three-dimensional strong topological insulators Bi_2Se_3, Bi_2Te_3 and Sb_2Te_3. *New Journal of Physics* **12,** 065013. `https://doi.org/10.1088/1367-2630/12/6/065013` (2010).
117. Wolos, A. *et al.* G-factors of conduction electrons and holes in Bi_2Se_3 three-dimensional topological insulator. *Physical Review B* **93,** 1–8. `https://doi.org/10.1103/PhysRevB.93.155114` (2016).
118. Köhler, H. Anisotropic g-Factor of the Conduction Electrons in Bi_2Te_3. *Phys. Stat. Sol. (b)* **75,** 127–136. `https://onlinelibrary.wiley.com/doi/abs/10.1002/pssb.2220670229` (1976).
119. Takahashi, R. *Topological States on Interfaces Protected by Symmetry* `https://www.springer.com/gp/book/9784431555339` (Springer, Tokyo, 2015).
120. Zyuzin, A. A., Hook, M. D. & Burkov, A. A. Parallel magnetic field driven quantum phase transition in a thin topological insulator film. *Phys. Rev. B* **83,** 245428. `https://link.aps.org/doi/10.1103/PhysRevB.83.245428` (2011).
121. Xu, Y., Jiang, G., Miotkowski, I., Biswas, R. R. & Chen, Y. P. Tuning Insulator-Semimetal Transitions in 3D Topological Insulator thin Films by Intersurface Hybridization and In-Plane Magnetic Fields. *Phys. Rev. Lett.* **123,** 207701. `https://link.aps.org/doi/10.1103/PhysRevLett.123.207701` (2019).
122. Pan, H., Wu, M., Liu, Y. & Yang, S. A. Electric control of topological phase transitions in Dirac semimetal thin films. *Sci. Rep.* **5,** 14639. `https://www.nature.com/articles/srep14639` (2015).
123. Liu, Z., Jiang, L. & Zheng, Y. Band structure of a three-dimensional topological insulator quantum wire in the presence of a magnetic field. *J. Phys.: Condens. Matter* **28,** 275501. `http://stacks.iop.org/0953-8984/28/i=27/a=275501` (2016).